AN ANALYTICAL AND EXPERIMENTAL INVESTIGATION FOR
AN INTERSTITIAL INSULATION TECHNOLOGY

A Dissertation

by

DONG KEUN KIM

Submitted to the Office of Graduate Studies of
Texas A&M University
in partial fulfillment of the requirements for the degree of

DOCTOR OF PHILOSOPHY

May 2008

Major Subject: Mechanical Engineering

AN ANALYTICAL AND EXPERIMENTAL INVESTIGATION FOR

AN INTERSTITIAL INSULATION TECHNOLOGY

A Dissertation

by

DONG KEUN KIM

Submitted to the Office of Graduate Studies of
Texas A&M University
in partial fulfillment of the requirements for the degree of

DOCTOR OF PHILOSOPHY

Approved by:

Chair of Committee,	Edigio Marotta
Committee Members,	Debjyoti Banerjee
	Sai Lau
	Tahir Cagin
Head of Department,	Dennis L. O'Neal

May 2008

Major Subject: Mechanical Engineering

ABSTRACT

An Analytical and Experimental Investigation for an Interstitial Insulation

Technology.

(May 2008)

Dong Keun Kim, B.S., Hankuk Aviation University;

M.S., Hankuk Aviation University

Chair of Advisory Committee: Dr. Egidio Marotta

An insulation technique has been developed which contains a single or combination of materials to help minimize heat loss in actual industrial applications. For the petroleum industry, insulation for deep sea piping is one of the greatest challenges which would prevent the industry from meeting the high demand for oil through exploration into deeper ocean environments. At current seafloor depths (5,000~10,000ft), pipeline insulation is essential in preventing pipeline blockage resulting from the solidification of paraffin waxes and / or hydrate formation which exist in crude oil. To maintain crude oil temperatures above the paraffin solidification point (68°C or 155°F), new and better insulation techniques are essential to minimize pipeline heat loss and maintain crude oil temperatures. Therefore, the objective of this investigation was to determine whether or not the thermal resistance of a new insulation concept, which involves IIT (Interstitial Insulation Technology) with screen wire, was greater than existing readily available commercial products through

analytical modeling and experimentation. The model takes into account both conforming and nonconforming interfaces at the wire screen contacts within the interstitial space between coaxial pipes.

In addition, confirmation was needed to determine whether or not laboratory testing of simulated coupons translate to thermal performance for a prototype pipe segment that fabricated with two layers of low conductivity wire-screen (stainless steel) as the interstitial insulation material. Both the inner and outer surface temperatures of the coaxial pipes were measured in order to evaluate the effective thermal conductivity and thermal diffusivity of the insulation concept. The predicted results from the model compared very favorably with the experimental results, confirming both the trends and magnitudes of the experimental data. In other words, whether the reduction in heat transfer observed for small laboratory samples was realistic for application to a pipeline configuration. This effort involved both analytical modeling for all thermal resistances and experimental test runs for validation of the analytical model.

Finally, it was a goal of this investigation to develop a simplified model for a multilayer composite structure which will include radiation heat transfer exchange among the layers that constitute the insulation. With the developed model, feasibility and performance characteristics of the insulation concept were predicted. The thermal predictions have demonstrated the thermal competitiveness of the interstitial insulation technology.

DEDICATION

To my lovely wife Jaennie for her great love,

my parents and parents in law, for their love and support,

and all my friends for their friendship.

ACKNOWLEDGEMENTS

I would like to thank my advisor, Dr. Egidio Marotta, for his guidance and support. His advice and encouragement are greatly appreciated. Thanks to Dr. Banerjee, Dr. Lau and Dr. Cagin, members of my advisory committee, for their time and interest.

I acknowledge the friendship and support of my friends, Yeonseok Kim, Taeho Kim, Hyeokjin Oh and other friends at the Conduction Heat Transfer Laboratory.

Finally I would like to thank my wife, Jaennie, and my family for their support.

TABLE OF CONTENTS

LIST OF FIGURES

Page

LIST OF TABLES

NOMENCLATURE

A =   *Area, (m^2)*

$A+B$ =   *Geometric parameter related to radius of curvature, ($1/m$)*

Bi =   *Biot number, Dimensionless*

C =   *Coefficient, dimensionless*

D =   *Diameter, (m)*

E =   *Modulus of elasticity, (N/m^2)*

                     Emissivity Power, (W/m^2)

E' =   *Effective modulus of elasticity, (N/m^2)*

F =   *Applied load, (N)*

                     View Factor

H =   *Hardness, (MPa)*

I_g =   *Gap conductance integral, dimensionless*

K =   *Complete elliptic integral of first kind, dimensionless*

L =   *Length, (m)*

M =   *Gas parameter, (m)*

N =   *Number of microcontacts, dimensionless*

Nu =   *Nusselt Number, Dimentionless*

P =   *Pressure, ($N/m^2, Pa$)*

Pr	=	Prandtl number, Dimensionless
$\dot{Q}$	=	Heat rate, (W)
R	=	Thermal resistance, (K/W)
Ra	=	Rayleigh number, Dimensionless
Ra^*	=	Modified *Rayleigh number*, Dimensionless
T	=	Temperature, (K)
Y	=	Mean plane separation, (m)
a	=	Semi-major diameter of ellipse, (m)
a_c	=	Microcontact radius, (m)
b	=	Semi-minor diameter of ellipse, (m)
c	=	Length between nodes, (m)
c_1	=	Correlation coefficient, dimensionless
c_2	=	Correlation coefficient, (GPa)
f	=	Combination of terms, dimensionless
g	=	Gravitational Acceleration, (m/s^2)
h	=	Thermal conductance, Heat transfer coefficient, $(W/m^2 \cdot K)$
k	=	Thermal conductivity, $(W/m \cdot K)$
m	=	Absolute asperity slope, radian
		Semimajor axis parameter, dimensionless
n	=	Number density of contact spot $(1/m^2)$
r^*	=	Dimensionless Radius, Dimensionless

t	=	Elapsed cooling time, (s)
		Wall thickness, (m)
α	=	Ratio of semi-major axes, dimensionless
		Thermal diffusivity, (m^2 / s)
δ	=	Normal deformation of surface, (m)
ε	=	Relative contact spot size, dimensionless
θ^*	=	Dimensionless temperature, dimensionless
κ	=	Parameter, dimensionless
ζ	=	Eigen value, dimensionless
λ	=	Relative mean plane separation, dimensionless
ν	=	Poisson's ratio, dimensionless
		Kinematic viscosity, (m^2 / s)
ρ	=	Minimum Radius of curvature, (m)
ρ'	=	Maximum Radius of curvature, (m)
σ	=	Effective surface roughness, (m)
ψ	=	Constriction parameter, dimensionless
Δ	=	Physical parameter, (m / N)

Subscript

$1-2$	=	Surface 1 and 2
a	=	Apparent
b	=	Black body
c	=	Constriction, Contact, Coolant

ct	=	*Elapse cooling*
e	=	*Elliptic, elastic*
eff	=	*Effective*
g	=	*Gas*
i	=	*Inner*
is	=	*Inner Surface*
iw	=	*Inner wall*
mc	=	*Microcontact*
n	=	*Order*
o	=	*Outer*
ow	=	*Outer wall*
os	=	*Outer surface*
p	=	*Plastic*
r	=	*Real*
rad	=	*Radiation*
ss	=	*Cooing bath surface*
tmc	=	*Total microcontact*
tot	=	*Total*
w	=	*Wire of screen mesh, Water*

CHAPTER I

INTRODUCTION

The high demand for oil has come from an exponential increase in transportation's use of the internal combustion engine within developed and developing countries. To meet this high demand, oil industries have explored more offshore locations for more oil products. But within the deep sea environment temperatures can range from 0°C to 2°C (32°F to 35°F), thus pipe insulation is obligatory to prevent blockage in the pipe due paraffin and hydrate build-up. Crude oil often contains a type of wax that begins to form solid paraffin deposits on the inner surface of the pipe when the oil temperature reaches the paraffin cloud point (68°C or 155°F); therefore, blockage can and does occur. When paraffin waxes block the inside of the pipe, an additional process is needed to remove it which translates to reduced production efficiency. Crude oil production temperatures are typically above 70°C (159°F) and to maintain the inner wall temperature above the paraffin and hydrate formation point, heat loss from the pipe wall must be minimized. Several insulation techniques have been developed to overcome the thermal issue by the addition of low conductivity materials and coatings on the external pipe surface using syntactic form and urethane. However, these techniques often have had severe limitations such as damage due to large hydrostatic pressure differentials and installation concerns.[1, 2, 3] Thus, more advanced insulation techniques have been developed to assure proper oil flow in increasingly challenging environments. Raymond et al. [3] developed a new insulation technique, named

_____

This dissertation follows the style of the ASME Journal of Heat Transfer.

ILS(Liquid Solid Insulation), using a liquid solid which acts as a heat accumulator in normal flow conditions, but during cool down restores its stored thermal energy to the flow line. It is claimed that this ILS can enhance the cool down period 2 to 4 times longer with respect to the existing insulation technologies. Azzola et al. [4] developed an insulation technique, named VIT (Vacuum Insulated Tubing), which contains a vacuumed annulus between inner and outer pipe walls. This minimizes the heat loss from hot inner pipe walls up to 90% of total heat loss. Compact space of insulation layer, high load capacity (200,000~500,000 lbs tension load) and high thermal insulation values are known as its advantages. However, these new insulation techniques still have problems such as environmental pollution when leakage occurred and difficult to maintain its vacuum status. This could cause additional maintenance cost and have to face the situation of trading off between the performance and the cost.

In this research, analytical and experimental investigations on a newly developed insulation technique, IIT (Interstitial Insulation Technology), which contains either one or more layers of a wire screen as an interstitial material within the annulus are conducted. A reduction in the heat transfer rate, and thus retardation in paraffin build-up, can be achieved without the limitations previously stated. Moreover, the manufacture and installation process for sub-sea piping will be greatly simplified [5]. Within the interstitially insulated coaxial pipe, the interstitial fluid is air which remains stagnant. However, other gases can be employed to achieve greater insulation performance. Air spaces between the coaxial pipes are small enough to prevent natural convection from occurring which leads to conduction heat transfer through the annulus.

Therefore, the dominate heat transfer mechanism for this system will be conduction through nonconforming contacts between the wall and wire screen. In addition, conforming micro contacts within the screen wire and pipe wall itself can provide an additional resistance heat flow path between contacting interfaces. Both macro contact and micro contact models will be reviewed to develop a proper joint resistance model. To aid in the model development, a thermal network circuit will be drawn to help visualize the heat path and aid in the joint model development.

A review of the literature on thermal contact resistance shows an extensive number of publications for both experimental and analytical studies. There exist numerous papers which detail correlations and analytical models for contact resistance for rough, conforming surfaces and nonconforming contacting surfaces [6]. These studies take various approaches; however, little work has been performed for a joint that contains both contacts simultaneously such as a wire screen.

An initial analytical study by Cividino et al. [7] analyzed joint conductances for a woven wire screen utilizing only Hertzian theory [8] to predict the macro contact area when a wire screen contacts a solid surface. The authors have neglected bulk resistance due to wire-to-wire contacts and micro resistances present at the surface. However, to obtain a more accurate model, micro contact analysis under the deformed macro contact area is required as well. Therefore, this investigation will develop an analytical model that combines both macro and micro contact theory to predict the overall joint resistance for contacting surfaces containing a wire screen.

Lambert and Fletcher [9] reviewed contact resistance models for various cases under vacuum condition while Sridhar and Yovanovich [10] reviewed elastic and plastic models which showed that smooth, contacting surfaces deform elastically and rough surfaces deform plastically. Also, Savija et al. [11] contained an excellent review for thermal conductance models with interstitial substances inserted at the joint.

In this investigation, along with an improved model for macro and micro contact resistances, fluid gap resistances are developed simultaneously. Predictions from the enhanced model are compared with experimental data from a previous experimental study [5] which contained an interstitially wire screen material in the annulus of a simulated coaxial pipe.

From the prior coupon size testing [5], an insulation system incorporating a low thermal conductivity screen mesh between a pipe and an interior liner was shown to be an effective passive thermal insulation solution for deepwater flow lines and risers. It has been established that a thermal resistance (due to the metrology of the contacting surfaces) was created at an interface between two materials, in this case a pipe and a liner. If the two contacting surfaces are further separated by a screen wire or mesh at the pipe and liner interface, then a higher thermal interface resistance will result, which will significantly increase the resistance to thermal transport characteristics. The screen wire reduces the heat transfer by restricting the path for conduction and forms a stagnant air gap to minimize convective heat transfer. Heat transfer can be further reduced by adding a polymeric insulation layer (between the screen mesh and interior liner) and by the addition of multiple layers for actual applications. As an intermediate

stage towards actual size pipe testing, an experimental investigation with a prototype

pipe insulation system is conducted.

CHAPTER II

ANALYTICAL MODEL

Thermal Circuit Modeling

Cividino et al. [7] developed an analytical model for a woven wire screen contacting a solid wall, but in this study the bulk resistance, through the screen wire, and the microcontact resistances within the wires were neglected. Moreover, to have a more accurate model the contact points among wire screen materials must be account for as well. In the present experimental study, the actual specimen diameter was 1 inch (2.54 cm) as shown by Fig. 1 a).

To properly build the thermal circuit, the nominal area was specified, and then divided into a unit cell area. Each unit cell area had four nodes. Figs. 1 a) and b) are top view of the actual wire screen and thermal flow paths, respectively. The heat flow path from the inner pipe wall to the outer pipe wall was simplified as shown in Figs. 2 a) and b).

For a given unit cell, four nodes were connected in parallel connection while each node has both serial and parallel paths (resistances).[12] The overall thermal resistance for the unit cell can be written as a parallel circuit of each node as shown in Fig. 3.
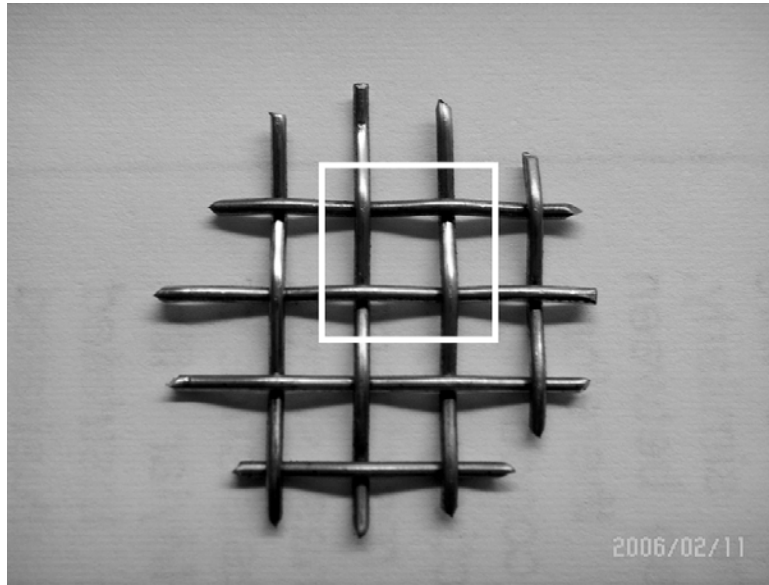
a)
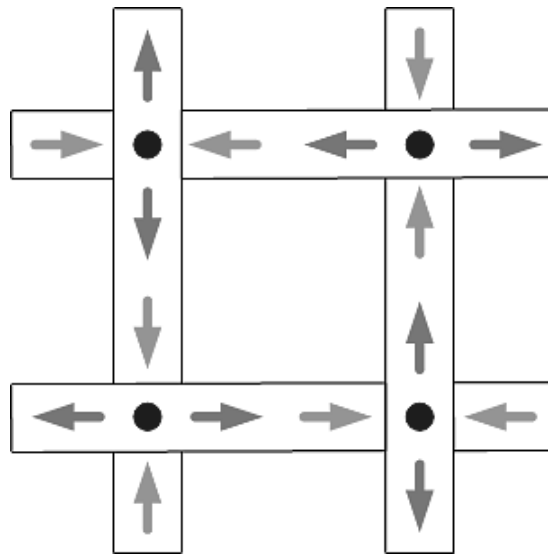
b)

Figure 1 a) Top view of unit cell of the screen wire.

b) schematic of heat flow in a unit cell.
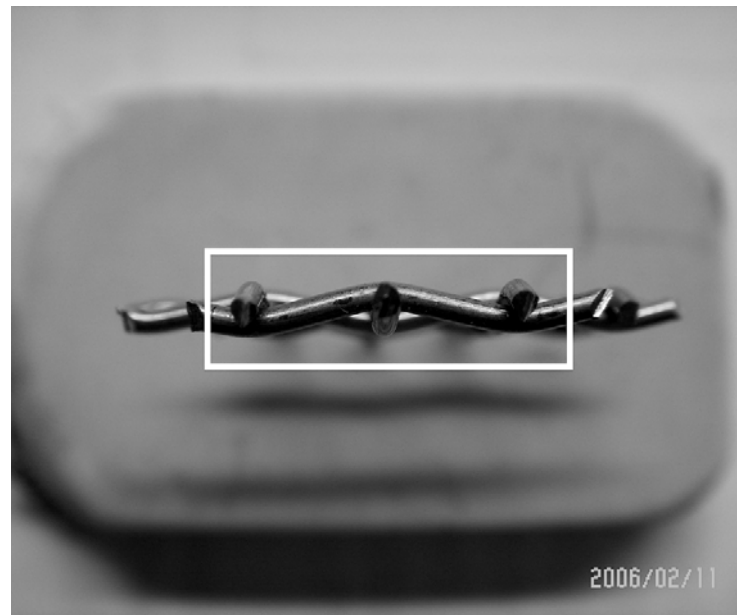
a)
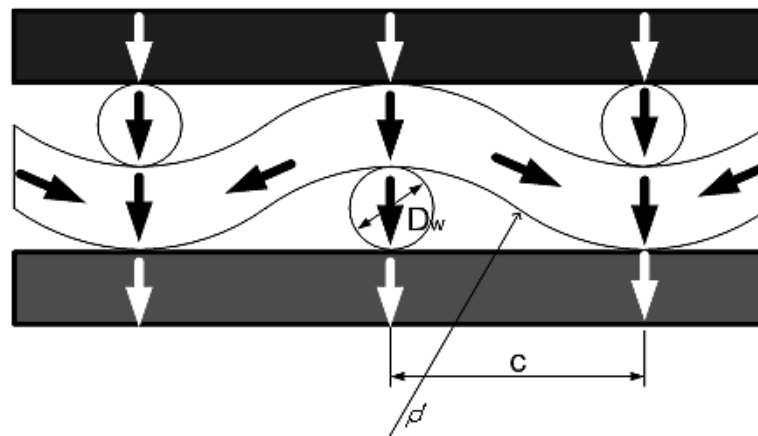
b)

Figure 2 a) Side view of unit cell of the screen wire.

b) schematic of heat flow path.

a)

b)
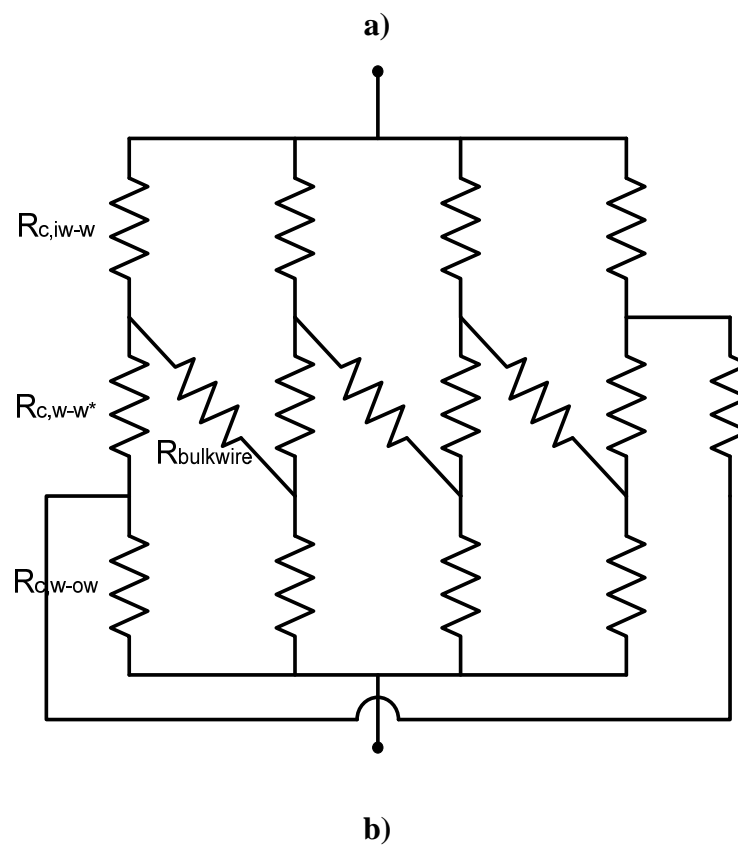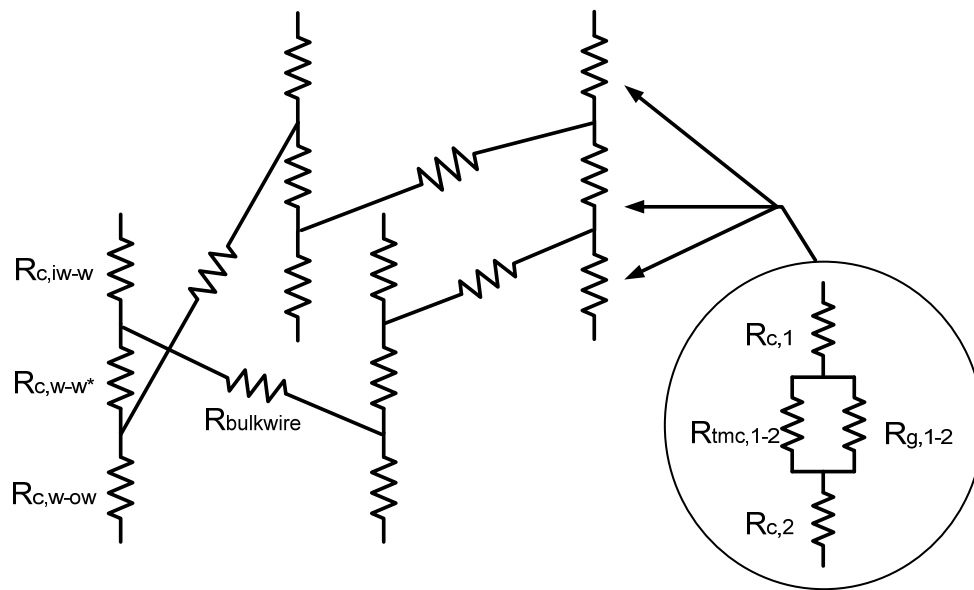
Figure 3 a) Thermal circuit in a unit cell.

b) thermal circuit in a unit cell in a closed form.

Contact Resistance Model

The joint analytical model was based on a combination of macro contact resistance, micro contact resistance, micro gap resistance, bulk resistance and air resistance for each node in the unit cell, and then programmed with the use of Matlab™ Software.

Macro Contact Model

Nonconforming contact modeling was the first step in developing the model, and was based on expressions for macro contact resistance developed by Yovanovich [13]. To obtain the contact area formed by the applied load on each nodal contact, geometrical parameters for screen wire and walls14 as shown in Fig. 2. b) were calculated with the following expressions,

$$\alpha = \frac{c}{D_w} \tag{1}$$

$$\rho = \frac{D_w}{2} \tag{2}$$

$$\rho' = \frac{D_w}{4}(1+\alpha^2) \tag{3}$$

where ρ', ρ are the maximum and minimum of radius of curvature (for flat surface $\rho' = \rho = \infty$), c and D_w are the distances between nodes and the wire screen diameter, respectively.

The inner and outer walls were assumed to be flat surfaces so that their curvatures were considered to be infinite. Each contact point formed an elliptical contact area with semi-major and semi-minor axes a and b computed as follow.

$$a = m\left[\frac{3}{4}F\Delta\right]^{\frac{1}{3}}, \quad b = n\left[\frac{3}{4}F\Delta\right]^{\frac{1}{3}} \tag{4}$$

where m and n are dimensionless parameters obtained from the expressions [14] below for the range of values $2 < \alpha < 8$, F is the applied force on each node and Δ is a geometric-physical parameter shown below,

$$m = 0.830\alpha^{0.735}, \quad \frac{m}{n} = 0.7905\alpha^{1.18} \tag{5}$$

$$F = PA_{apparent} = Pc^2 \tag{6}$$

$$\Delta_{1-2} = \frac{\left[\dfrac{1-\nu_1^2}{E_1} + \dfrac{1-\nu_2^2}{E_2}\right]}{A+B} \tag{7}$$

$$A + B = \frac{1}{2}\left[\frac{1}{\rho_1} + \frac{1}{\rho_1'} + \frac{1}{\rho_2} + \frac{1}{\rho_2'}\right] \tag{8}$$

Since the formed elliptical contact area is very small when compared with the nodal area, the thermal resistance in the contact area can be modeled as a thermal constriction-spreading resistance within half-space [13]. With the calculated semi-major and semi-minor axes, the thermal constriction resistance for the contact area of each node can be determined as,

$$R_{constriction} = \frac{\psi_e^T}{4ka} \tag{9}$$

where ψ_e^T is the spreading/constriction parameter defined [14] as,

$$\psi_e^T = \frac{2}{\pi}K(\kappa) \tag{10}$$

and $K(\kappa)$ is the complete elliptic integral of the first kind with κ defined as,

$$\kappa = \left[1 - \left(\frac{b}{a}\right)^2\right]^{1/2} \tag{11}$$

The constriction-spreading resistance between the two different materials was the summation of each resistance,

$$R_{constriction12} = R_{c1} + R_{c2} \tag{12}$$

A total of three constriction-spreading resistances existed for each nodal contact (e.g. $R_{iw-w}, R_{w-w}, R_{w-ow}$).

Bulk Resistance (wire)

In the thermal circuit, some portion of the heat flow within wire itself between each node must be taken into account as shown in Fig. 3. Analyzing the circuit network via Kirchhoff's Law [15], the amount of heat out flow and in flow must be identical, and can be modeled as a parallel resistance with the wire to wire constriction resistance and bulk resistance. The bulk resistance through the wire was defined as,

$$R_{bulkwire} = \frac{2L}{k_w A_w} \tag{13}$$

where A_w (defined below) and L are the wire cross-sectional area and wire length, respectively.

$$A_w = \frac{\pi D_w^2}{4}, L = \sqrt{c^2 + D_w^2} \tag{14}$$

Micro Contact Resistance

Within the elliptical contact area formed by the applied load, a number of conforming microcontacts were also formed; therefore, micro constriction/spreading and gap resistances coexisted in parallel. Generally, each surface has roughness where all contacting asperities were assumed be isotropic and randomly distributed over the contacting surfaces, i.e., Gaussian surface [16].

Between two Gaussian surfaces, the contact can be simplified as a flat/rough surface with an effective roughness and slope. The effective RMS surface roughness and effective absolute mean asperity slope were computed as,

$$\sigma = \sqrt{\sigma_1^2 + \sigma_2^2}, \quad m = \sqrt{m_1^2 + m_2^2} \tag{15}$$

Depending on the deformation mode of the contacting asperities, two model types are available - plastic or elastic. With geometric parameters obtained from each model, the contact resistances can be obtained with the use of the following relationships [17],

$$h_c = \frac{2nak_s}{\psi(\varepsilon)} \tag{16}$$

$$k_s = \frac{2k_1k_2}{k_1 + k_2} \tag{17}$$

$$\psi(\varepsilon) = (1-\varepsilon)^{1.5}, \varepsilon = \sqrt{\frac{A_r}{A_a}} \tag{18}$$

Details of plastic and elastic model are further explained in the following sections below.

Plastic Model

If contacting asperities are deformed plastically, then the following relationships via Cooper et al.[17, 18] are applicable with appropriate geometric parameters,

$$\lambda = \left(\frac{Y}{\sigma}\right)_p = \sqrt{2}erfc^{-1}\left(\frac{2P}{H_p}\right) \tag{19}$$

$$a_c = \sqrt{\frac{8}{\pi}\frac{\sigma}{m}}\exp\left(\frac{\lambda^2}{2}\right)erfc\left(\frac{\lambda}{\sqrt{2}}\right) \tag{20}$$

$$n = \frac{1}{16}\left(\frac{m}{\sigma}\right)^2\frac{\exp(-\lambda^2)}{erfc(\lambda/\sqrt{2})} \tag{21}$$

$$\frac{A_r}{A_a} = \frac{1}{2}erfc(\frac{\lambda}{\sqrt{2}}) \tag{22}$$

where λ, a_c, n and A_r/A_a are the relative mean plane separation, radius of microcontact, number density of contact, and the ratio of actual contact area to nominal area, respectively. In Eq. (19), H_p is the microhardness of the softer contacting asperities.

An appropriate microhardness can be obtained from the relative contact pressure P/H_P relationship developed by Song et. al.[19],

$$\frac{P}{H_p} = \left[\frac{P}{c_1(1.62\sigma/m)^{c_2}}\right]^{1/(1+0.071c_2)} \tag{23}$$

$$\frac{c_1}{3178} = 4.0 - 5.77 H_B^* + 4.0(H_B^*)^2 - 0.61(H_B^*)^3$$

$$H_B^* = \frac{H_B}{3178} \tag{24}$$

$$c_2 = -0.370 + 0.442(\frac{H_B}{c_1})$$

where c_1, c_2 are the correlation coefficients which are obtained from Vickers microhardness measurements. Equivalent Vickers microhardness can be computed from Brinell hardness values H_B .

Elastic Model

The Elastic deformation model for contacting asperities was initially proposed by Mikic [20] as follows,

$$\lambda = \left(\frac{Y}{\sigma}\right)_e = \sqrt{2} erfc^{-1}\left(\frac{4P}{H_e}\right) \tag{25}$$

$$a_c = \frac{2}{\sqrt{\pi}} \frac{\sigma}{m} \exp\left(\frac{\lambda^2}{2}\right) erfc\left(\frac{\lambda}{\sqrt{2}}\right) \tag{26}$$

$$n = \frac{1}{16}\left(\frac{m}{\sigma}\right)^2 \frac{\exp(-\lambda^2)}{erfc(\lambda/\sqrt{2})} \tag{27}$$

$$\frac{A_r}{A_a} = \frac{1}{4} erfc(\frac{\lambda}{\sqrt{2}}) \tag{28}$$

$$H_e = CmE', C = 0.7071 \tag{29}$$

$$\frac{1}{E'} = \frac{1-v_1^2}{E_1} + \frac{1-v_2^2}{E_2} \tag{30}$$

where H_e, $\frac{1}{E'}$ are the equivalent elastic hardness and the effective Young's modulus, respectively.

With appropriate geometrical parameters and either the plastic or elastic model, the microcontact thermal resistance can be computed as,

$$R_{mc} = \frac{1}{h_c \pi a_c^2} \tag{31}$$

For a given nodal area, the total microcontact resistance was calculated with the following expression,

$$R_{tmc} = \frac{R_{mc}}{N_{mc}} \tag{32}$$

where ($N_{mc} = n \times A_e, A_e = \pi ab$) N_{mc} is the number of micro contacts within the nodal area A_{node}.

Micro Gap Resistance

In the present investigation, the space within the wall and wire screen and the micro-gap between the contacting interfaces was filled with air, which is the media of conduction across the gap. The gap conductance model was first developed by Yovanovich [18] as

$$h_g = \frac{k_g}{\sigma} I_g \tag{33}$$

A correlation equation for the gap integral I_g was developed by Negus et al. [21] which depends on two dimensionless parameters, the relative mean planes separation Y/σ and the relative gas rarefaction parameter M/σ.

$$I_g = \frac{f_g}{\dfrac{Y}{\sigma} + \dfrac{M}{\sigma}} \tag{34}$$

where $f_g = 1.063 + 0.0471\left(4 - \dfrac{Y}{\sigma}\right)^{1.68}\left(\ln\dfrac{\sigma}{M}\right)^{0.84}$.

The gas's dependence on pressure and temperature for the gas parameter M was presented by Yovanovich et al.[22] in Eq. (35).

$$M = 0.373 \times 10^{-6} \times \frac{T_{air}}{323} \times \frac{P_{g,1atm}}{P_g} \tag{35}$$

With these parameters, the micro-gap resistance for a node was obtained as

$$R_g = \frac{1}{h_g \pi ab} \tag{36}$$

In Eq. (36), πab is the formed contact area in a node.

Air Resistance in the Space Within Walls and Wire screen

The interstitial area between the inner and outer wall was occupied with air and wire screen, and the area not occupied by the wire screen was the cross-sectional area occupied by trapped air. The area of the unit cell was $A_{node} = c^2$. Thus the occupied air cross-sectional area was computed as,

$$A_{air} = A_{node} - \left(2 \times c \times D_w - D_w^{\,2}\right) \tag{37}$$

When the load was applied to the node, each contact point was deformed in the same direction as the applied, whose deformation can be obtained from the expression developed by Johnson [8],

$$\delta = \frac{3F}{2\pi abE'} bK(\kappa) \tag{38}$$

Therefore, the thermal resistance through the air in the space for each deformed node and air space can be expressed as,

$$R_{air} = \frac{2D_w - \delta_{iw-w} - \delta_{w-w} - \delta_{w-ow}}{k_{air}A_{air}} \tag{39}$$

This expression takes into account the wire deformation and its influence on the gap of the air space.

Total Resistance

The total contact resistance for each node from the inner wall to the wire mesh, and then the outer wall was a summation of all the resistances which were in serial and parallel as shown in Fig. 4.

The following expressions detail the equations used to calculate each component. For the inner or outer wall and wire screen, the following expressions were used,

$$R_{c,iw-w} = R_{c,iw} + \left(\frac{1}{R_{tmc,iw-w}} + \frac{1}{R_{g,iw-w}} \right)^{-1} + R_{c,w} \tag{40}$$

$$R_{c,w-ow} = R_{c,w} + \left(\frac{1}{R_{tmc,w-ow}} + \frac{1}{R_{g,w-ow}} \right)^{-1} + R_{c,ow} \tag{41}$$
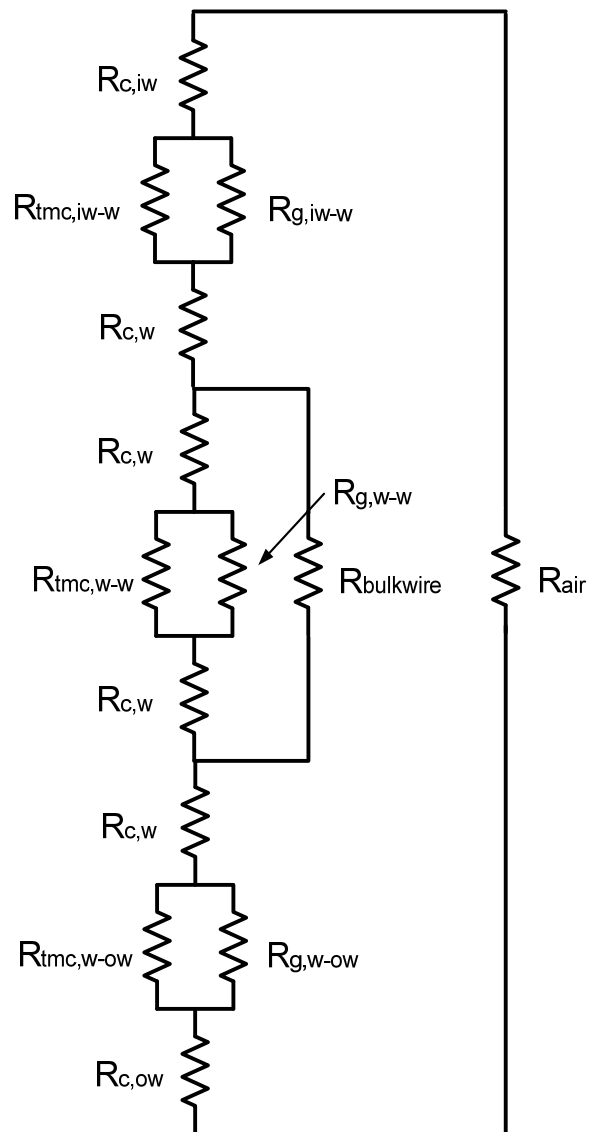
Figure 4 Total thermal circuit for a node.

For the resistance of the wire screen, the following expression was employed,

$$R_{c,w-w} = \left(\cfrac{1}{\left(R_{c,w} + \left(\cfrac{1}{R_{tmc,w-w}} + \cfrac{1}{R_{g,w-w}} \right)^{-1} + R_{c,w} \right)} + \cfrac{1}{R_{bulkwire}} \right)^{-1} \tag{42}$$

The total contact resistance of each node was calculated from the summation of the contact points as follow,

$$R_{tot,c} = R_{c,iw-w} + R_{c,w-w} + R_{c,w-ow} \tag{43}$$

The total contact resistance was in parallel with the air space resistance shown in Fig. 4 and computed as,

$$R_{tot,node} = \left(\frac{1}{R_{tot,c}} + \frac{1}{R_{air}} \right)^{-1} \tag{44}$$

One unit cell had four nodes that exist as parallel resistances; therefore, the total resistance for the unit cell became,

$$R_{tot,cell} = \left(\frac{4}{R_{tot,node}} \right)^{-1} \tag{45}$$

The number of unit cells in an actual area can obtained from the following expression,

$$N_{cell} = \frac{A_{actual}}{A_{cell}} \tag{46}$$

In a similar manner, actual joint thermal resistance can obtained as,

$$R_{actual} = \left(\frac{N_{cell}}{R_{tot,cell}} \right)^{-1} \tag{47}$$

Finally, conductance for the actual area can be expressed as,

$$h_{actual} = \frac{1}{R_{actual} A_{actual}} \tag{48}$$

In this expression, actual area is a coupon area which has one (1) inch diameter.

As mentioned above, thermal resistance of a node which included all resistance components such as macro contact resistance, micro gap resistance, bulk resistance, micro resistance (plastic or elastic), micro gap resistance and air resistance and presented as parallel and serial resistance combination form as shown in Fig. 4. Four resistances of a node formed a resistance of a unit cell as a parallel form and finally, unit cells in actual coupon area formed actual resistance as a parallel form as in Eq. (47). From the analytical model, the characteristics of IIT are shown in the Results and Discussions section.

Radiative Resistance in the Space Within Walls and Wire screen

Radiation can be one of the heat transport mode in interstitial area among walls and wire screen. Radiative thermal resistance between two separate surfaces can be expressed as [6],

$$R_{rad} = \frac{T_i - T_j}{\sigma A_a F_{ij}(T_i^4 - T_j^4)} = \frac{1}{4\sigma A_a F_{ij}\overline{T_{ij}}^3} \tag{49}$$

where $4\overline{T}_{ij}^{\,-3} \approx \dfrac{T_i^4 - T_j^4}{T_i - T_j}, \overline{T}_{ij} = \dfrac{T_i + T_j}{2}$

For the thermal resistance among two walls and screen wire, view factor can be obtained from geometrical relationship between infinite flat plane and row of cylinders as in Fig. 5 and Eq(50) [23],

$$F_{iw-w} = 1 - \left[1 - \left(\frac{D_w}{s}\right)^2\right]^{1/2} + \left(\frac{D_w}{s}\right)\tan^{-1}\left[\left(\frac{s^2 - D_w^2}{D_w^2}\right)^{1/2}\right] \quad (50)$$

Where s is the distance between wires.

Radiative thermal resistance circuit can be expressed and assumed screen wire behaves as reradiating surface (i.e. $\dot{q}_w = 0$) as shown in Fig. 6, thus radiative thermal resistance can be expressed as Eq. (51).

$$R_{rad} = \frac{\dfrac{1-\varepsilon_{iw}}{\varepsilon_{iw}A_{iw}} + \left(A_{ow}F_{ow-iw} + \dfrac{1}{\dfrac{1}{A_{iw}F_{iw-w}} + \dfrac{1}{A_{ow}F_{ow-W}}}\right)^{-1} + \dfrac{1-\varepsilon_{ow}}{\varepsilon_{ow}A_{ow}}}{4\sigma\overline{T}_{iw-ow}^{\,3}} \quad (51)$$

The radiative resistance was existed as parallel resistance with air and total contact resistances in a node thus new total thermal resistance in a node can be expressed as Eq.(52),

$$R_{tot,node} = \left(\frac{1}{R_{tot,c}} + \frac{1}{R_{air}} + \frac{1}{R_{rad}}\right)^{-1} \quad (52)$$
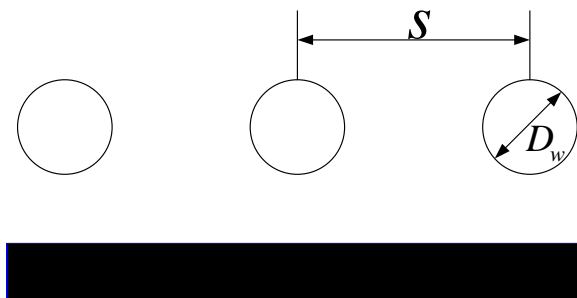
Figure 5 View factor between wall and screen wire.
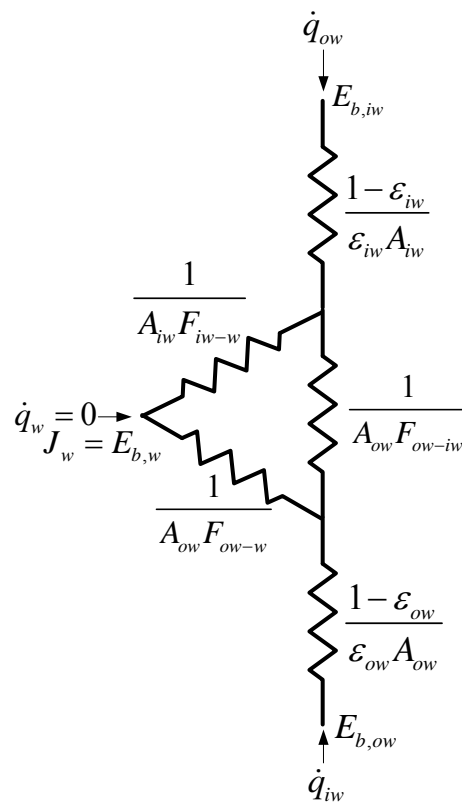
Figure 6 Thermal circuit for radiation among walls and wire in a node.

With new total thermal resistance in a node, total resistance in a unit cell and actual joint thermal resistance and conductance can be expressed with new total as in Eq. (45), (47) and (48) respectively.

From modified model, effect of radiation in total resistance is discussed in the result section.

Multilayer Model

A multilayer model is required for the actual design and optimization. The multilayer model will be able to predict the overall thermal conductance and deformation of wire screen thickness. In a multilayer design, the liner material's selection is important due to its function as a radiation shield as well as a separator for the individual screen layers. In the developed model, the properties of the outer wall were replaced with liner's properties. In the same way, properties of the inner wall on the last layer should be replaced with liner properties. As for properties of the middle layer walls, the liner properties were used.

For resistance calculation, the temperatures of each layer were required. The heat rate can be calculated as shown in Eq. (53). With calculated heat rate, temperatures of each layer can be expressed as Eq.(54).

As shown in Fig. 7, the overall thermal resistance of the multilayer structure can be calculated from the summation of the serial type resistances.

$$Q_{node} = \frac{T_H - T_L}{R_{tot,node}} = \frac{T_h - T_i}{R_{node,i}} \tag{53}$$

$$T_{i+1} = T_i - Q_{node} \cdot R_{node,i+1} \tag{54}$$

The modified model for the multilayer structure included the macro and micro resistances (plastic and elastic), as well as air-gap and radiation resistances.

Parametric Study

One of the best advantages from modeling is that a parametric study can be conducted. Parametric study was executed for the one varied value parameter with other fixed value parameters which can be made the different sets of input parameters (i.e. selected mechanical, geometrical and thermophysical properties). Among the mechanical and/or thermophysical properties, the dominant property of the material that most affect the thermal performance can be determined through this parametric study. With the developed modeling it is possible to find the dominating property of metal material. For non metal material, a different modeling is required.
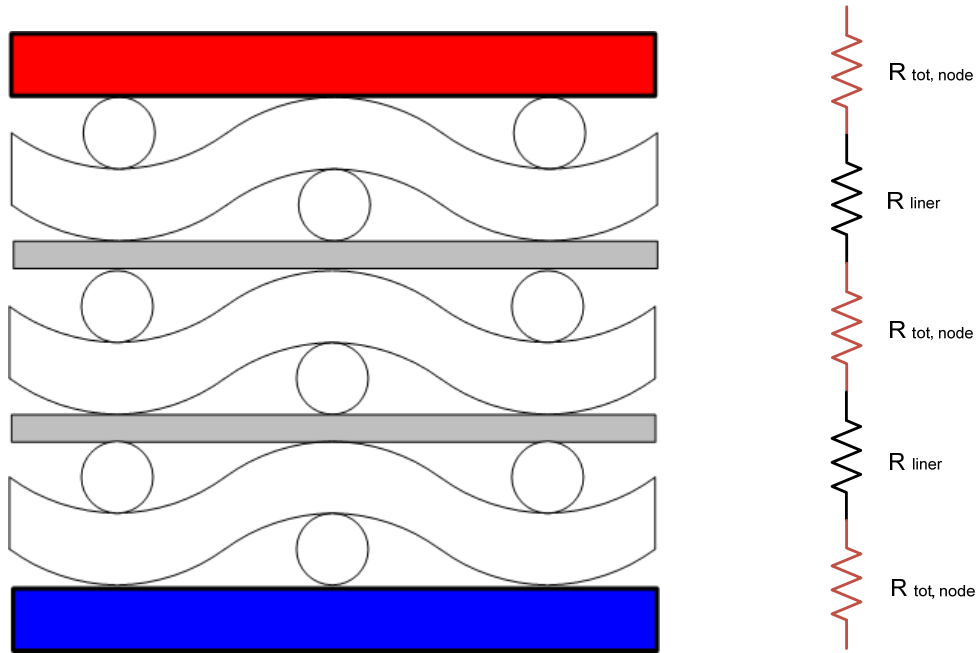
Figure 7 Schematic of the multilayer (three layers) structure and thermal circuit among walls, wire and liner in a node.

CHAPTER III

EXPERIMENTAL INVESTIGATION

Experimental investigation part of this study involved the construction, assembly, and testing of an initial prototype pipe section as an intermediate stage towards a conventional size pipe for actual applications. The test pipe, manufactured by Stress Engineering Houston, TX, was three (3) feet long and made of common pipe steel. The inner diameter of the inner pipe was three (3) inch, the outer diameter of the outer pipe was four (4) inch. As shown in Fig. 8, IICP (Interstitially Insulated Coaxial Pipe) had two layers of insulation which means two (2) stainless steel wire meshes, divided by a thin aluminium liner that acts as a radiation heat transfer barrier comprise the prototype piping and on one end a flange was welded onto the pipe to connect it with the test apparatus. While on the other end there was a drill hole containing threading for attachment to an exterior pipe fitting.

Purpose

The objective of the prototype experiments was to investigate the performance characteristic of the insulation technology that is named "The Interstitial Insulation Technology (IIT)". Its performance can be represented by following thermo physical properties [23].

1) Thermal conductivity, k, is the intensive property of a material that indicates its ability to conduct heat. However, it is more useful to represent the heat transfer ability

Figure 8 IICP-test-section & cross-section view of the test pipe.

using effective thermal conductivity, k_e, when heat transfer through any of these insulation systems may include several modes: conduction through the solid materials; conduction or convection through the air in the void spaces; and, if the temperature is sufficiently high, radiation exchange between the surfaces. Effective therma conductivity depends on the thermal conductivity and surface radiative properties of the solid material, as well as the nature and volumetric fraction of air or void space.

2) Thermal diffusivity, α, the ratio of the thermal conductivity to the volumetric heat capacity is an important property which measures the ability if a material to conduct thermal energy relative to its ability to store thermal energy. Material of large, α, will respond quickly to change in their thermal environment, while small , α, will respond more slowly, taking longer to reach a new equilibrium condition. These properties are highly depend on a special parameter of system, bulk density (solid mass/total volume), which depends strongly on the manner in which the solid materials is interconnected.

The experimental facility was appropriate for simulating deepwater thermal applications. The tests consisted of two parts to measure the thermal properties stated above, 1) steady state and 2) transient testing. The details of the experimental procedure and experimental plans are described below. In each test run, the inner and outer surface temperatures were measured with an Omega 30 gauge – SLE (Special Limited Error) thermocouple. Each surface had twelve (12) temperature reading locations which were spaced at three (3) inch intervals along with the axial direction from inlet to outlet. Fig. 9 shows the prototype pipe after all the thermocouple wires

were attached. These thermocouples were used to measure the axial temperature distributions on the surfaces every second (i.e., the reading rate of the data logger).

Steady State Test

Steady state tests were conducted at several temperatures which were set with the use of a hot water heater. The temperatures were 50, 60, 70, 75 and 80°C with a preset mass flow rate (0.05-0.4 GPM) that allowed the control of the heat flux. At each given inlet temperature, the heat flux could be controlled by the inlet hot water valve and the flow meter which were connected to the hot loop inlet line. With data from the steady state tests, the effective thermal conductivities were computed (see the result and discussion section).

Transient Test

Transient tests were conducted under prescribed hot water temperatures that maintained a free inner pipe flow volume with no mass flow variations. Each test was run at 50, 60, 70, 73, 75 and 80°C for the initial hot water temperature. The temperature measurements were recorded as a function of time, and then the thermal diffusivities were calculated which are shown in the result and discussion section.

Under the above two test conditions, the temperature of the inner and outer surface of the pipe and the hot water and coolant inlet and outlet temperatures were measured with a data acquisition system every one (1) second.

In summary, the results from the steady state tests were plotted as thermal conductivity as a function of heat flux under a given inlet hot water temperature. And

Figure 9 Prototype pipe with thermo couples.

for the transient tests, the thermal diffusivity was plotted as a function of temperature. With the data obtained from these experimental tests, the performance of the IIT was ascertained.

Apparatus Design Overview

The experiment setup was constructed with cold and hot loops to simulate actual working environment with the hot water as the crude oil and the coolant as the seawater. The hot loop was designed so as to control the input heat load by using a hot water inlet valve with a flow meter connected to the hot water source. A built-in temperature controller maintained the hot loop inlet temperature while the cold loop was connected to a coolant bath to maintain the outer surface environment. A schematic of the test apparatus and loops is shown in Fig. 10. Twelve "T" type thermocouples were attached to the inner surface and outer surfaces to measure the temperature. For the cold and hot loops, the inlet and outlet temperatures were measured with two thermocouples within each loop flow line. Preliminary test results, with a relatively large cooling bath, indicated that a new design was required to meet the cooling loads. Therefore, a new cooling bath design was fabricated to satisfy the proper capacity of the coolant bath. The new cooling bath design was a plug-in type cooling bath (i.e., prototype IICP was insert and placed in the coaxial PVC cooling bath).

A six (6) inch inner diameter PVC pipe was used for the coolant bath. The prototype pipe was inserted to PVC pipe with copper coil wrapping which was connected to low temperature circulator, assembly is shown in Fig. 11.

The gap between the prototype piping and the PVC pipe was filled with ethylene glycol. To minimize heat loss, the coolant bath (PVC pipe) and all connected lines were entirely enclosed with air bubble/ fiberglass insulation as shown in Fig. 12.

For the hot loops source, an A.O. Smith water heater was used which had a 66 gallon capacity for a given temperature setting (Fig. 13 top). For the cold loop source, a NESLAB UTL-95 Low Temperature Circulator was employed as shown in Fig. 13 bottom.

Data Acquisition System

For the temperature data collection a National Instruments TC-2095 Data Board was used, which provided thirty two (32) channels for thermo couples. All measurements were displayed via Lab View 7.1. Lab View is a graphical programming development environment based on "G programming" language. It offers interactive control for data acquisition, data analysis and data presentation. Each temperature was recorded by the data acquisition system with measurements taken every one second.

Data Analysis

For steady state testing, once steady state conditions were reached, the temperature data were used to calculate the heat rate from the hot water to the pipe's inner surface
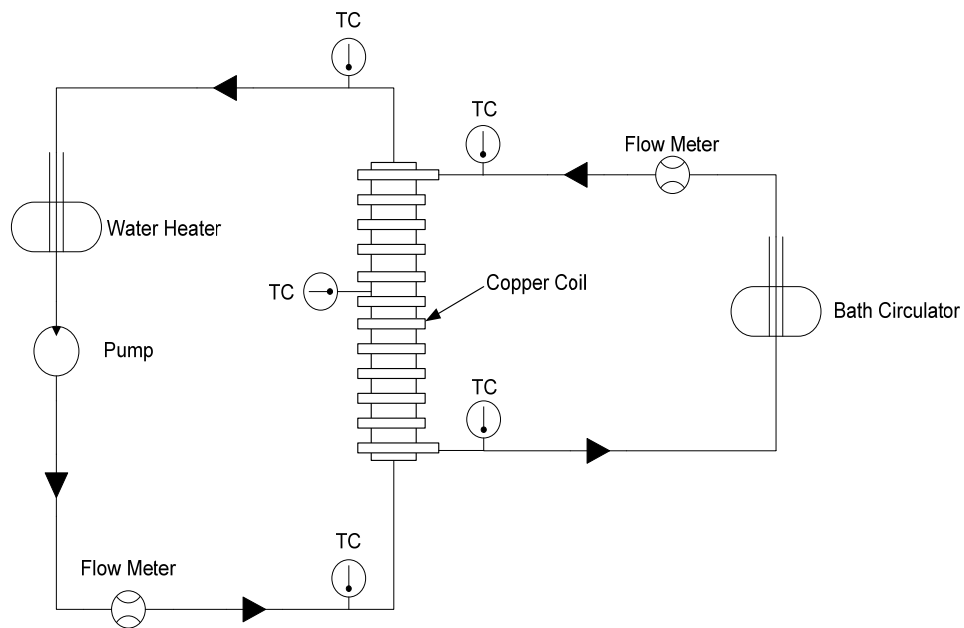
Figure 10 Schematic of test apparatus.
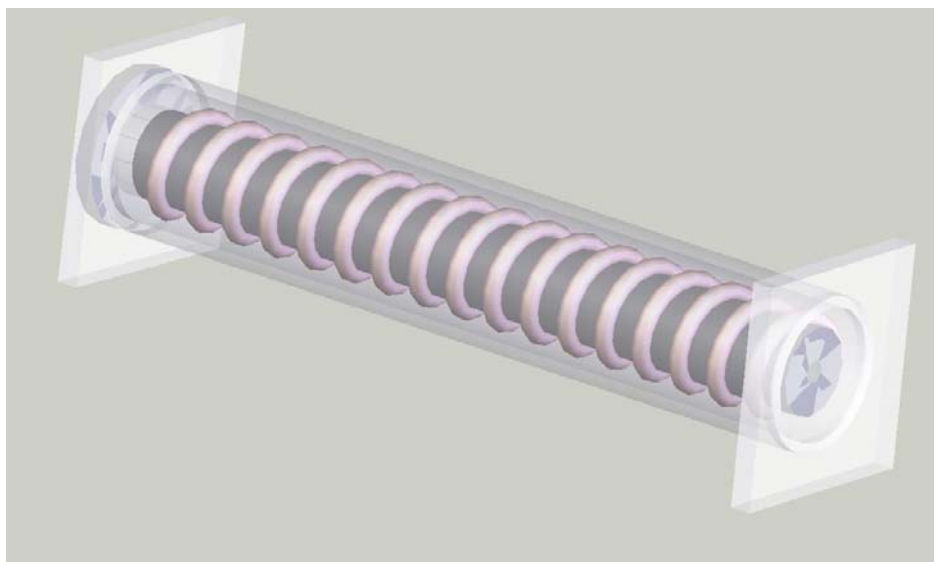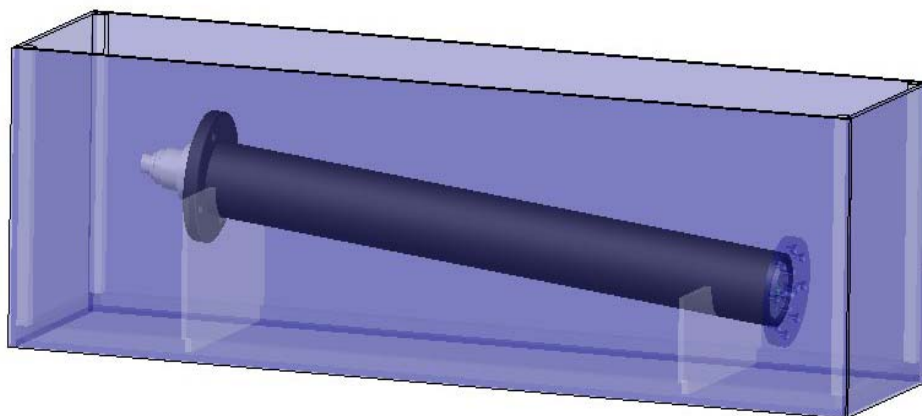
Figure 11 Old (top) and new design (bottom) of cooling bath.

Figure 12 Before(top) and after(bottom) application of insulation.

Figure 13 Hot water heater (top) and low temperature circular (bottom).

by applying Newton's law of cooling. The inlet and outlet hot water temperatures were employed for this calculation. The effective thermal conductivity was calculated from the heat rate and the measured temperature drop across the pipe insulation. The volume flow range for all experiments was 0.05 – 0.4 GPM and the Reynolds number was less than 2300 (i.e. laminar flow). With a constant heat flux condition, the Nusselt number was obtained,

$$Nu = \frac{h_i D_i}{k_w} = 4.36 \tag{55}$$

Therefore, the convection heat transfer coefficient for internal flow can be expressed as,

$$h_i = \frac{4.36 k_w}{D_i} \tag{56}$$

The heat rate for internal flow was computed as,

$$\dot{Q} = h_i A_{is} (T_i - T_o) \tag{57}$$

From an energy balance, the effective thermal conductivity was calculated with the use of the heat rate above,

$$k_{eff} = \frac{\ln(r_{os}/r_{is})\dot{Q}}{2\pi L (T_{is} - T_{os})} \tag{58}$$

In transient testing, when the temperature data from one steady state condition to the desired steady condition were obtained, the free convection heat transfer coefficient, h_o, in the cooling bath was calculated from the temperature difference between the outer pipe surface and the cooling bath temperature. The Biot number was calculated

with the use of the heat transfer coefficient. The Fourier number can be calculated with the use of the Biot number and an equation which contained a Bessel function. Finally, the thermal diffusivity was calculated from the Fourier number. The free convection heat transfer coefficient was then calculated from the Rayleigh number,

$$Ra_L = \frac{g\beta(T_{os} - T_{ss})t^3}{v\alpha_c} \tag{59}$$

For concentric cylinders, Raithby and Hollands [24] developed the following correlations for the effective thermal conductivity,

$$k_{ef} = 0.386k_c \left(\frac{\text{Pr}}{0.861 + \text{Pr}}\right)^{1/4} \left(Ra_c^*\right)^{1/4} \tag{60}$$

where

$$Ra_c^* = \frac{\left[\ln\left(D_s / D_o\right)\right]^4 Ra_L}{t^3 \left(D_s^{-3/5} + D_o^{-3/5}\right)^5} \tag{61}$$

The heat transfer rate was expressed as,

$$\dot{Q} = \frac{2\pi k_{ef} L}{\ln(D_s / D_o)}(T_{os} - T_{ss}) \tag{62}$$

The free convection heat transfer coefficient was obtained as,

$$h_o = \frac{\dot{Q}}{A_{os}(T_{os} - T_{ss})} \tag{63}$$

The Biot number can be expressed as,

$$Bi = \frac{h_o t}{k} \tag{64}$$

From the one dimensional form of the heat conduction equation with initial wall temperature and convective boundary conditions, the equations were developed by Schneider [25] as follows,

$$\theta^* = C_1 \exp(-\zeta_1^2 Fo) J_0(\zeta_1 r^*) = \frac{T_{os} - T_{ss}}{T_{osi} - T_{ss}} \tag{65}$$

where $r^* = r / r_o$,

The discrete value for ζ_n (zeta, eigen value) can be calculated from the Biot number as,

$$Bi = \zeta_n \frac{J_1(\zeta_n)}{J_0(\zeta_n)} \tag{66}$$

The coefficient C_n can be calculated from the Bessel function,

$$C_n = \frac{2}{\zeta_n} \frac{J_1(\zeta_n)}{J_0^2(\zeta_n) + J_1^2(\zeta_n)} \tag{67}$$

From Eq. (65), the solution for the Fourier number can be obtained,

$$\alpha = \frac{Fot^2}{t_{ct}} \tag{68}$$

From the solution for Fourier number, the thermal diffusivity was calculated for a given elapsed cooling time as in Eq. (68).

Experimental Procedure

The experimental tests were conducted with a specific procedure developed for each case. For steady state tests, the hot water temperature had to be maintained with

minimal variance. An A.O. Smith hot water heater was employed which had a large tank capacity and contained two heaters controlled by built-in temperature controllers with thermo stats (upper and lower reservoir part). Natural convection could exist in the reservoir which could cause temperature fluctuations during the heating operation. To obtain a constant flow rate, flow meter readings were frequently required. Even when the experiment reached steady state condition, the variance levels of the temperature measurements were confirmed by statistical tools.

For the transient test, initial steady state conditions were crucial factors, therefore, the same method for temperature variance level checking was performed prior to starting and ending of the experiment run.

CHAPTER IV

RESULTS AND DISCUSSIONS

Analytical Model

In the analytical modeling study, both macro and micro plastic and elastic models were employed. The model included constriction/spreading resistances for an elliptical contact area, the bulk resistance for the wire screen and an air space resistance for a contacting node. Plastic and elastic models for micro contacts and gap resistance models were employed.

To investigate the contribution of each resistance to the overall resistance in a node, total contact resistance and air resistance and the total resistance for a node is plotted as a function of applied pressure as shown in Fig. 14. This figure indicates that the contact resistance decreased as applied pressure increased while the air resistance decreased only slightly. The contact resistance sharply decreased due to increasing contact area. When the applied pressure reached roughly 283 kPa, the contact resistance was lower than the air resistance, and there-after the air resistance dominated the total resistance.

The contact resistances within a node can be classified into either contact resistance by the inner wall-to-wire, the wire-to-wire, or the wire-to-outer wall resistance. In the model, the inner wall-to-wire and wire-to-outer wall had similar properties; therefore, they were similar resistance components. Fig. 15 shows a plot of the total contact resistance and contact resistances for the inner wall-to-wire and wire-to-wire resistances. As shown in the figure, the inner wall-to-wire or wire-to-outer wall contact

created higher resistance than the wire-to-wire contact resistance thus controlling the overall resistance for the range of applied pressures investigated. The resistance in the wire-to-wire contact had a relatively large decrease as 200 kPa was approached as indicated by the changing slope of the curve.

To obtain a better understanding of the contact resistance caused by the wall-to-wire interface, which seems to dominate the overall resistance in the node, a plot of multiple interface resistances is shown in Fig. 16. From Fig. 16, the dominant resistance component at the inner wall-to-wire interface is clearly the microcontact resistance (R_{tmc}: total microcontact) which is highly dependent on the applied interface pressure. The analysis also indicated that the macro constriction ($R_{c,iw}$) and spreading ($R_{c,w}$) resistances at the inner wall and wire were the least dominant resistances, and then this was followed by the microgap resistance ($R_{g,iw-w}$). All of these resistances were located at the inner wall-to-wire interface. To highlight this same behavior within the wire-to-wire interface, Fig. 17 shows these same individual contact and gap resistances at this interface. Even in wire-to-wire contact, the total microcontact resistance ($R_{tmc,w-w}$) seemed to be the dominant resistance parameter, similar to the inner wall-to-wire interface shown in Fig. 16. Again, the least influence at this interface came from the macro constriction and spreading resistances. However, the addition of the bulk wire resistance did cause a lower overall total contact resistance when compared to the inner wall-to-wire interface which is indicated by the solid lines ($R_{c,iw-w}$ and $R_{c,w-w}$) in both Figs 16 and 17. This lower resistance is more prevalent between 230 and 600 kPa of applied pressure. The overall total contact

resistance included all of the resistances which comprise the thermal circuit network (see Fig. 4 for a single node).
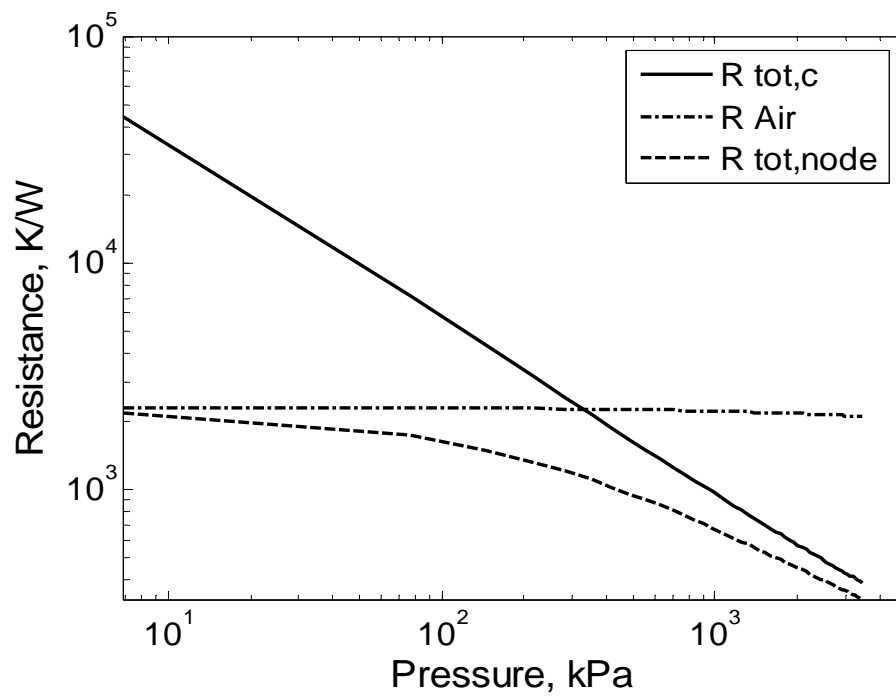
Figure 14 Thermal resistance as a function of applied pressure in a node.
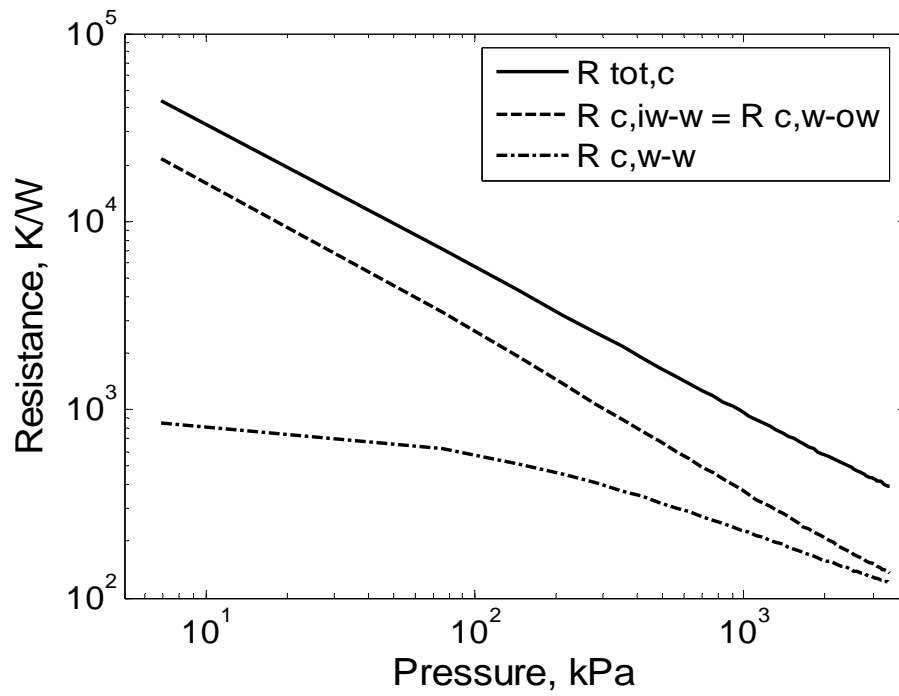
Figure 15 Thermal contact resistances as a function of applied pressure in a node.
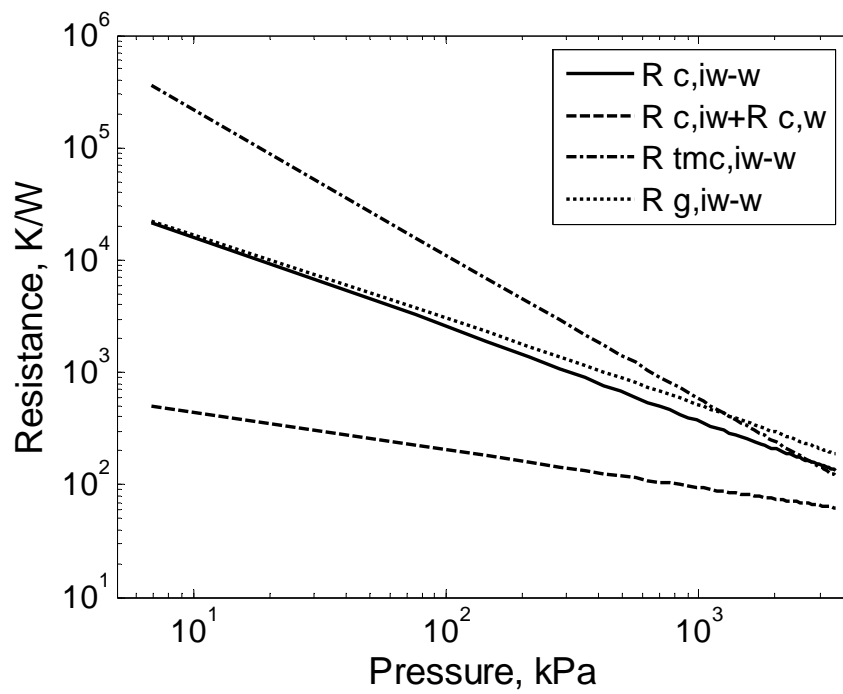
Figure 16 Thermal resistance as a function of applied pressure within inner wall and wire of a node.
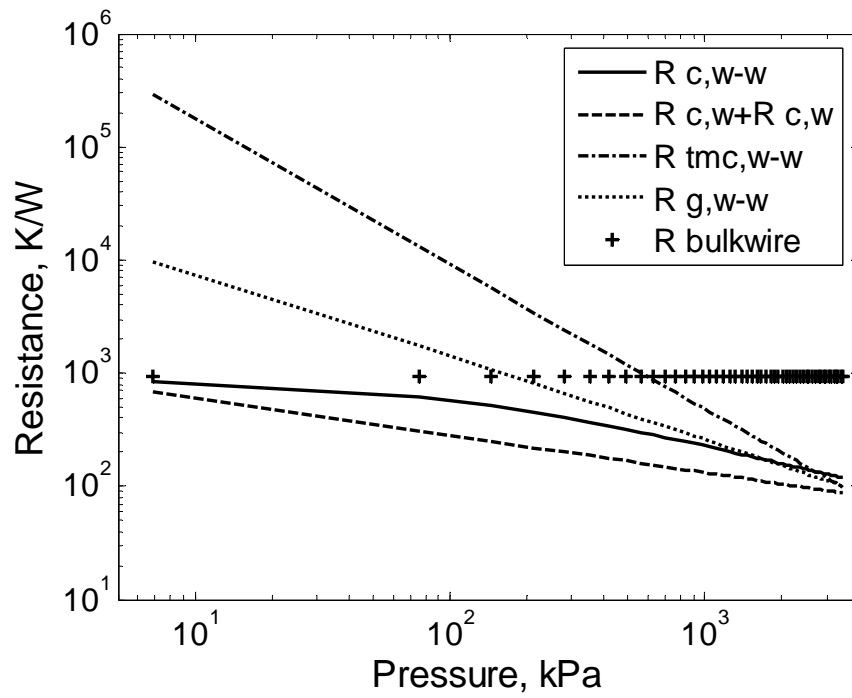
Figure 17 Thermal resistance as a function of applied pressure within wire and wire of a node.

To investigate the effects of contact resistance as a function of applied pressure at a node, a nondimensionalized expression was developed which included macrocontact, microcontact, micro gap, bulk wire and the air resistance in the space between inner and outer wall and within screen mesh, $R_{tot,c} / R_{tot,node}$,

$$\frac{R_{tot,c}}{R_{tot,node}} = 1 + \frac{R_{tot,c}}{R_{air}} \qquad (69)$$

Eq.(69) is plotted in Fig. 18 as a function of applied nominal pressure over the range 1 kPa $\leq$ P $\leq$ 3500 kPa. It seemed from this analysis that the interface contact resistances had a greater influence on the overall resistance over all pressure regions. Further, contact resistances sharply decreased as the applied pressure approached 283 kPa which was mainly caused by the reduction in micro contact resistance.

For comparison, experimental data are also shown along with the model predictions in Fig. 18. The trend indicated a large reduction in contact resistance influence as the pressure was increased up to 690 kPa, then the air resistance began to dominate for pressures greater than 1015 kPa. The comparison indicated that the inclusion of a plastic model for micro contacts was better at predicting the experimental data than the assumption of elastic micro contacts at these higher pressures (RMS errors have been computed).

As shown by Figs. 16 and 17, the resistance due to micro contacts and micro gaps was much larger than other resistances, and thus became the controlling factor for this system. This means that a wire screen can be a proper insulating medium for an interstitially insulated system if the applied pressure is controlled properly.
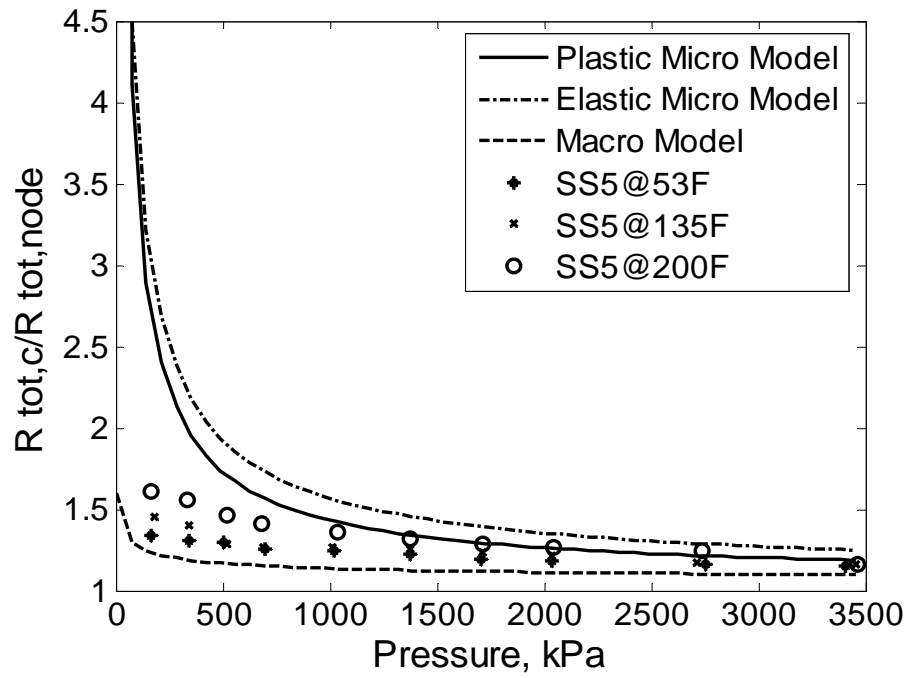
Figure 18 Dimensionless thermal resistance as a function of applied pressure.

The total thermal resistance for three different deformation models is compared with experimental data as shown in Fig. 19. The comparison indicated that the trends for the total thermal resistance variation, which included the effect for plastic and elastic deformations were similar, but that the elastic model showed a higher resistance. The difference between two the contact models was mainly caused by the deformation mode of the contacting asperities in microcontact, and generally rough surfaces tended to follow the plastic model rather than elastic deformation model. However, the elastic macro model by itself had lower resistance and tended to under predict the experimental thermal resistance results.

Fig. 20 shows the thermal conductance for the various models employed in this study as a function of the experimental data. In this plot, a significant under prediction at light pressure range is observed, for micro models especially, for applied pressures under 1500 kPa. This is a similar trend as seem in Fig. 19 for low applied pressures.

As a quantitative comparison between model predictions and experimental data, Table 1 shows the RMS error between these results. For the plastic contact model, the error ranged from 10 to 19%, which happens to be the lowest values. With the assumption of elastic microcontact deformation, the RMS error ranged from 19 to 29%. While these values were higher than for the plastic deformation assumption, they were still lower than for the assumption of just macrocontact without inclusion of microcontact effects. In the macro model (not include microcontact effects), the error ranged from 68 to 78% which was due to the assumption of perfect contact in the

deformed area. Table 2 shows the geometrical and thermophysical properties of the metallic materials that were used for this analytical and experimental study.

In summary, the reason for higher conductance/lower resistance at lighter pressures (light applied load) as compared to the model predictions can be accounted for from visual inspection of the wire screen prior to any testing. In the untested state, pre-deformation was observable at each wire-to-wire interface for each node caused by the stresses of the fabrication process. The applied load due to fabrication formed an initial contact area which results in lower resistance, or higher conductance, when compared to the model predictions. The model predictions did not take into account pre-deformation of any contacting surfaces.
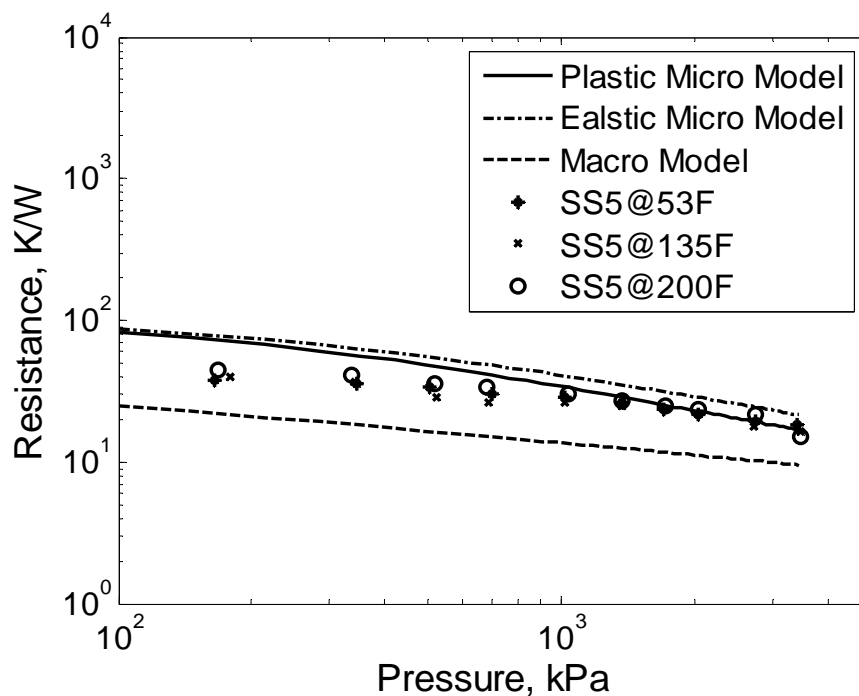
Figure 19 Prediction of thermal resistance for each model compared with experimental data as a function of applied pressure.
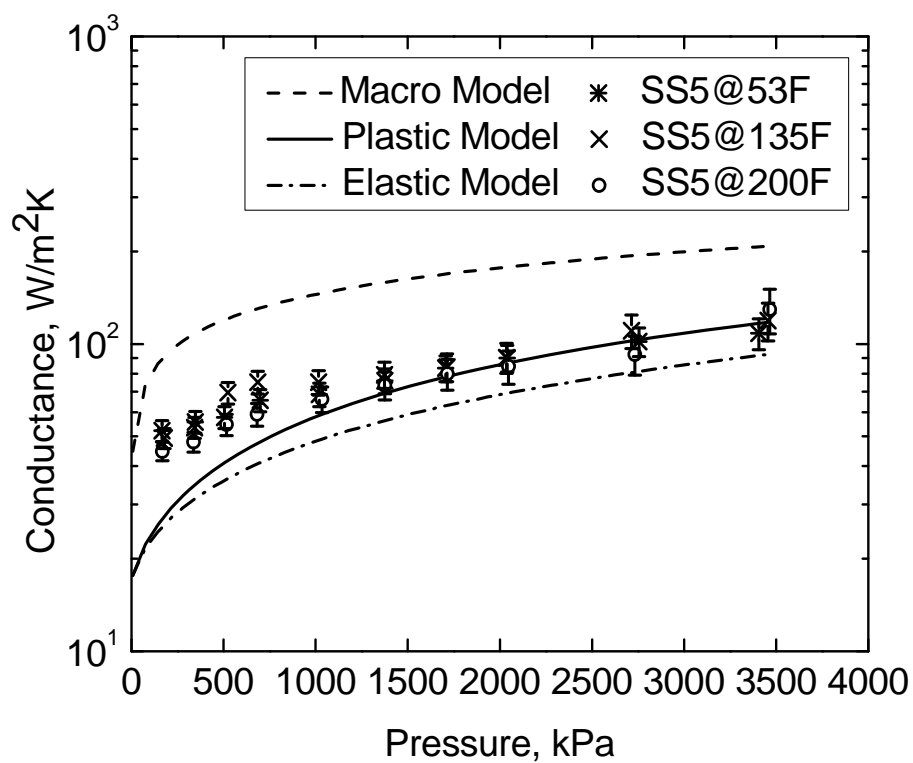
Figure 20 Prediction of thermal conductance for each model compared with experimental data as a function of applied pressure.

Table 1   **RMS error between the experimental data and models**

Model	53°F	135°F	200°F	Average
Elastic Micro	29	29	19	26
Plastic Micro	19	19	10	16
Macro	68	69	78	72

Table 2   **Properties of materials [23]**

Material	Poison's Ratio	Modulus (GPa)	Roughness (μm)	Absolute Asperity Slope	Thermal Conductivity (W/mK)	Emissivity
Steel 4140 P110 (Inner or Outer Wall)	0.3	207	1.5	0.0938	42.7~46.7	0.44
Stainless Steel 316 (Mesh Screen)	0.3	190	0.4	0.0471	16.3~16.5	0.22

C(Length between nodes, mm)		25.4	D_w (Wire Diameter, mm)		0.925	

Radiative Resistance Model

As one of the heat transfer modes within the interstitial space, thermal transport by radiation was included in the model. Radiation heat transfer was placed in the thermal circuit as a parallel resistance along with the total contact resistance and air resistance. To determine the contribution of each resistance to the overall resistance in a node; the total contact resistance, air resistance, radiative resistance and the total resistance for a node were plotted as a function of applied pressure as shown in Fig.21. This figure indicated that the contact resistance dominants in the low pressure range (~25Kpa) and linearly decreased as applied pressure increased, meanwhile, the radiative and air resistance decreased only slightly. Therefore, it was observed that the total resistance in a node was highly dependent on the change of contact resistance which was similar to results without radiative resistance being added. After adding the radiative mode, the analysis showed a higher thermal conductance (lower thermal resistance) at the lower pressure range as shown in Fig 22 and 23. After the inclusion of the radiative mode into the model, the under prediction of thermal conductance at the light pressure range was decreased while at the high pressure range its change was negligible. This is a positive effect to the prediction of the thermal performance.
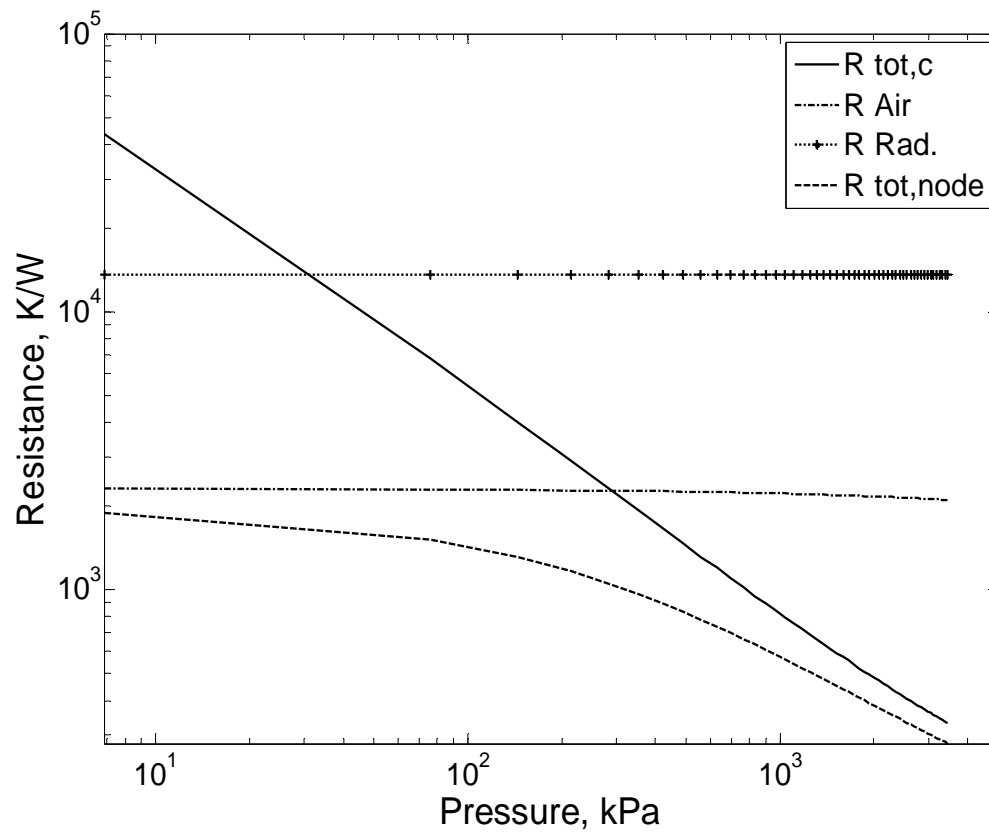
Figure 21 Thermal Resistance as a function of applied pressure in a single node.
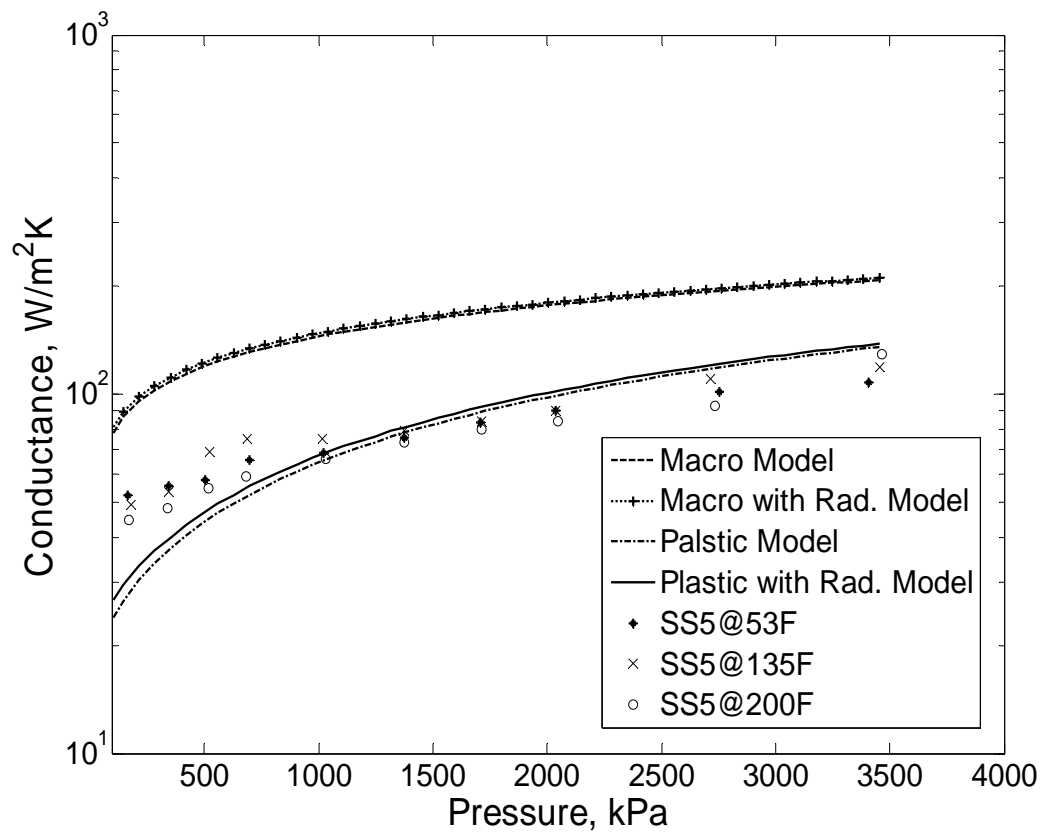
Figure 22 Prediction of thermal conductance for each model with /without radiation model and compared with experimental data as a function of applied pressure.
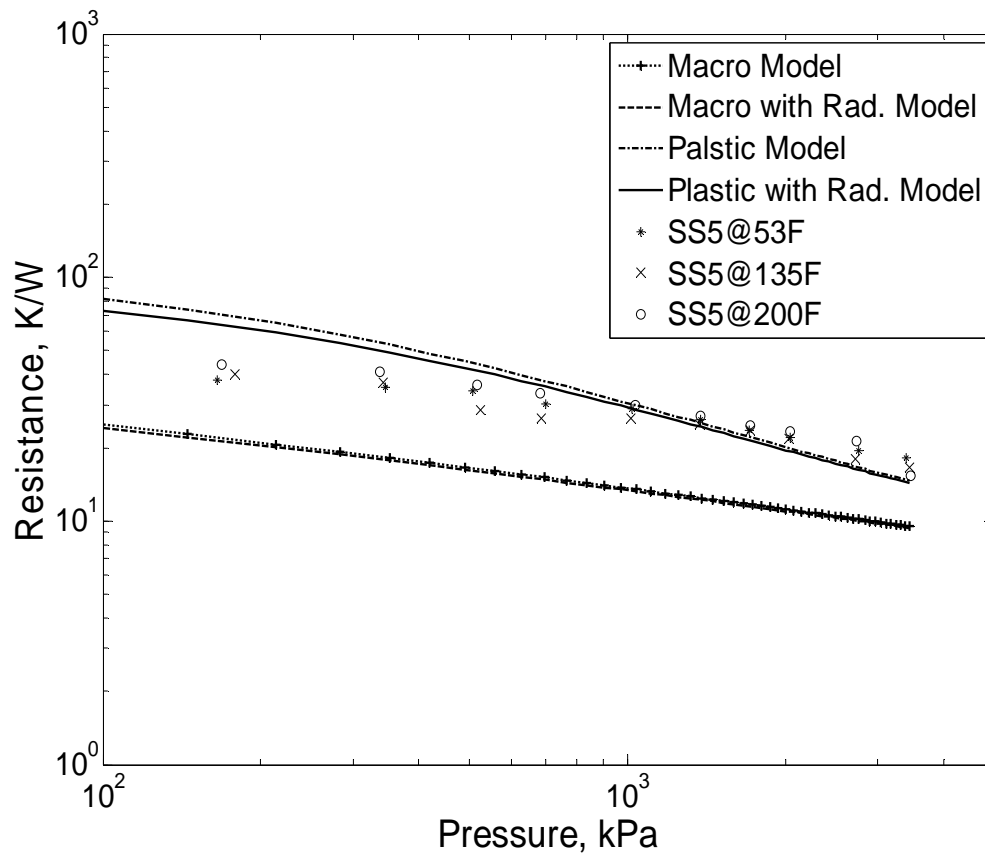
Figure 23 Prediction of thermal resistance for each model with /without radiation model and compared with experimental data as a function of applied pressure.

Comparison with Other Mesh Numbers and Materials

An analytical model was developed to predict the thermal performance of the interstitial insulation technology with different mesh material and mesh number (i.e. number of mesh per square inch). With experimental data [5] and material properties, as shown in Table 3, a comparison between model predictions and the experimental data was conducted.

With the developed model, applied to an Inconel Alloy with a mesh number of 5, a comparison of the experimental and theoretical thermal conductance values as a function of applied pressure was conducted and is shown in Fig. 24. The trend for the predicted values correlated very well with experiment data; however, an under-prediction of the conductance occurred in low pressure range as shown previously with Stainless Steel 316. At an interface pressure of 172kPa, the difference in thermal conductance between model prediction and experimental data was 15.2 W/m^2K while its difference was reduced to $0.91 W/m^2K$ at 2080 kPa.

Fig. 25 shows a comparison between model predictions and experiment data for Stainless Steel and Inconel at a mesh number of 5, and Titanium material for a mesh number of 9. The model predicted the thermal conductance very well with the given pressure range tested. As a quantitative comparison, between model prediction and experimental data, the RMS error was calculated for each material which is shown in Table 4. For Inconel, the RMS error was 10.5% which was the lowest among the three materials while the Titanium mesh material had a value of 21.9 % (the highest error computed).

For Titanium material at different mesh numbers (e.g., 9, 14 and 18), a comparison between predicted and experiment data for thermal conductance as a function of applied pressure is shown in Fig. 26. As Fig. 26 reveals, as the number mesh increased, the difference between model predictions and experimental data increased noticeably at low interface pressures. Again, a possibility for this effect is the observed pre-deformation at the wire-to-wire interface as the number of nodes increased; this caused the apparent area to increase.

Table 3   Properties of screen mesh material [5, 23]

Material	Mesh number	Thermal conductivity W/mK at 366K	Young's Modulus GPa	Wire Diameter mm
Inconel	5	9.8	207	0.819
Titanium	9	22.3	116	0.812
	14	22.3	116	0.406
	18	22.3	116	0.616

Table 4   RMS error between the experimental data and models

Material	Mesh Number	RMS
SS 316	5	13.6
Inconel	5	10.5
Titanium	9	21.9
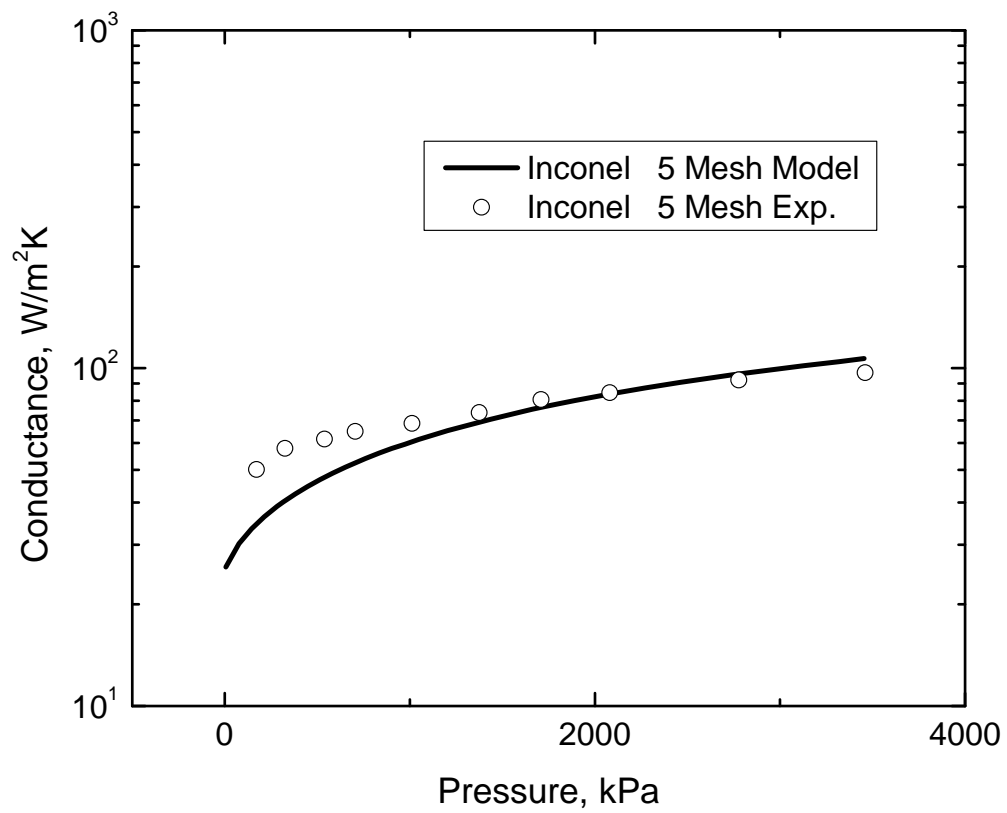
Figure 24 Prediction of thermal conductance of Inconel wire mesh for model compared with experimental data as a function of applied pressure.
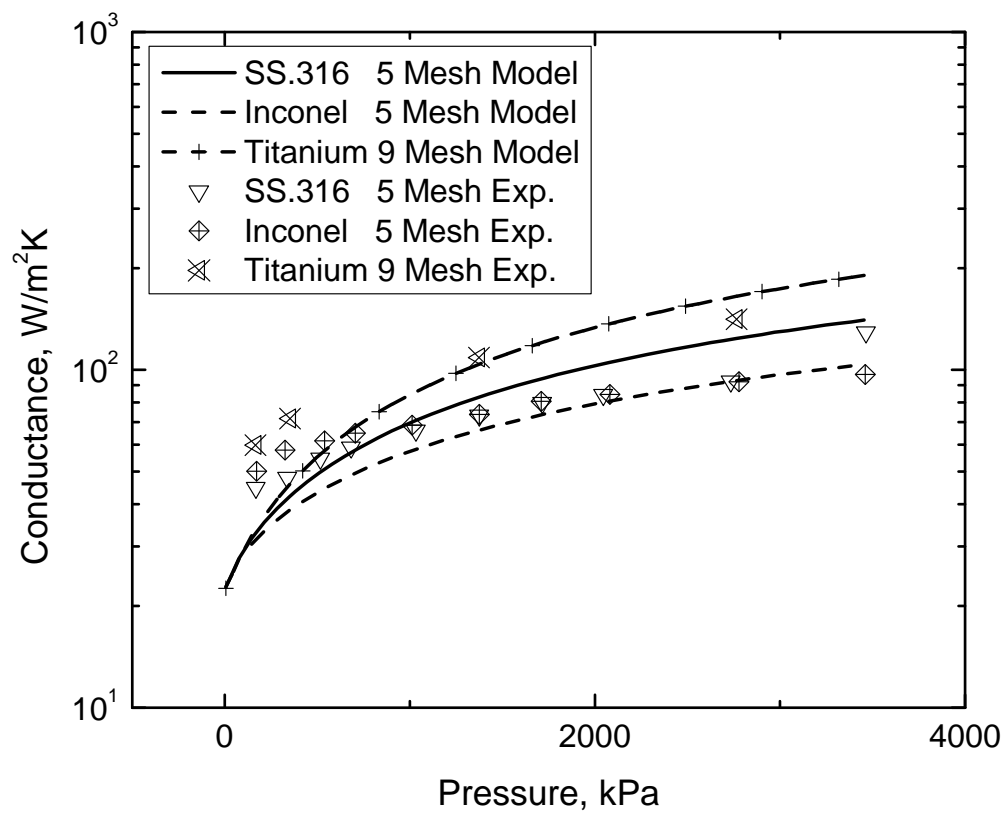
Figure 25 Prediction of thermal conductance of different mesh material for model compared with experimental data as a function of applied pressure.
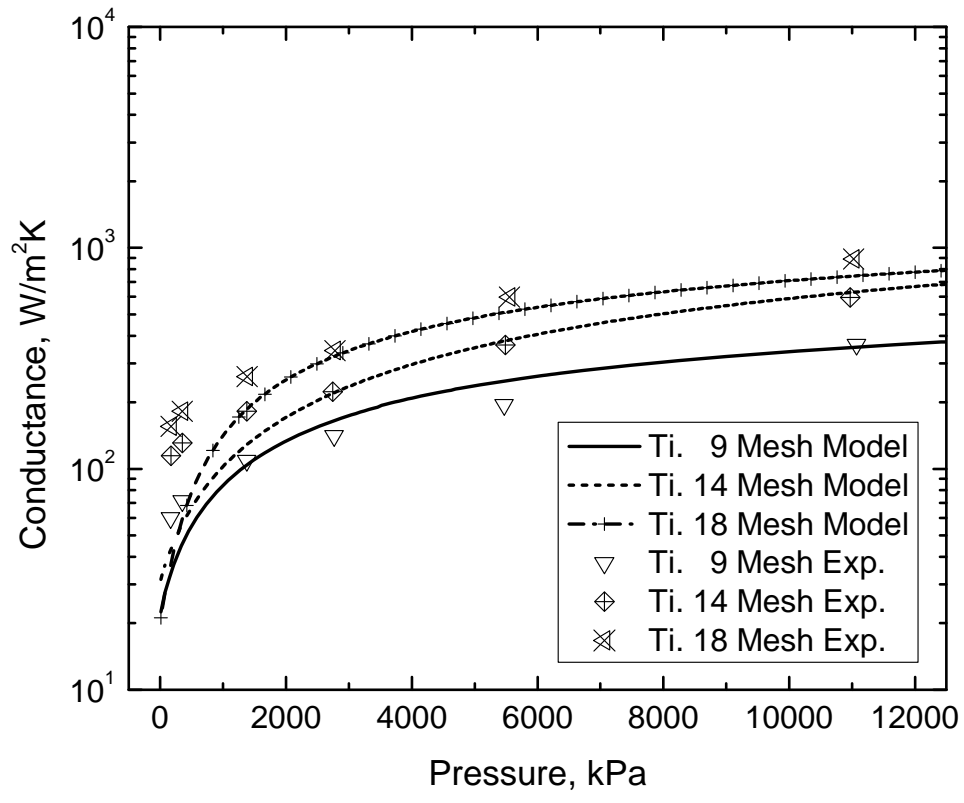
Figure 26 Prediction of thermal conductance of different mesh size of Titanium wire mesh for model compared with experimental data as a function of applied pressure.

Multilayer Model

In real applications, design performances for the IIT are important. Geometrical factors play a pivotal role in the design's performance; therefore, determination of the number of layers is an important parameter to identifying the critical thickness. This helps to achieve the optimum performance at the lowest cost. Fig. 27 shows the thermal conductance as a function of pressure. Each line represents the number of layers from a single screen wire mesh to fifty (50) layers. As the number of layers increased, thermal conductance of the IIT structure decreased. In Fig. 27, the conductance of a single layer at an applied interface pressure of 145Kpa was calculated as $27.5W/m^2K$, $3.3W/m^2K$ for eight (8) layers and $1.6W/m^2K$ for sixteen (16) layers. These multilayer conductance values showed a big decreased; however, the rate of decrease in conductance (i.e., $\Delta h_{i-i+1} = h_i - h_{i+1}$), by adding each additional layer, decreased as the number of layers increased. For instance, the decrease in conductance between a single and double layer was $14.1\ W/m^2K$, eight and nine layer was $0.36W/m^2K$ and sixteen and seventeen was $0.09W/m^2K$ while a linear increase in thermal resistance was observed as the applied pressure increased as shown in Fig. 28. In this figure, the resistance for a single layer was $71\ K/W$, it increased to $146\ K/W$ by $75\ K/W$ with the addition of one more layers and then, $75.7\ K/W$ was resistance increase due to adding one more layer between sixteen to seventeen layers. The rate of increase in resistance (i.e., $\Delta R_{(i-1)-i} = R_{i+1} - R_i$) was observed as nearly constant and thermal resistance was more sensitive to the applied pressure due to greater deformation, which resulted in a contact area increase.
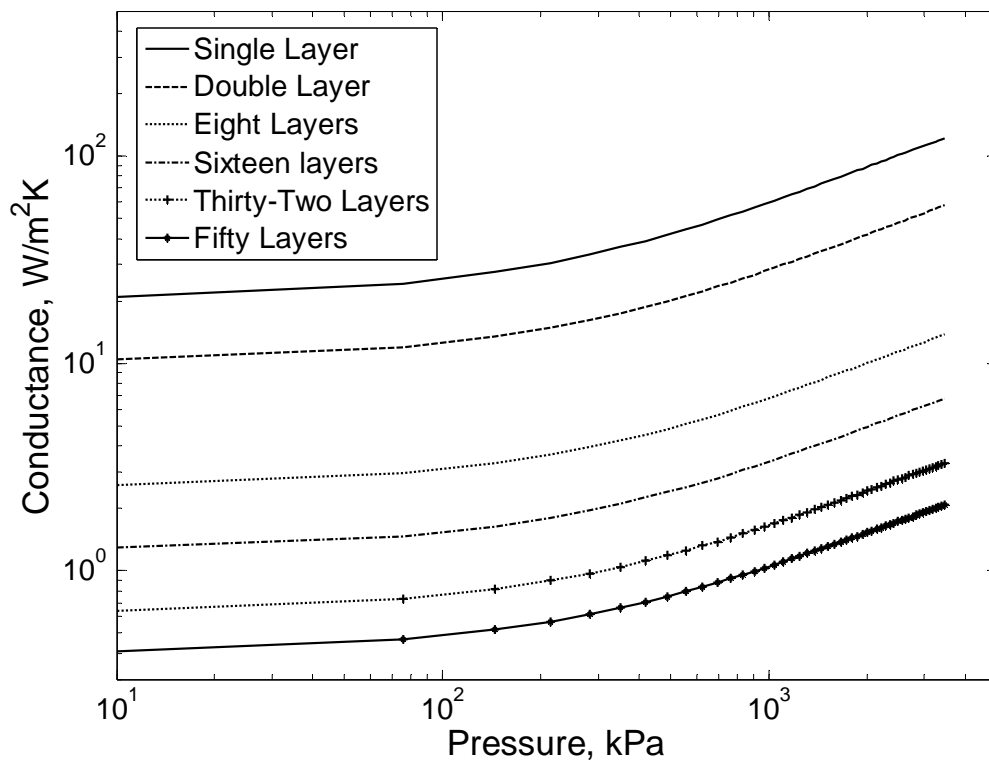
Figure 27 Thermal conductance of multilayer as a function of applied pressure.
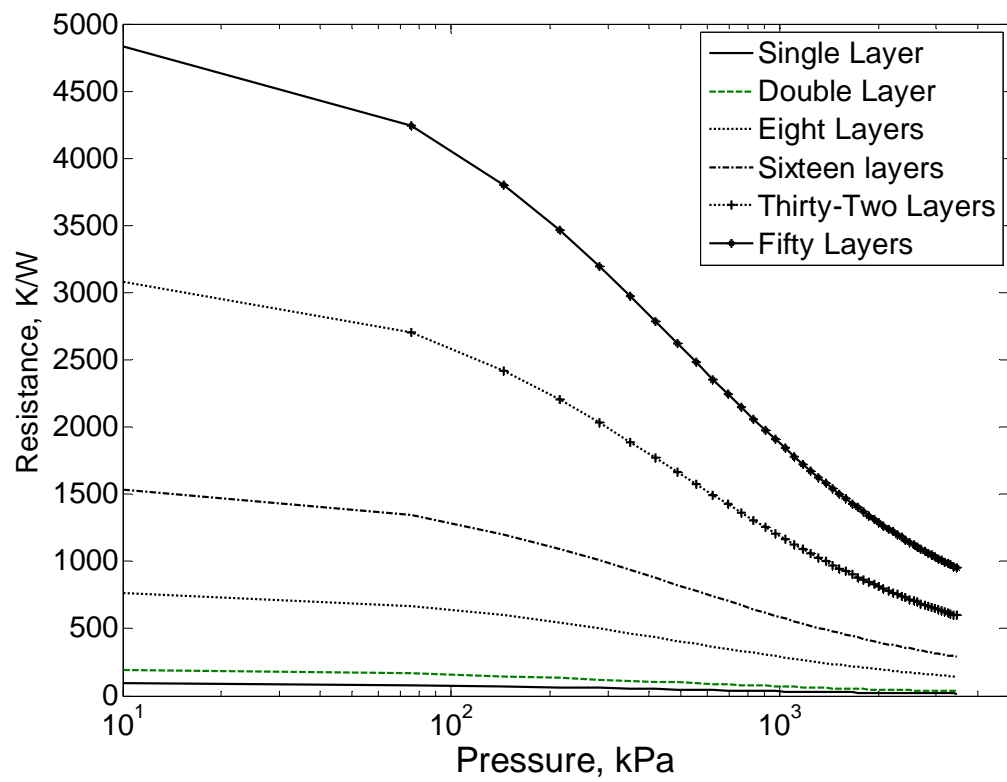
Figure 28 Thermal resistance of multilayer as a function of applied pressure.

Fig. 29 shows the total thickness of each multilayer structure as a function of the applied interface pressure. It indicates that the amount of structural deformation can be attributed to the greater compliance of the layered structure.

The effective thermal conductivity can be calculated by the following equation;

$$k_{eff} = h \cdot t \tag{70}$$

The effective thermal conductivity of a multilayer structure as a function of applied pressure is shown in Fig. 30. At 145KPa interface pressure, the effective thermal conductivity of a single layer was $0.050 W/mK$, while its value was $0.059 W/m^2K$ for an eight layer structure and $0.060 W/m^2K$ for sixteen layer configuration. The change in effective thermal conductivity value by adding one additional layer decreased as the number of layers increased. For instance, the change in thermal effective conductivity value ($\Delta k_{eff,i+1-i} = k_{eff,i+1} - k_{eff,i}$) was $0.005 W/m^2K$ for a single to double layer, $0.000126 W/m^2K$ for an eight to nine layer structure and $0.000019 W/m^2K$ for sixteen to seventeen layer structure at 145KPa interface pressure.

In summary, an optimal overall thickness can be found from the use of the multilayer model. As the number of layers increased, overall thermal conductance was decreased (resistance increased); however, the rate of deduction was reduced after sixteen layers thus its effectiveness by adding more layers was decreased. This can be observed easily from the effective thermal conductivity comparison between eight layers and sixteen layers case as a function of interface pressure as shown in Fig. 27.
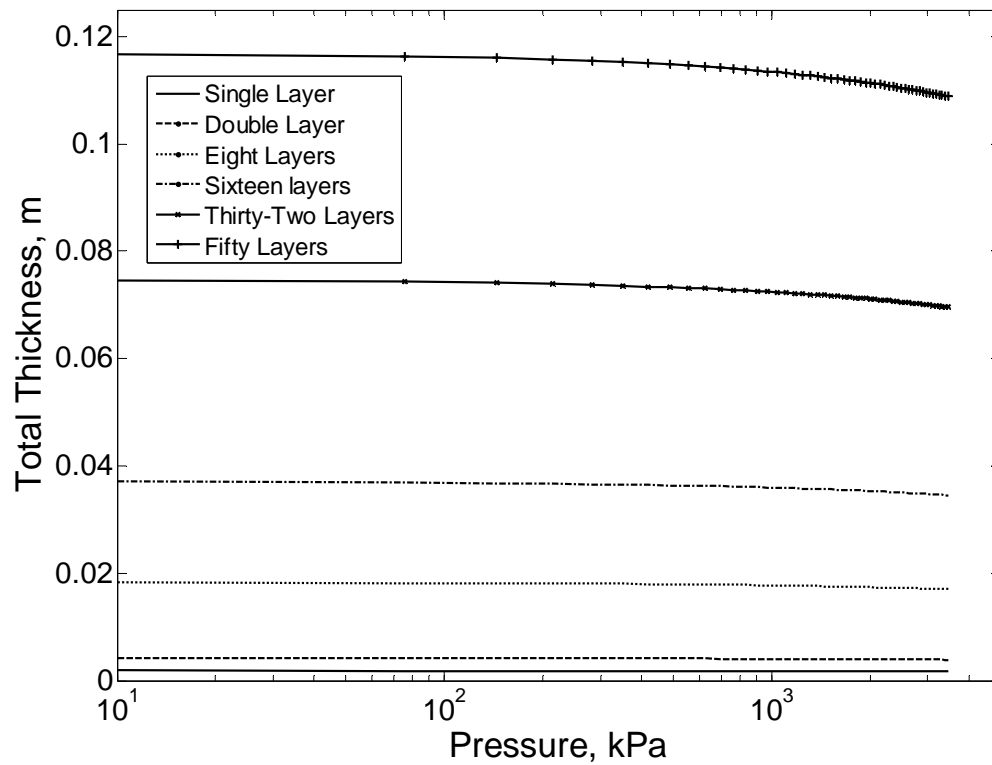
Figure 29 Total thickness of multilayer as a function of applied pressure.
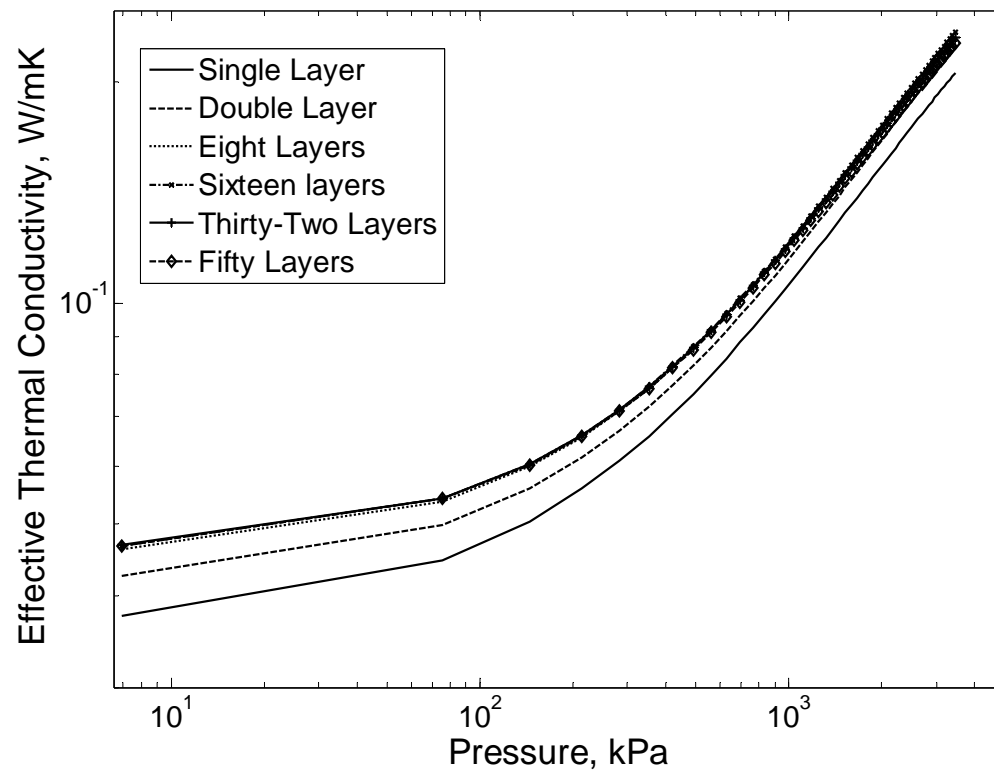
Figure 30 Effective thermal conductivity of multilayer as a function of applied pressure.

Parametric Study

A parametric study was conducted to determine the influence of the variation in geometrical, mechanical and thermophysical properties on the overall thermal conductance of a single layer. The parametric study was conducted by choosing to vary one parameter while holding the remaining parameters constant. The geometrical property chosen was the surface roughness, σ, the mechanical property was Young's modulus, E, while the thermophysical properties selected were thermal conductivity, k, and surface emissivity, ε. All these properties are influential parameters in choosing the optimum material for the application design. To determine the most dominant parameter among the selected parameters, each was changed by 10, 20 and 30% from nominal value as shown in Table.5.

For the 10% case, relatively big reduction in thermal conductance was observed from thermal conductivity parameter case while negligible reductions were observed from other parameter cases as shown in Fig. 31. When thermal conductivity was varied parameter, thermal conductance reduction value was $2.66\ W/m^2K$ at 144kPa, it increased as applied pressure increase which was $13.55 W/m^2K$ at 3454kPa. Fig. 32 shows thermal conductance percent differences between the chosen nominal parameter value and a ten percent (10%) change in its value. From Fig. 32, the percent reduction in thermal conduction as a function of pressure for each parameter can be identified easily.

Reduction by varying thermal conductivity increased up to 9.5 percent (%) at 900kPa, and then negligible increases were observed thereafter. Other parameters

affected the reduction by 1.7 percent. For the emissivity case, its reduction was decreased as pressure increased, which had a 1.6 percent reduction at the low-end pressure (6.8 kPa) and 0.23 percent at the high-end pressure (3454 kPa), repectively. When each parameter was varied by twenty percent (20%), the overall thermal conductance as a function of interface pressure is shown in Fig. 33. Thermal conductance was observed as the most affecting parameter on overall conductance among the selected parameters like in 10% case and conductance reduction was $27 W/m^2 K$ at 3454 kPa. Fig. 34 shows percent change in thermal conductance as a function of interface pressure with twenty percent (20%) variation in each parameter. When thermal conductivity was changed, an upper limit of 19.5 percent (%) reduction in thermal conductance can be expected and for the other parameters only 3.1 percent reduction can be expected. When roughness was varied, the reduction in thermal conductance increased up to 3.17 percent at 489kPa, and then it decreased as the interface pressure increased. For 30% parameter changes, Fig. 35 shows thermal conductance as a function of pressure when the selected parameters were changed one after another. Similar to the 10 and 20% varying cases, thermal conductivity was the most influential parameter on thermal conductance, it had a 5.3 $W/m^2 K$ reduction at 6.8 kPa and $40.6 W/m^2 K$ reduction at 3454 kPa. When reduction was plotted in percent difference from nominal conductance as shown in Fig. 36, up to a 29.3 percent reduction can be expected by varying thermal conductivity. For Young's modulus, the reduction was increased up to 1.05 percent at 75.8kPa interface pressure, and then it

decreased with a negative reduction (increase in conductance) up to -0.75 percent. However, the reduction due to Young's modulus was small enough to neglect.

In summary, a parametric study was conducted from the developed model and thermal conductivity, k, was the most affecting parameter among the selected parameters such as surface roughness, σ, Young's modulus, E, and surface emissivity, ε. Each selected parameter showed its change as a function of interface pressure, but not to the extent as thermal conductivity.

Table 5   **Properties of selected materials for parametric study**

Walls/Wire	Nominal	10%	20%	30%
Thermal Conductivity W/mK	46.7/16.5	42.03/14.85	37.36/13.2	32.69/11.55
Surface Roughness μm	1.5/0.4	1.65/0.44	1.8/0.48	1.95/0.52
Young's Modulus GPa	207/190	227.7/209	248.4/228	269.1/247
Surface Emissivity	0.44/0.22	0.396/0.198	0.352/0.176	0.308/0.154
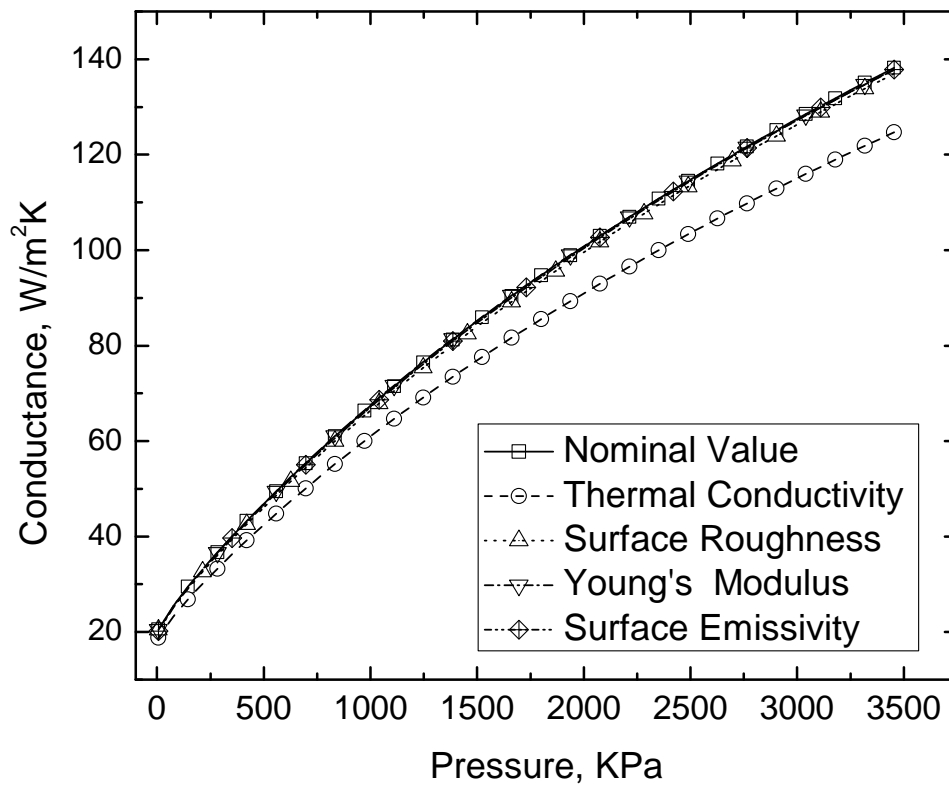
**Figure 31 Thermal conductance on each parameter varies by 10%
as a function of applied pressure.**
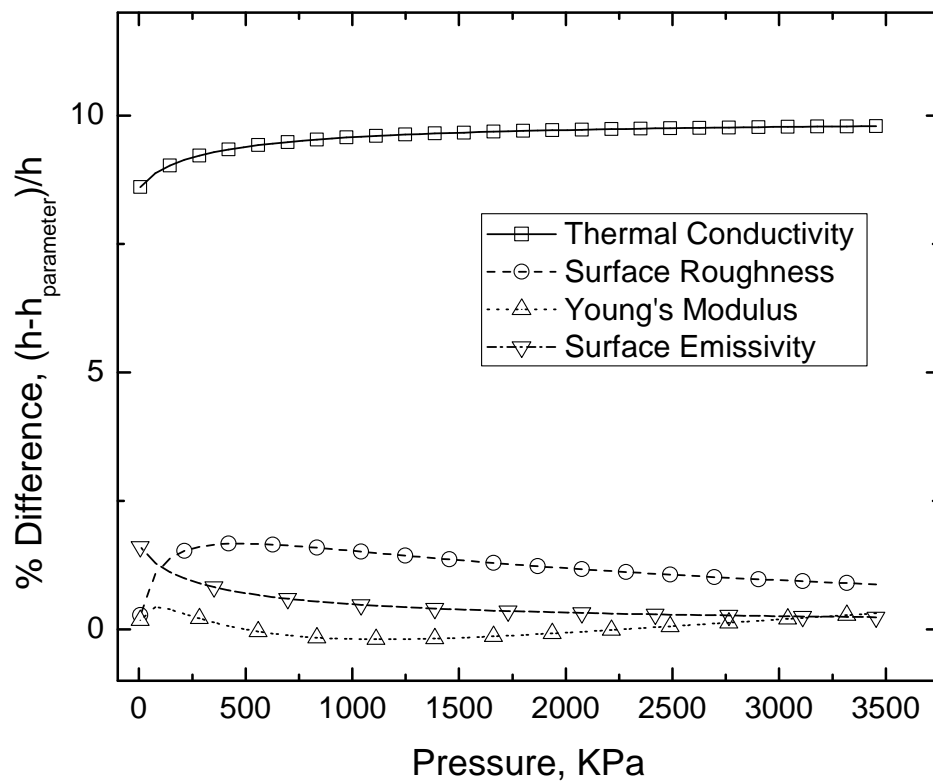
**Figure 32 Thermal conductance difference by 10% varying parameter
as a function of applied pressure.**
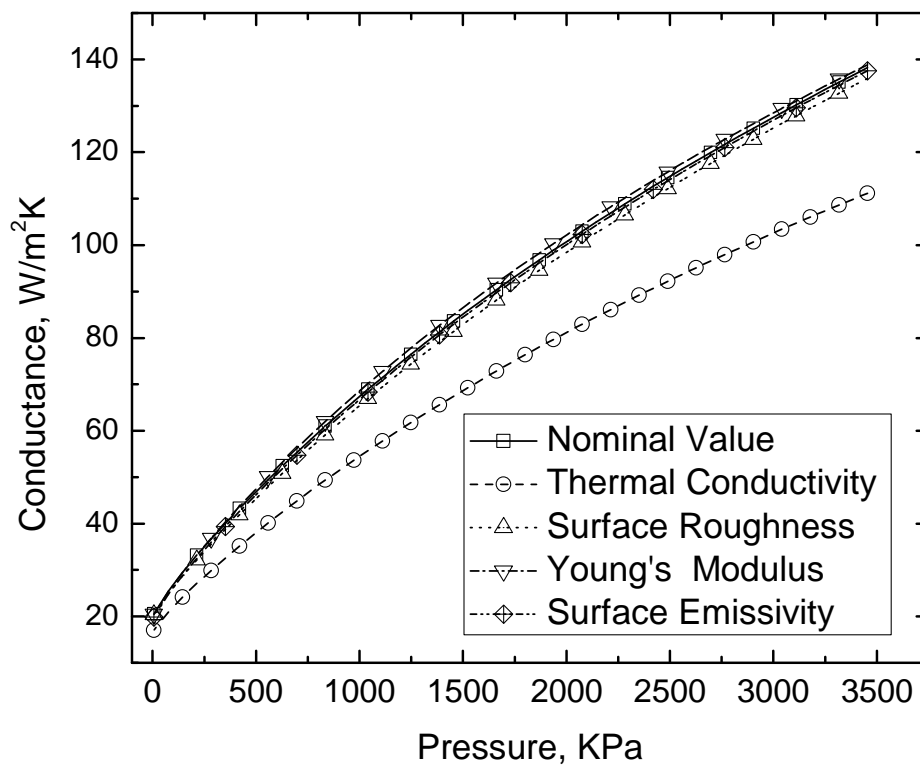
Figure 33 Thermal conductance on each parameter varies by 20%

as a function of applied pressure.
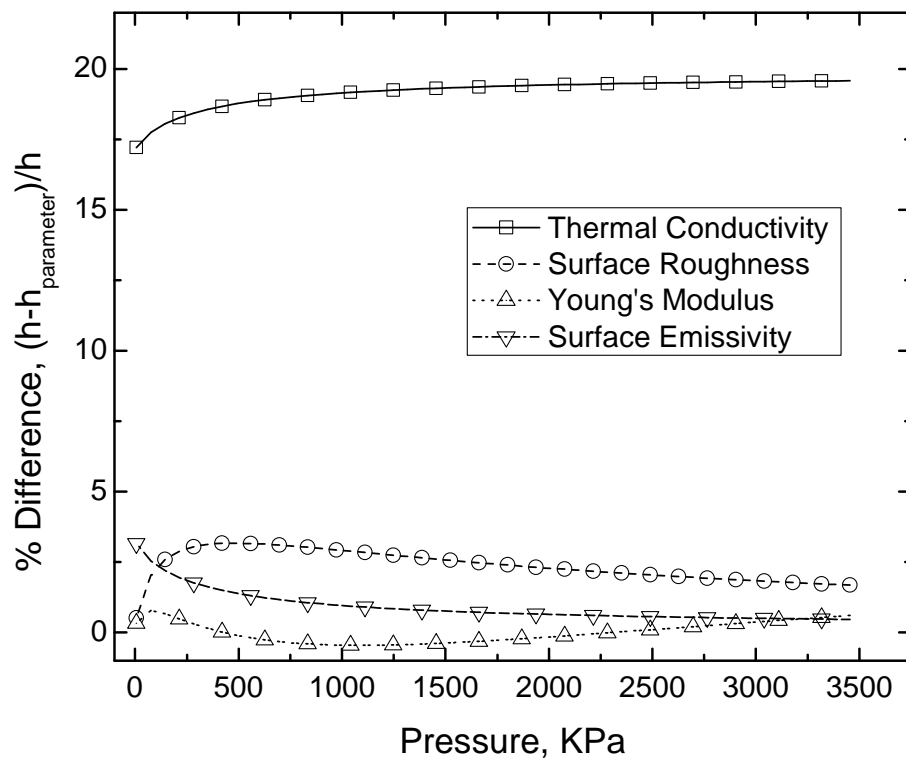
Figure 34 Thermal conductance difference by 20% varying parameter as a function of applied pressure.
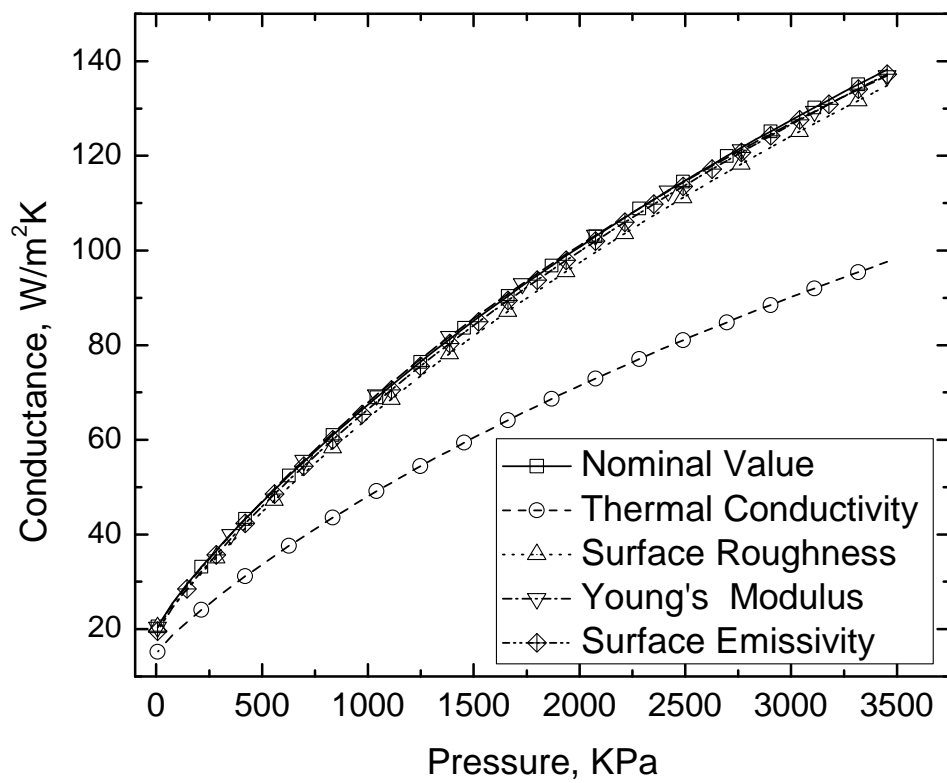
Figure 35 Thermal conductance on each parameter varies by 30%

as a function of applied pressure.
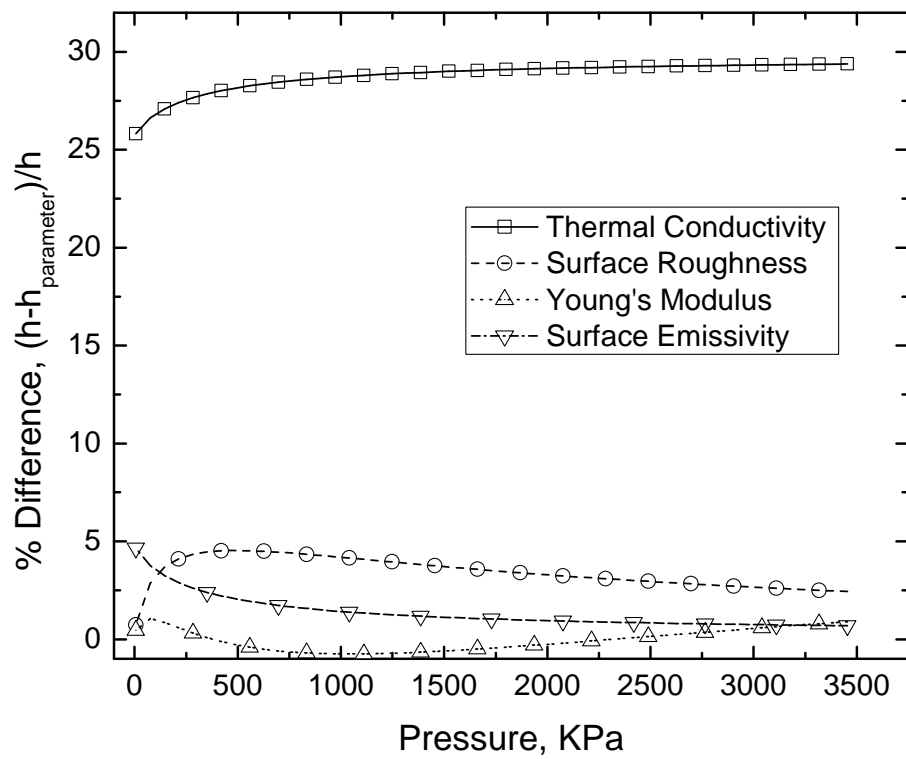
Figure 36 Thermal conductance difference by 30% varying parameter as a function of applied pressure.

Prototype Experiment

Steady State Test

Steady state experimental results compared the effective thermal conductivity of the insulation system to the flow fluid temperature or heat rate. The effective thermal conductivity, k_e, variation is shown in Fig. 37 as a function of incoming hot water temperature at five different volumetric fluxes (gallons per minute). At the lowest in-flow water temperature, 50°C, the effective thermal conductivity, k_e, had a relatively large variation which ranged from 0.084 W/mK to 0.017 W/mK as the volume flux was changed from 0.1 GPM to 0.4 GPM. The difference between 0.1 GPM and 0.4 GPM was 0.066 W/mK. As the in-flow temperature was increased, the effective thermal conductivity difference between the lowest and highest volume flux decreased, for instance, at 80°C the difference was 0.024 W/mK. The effective thermal conductivity decreased as temperature increased. As the volume flux increased, the effective thermal conductivity changed as the temperature was reduced.

The effective thermal conductivity, k_e, as a function of heat rate (W) at five different in-flow hot water temperatures is shown in Fig. 38. At the lowest heat rate (10W), the effective thermal conductivity had relatively small differences among the five different temperatures. For a given heat rate condition, the thermal conductivity decreased as the incoming fluid temperature increased (e.g. at 10W), the lowest k_e was 0.011 W/mK, while the highest value was 0.019 W/mK with a difference of 0.008 W/mK. The effective thermal conductivity increased as the heat rate was increased at

the same temperature condition. For instance, at 80°C in-flow temperature, k_e increased from 0.011 to 0.05 W/mK as the heat rate changed from 10 to 46W.

For comparison of effective thermal conductivity for IIT to air, the dimensionless thermal conductivity ratio, k_{eff}/k_{air}, is shown in Fig. 39 as a function of mean wall temperature of the pipe walls for five different volumetric fluxes. The effective thermal conductivity for the IIT had its highest values for volumetric fluxes equal to 0.1gpm and 0.15 gpm (275% and 150%, respectively). However, the effective thermal conductivity showed large decrease as the temperature was increased. As the inflow rate was increased, the dimensionless thermal conductivity ratio decreased. At lower inflow rates there was a significant decrease in the dimensionless thermal conductivity ratio while it was nearly constant as the volumetric flux was increased.

For comparison purposes, Fig. 40 shows the thermal conductivity ratio data, k_{eff}/k_{air}, for coupon tests previously conducted [5] and the pipe prototype test data for the current experimental investigation. The thermal conductivity values at pressures of 165 and 351 KPa and mean interface temperature of 5ºC were selected from the coupon tests for this comparison. These interface pressure values were closest to the experimental environmental conditions conducted in phase II. Under these values the calculated ratios for the coupons ranged from 0.27 to 0.32. The lowest ratio value computed from the pipe prototype tests was 0.38; this represents a ratio difference of 0.11 from the coupon tests. However, the estimated environmental pressure for the pipe prototype tests was approximately 1 atm (101KPa); this is approximately two times lower than the pressure value for the coupon tests. This difference in pressure was

caused by the pipe's construction process. Therefore, this limits a direct one-to-one comparison between the values. But if one takes into consideration the experimental uncertainty in the experimentally measured thermal conductivity values the ratio difference becomes less significant. In conclusion, the values for the thermal conductivity ratio are very similar even thou slight differences exist. For comparison the effective thermal conductivity of IIT (0.017 to $0.079\,W/mK$) with commercial product, conductivity values of commercial materials are shown in Table. 6.
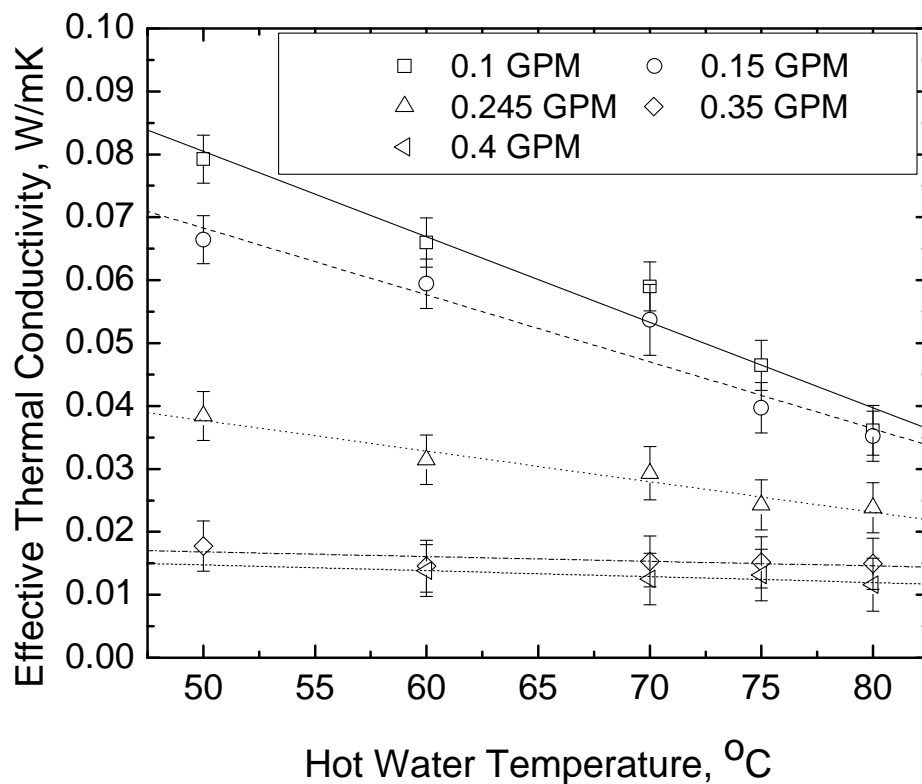
Figure 37 Effective thermal conductivity at each volume flux as a function of hot water temperature.
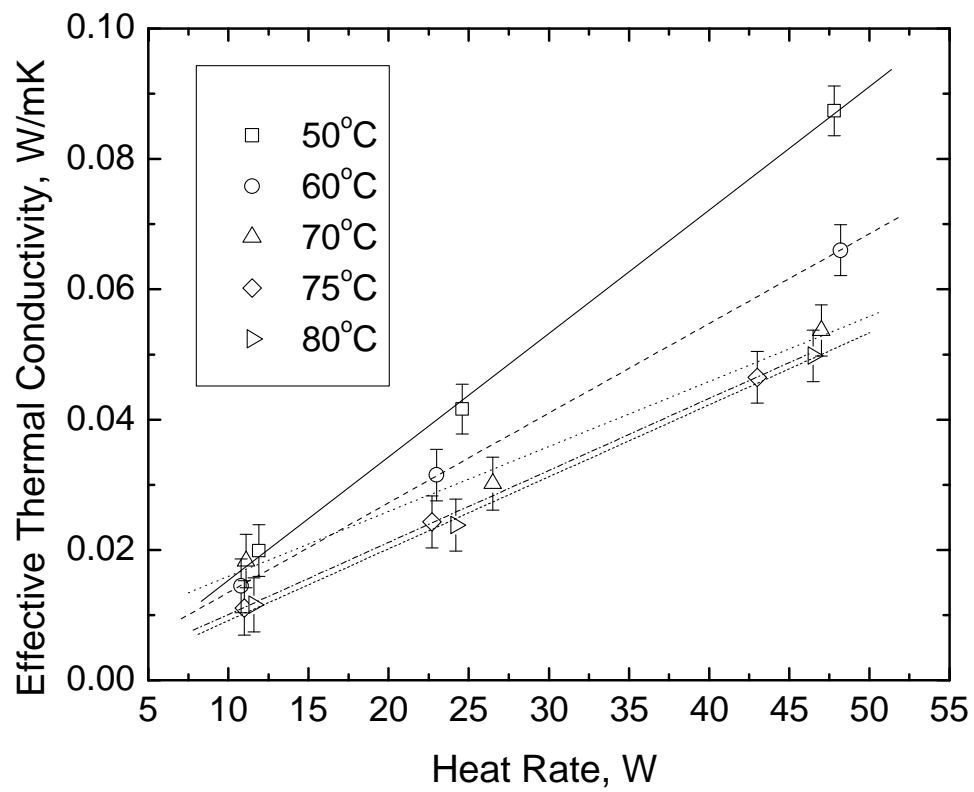
Figure 38 Effective thermal conductivity at each starting hot water temperature as a function of heat rate.
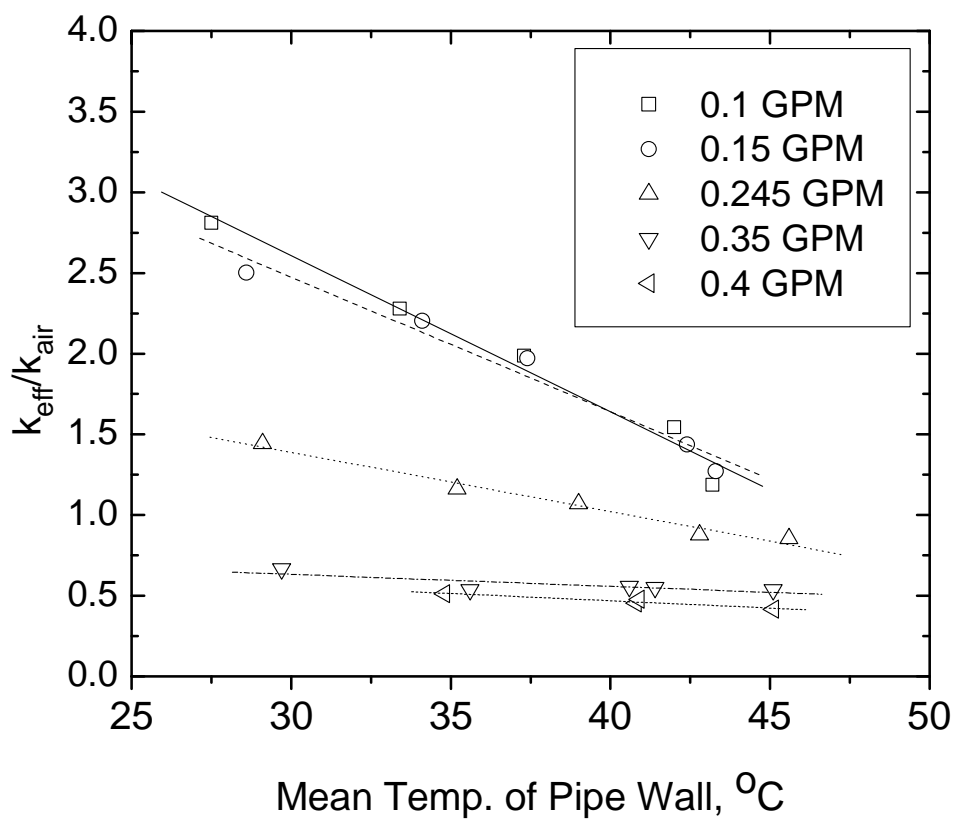
Figure 39 Ratio of thermal conductivity at each volume flux as a function of mean temperature of pipe wall.
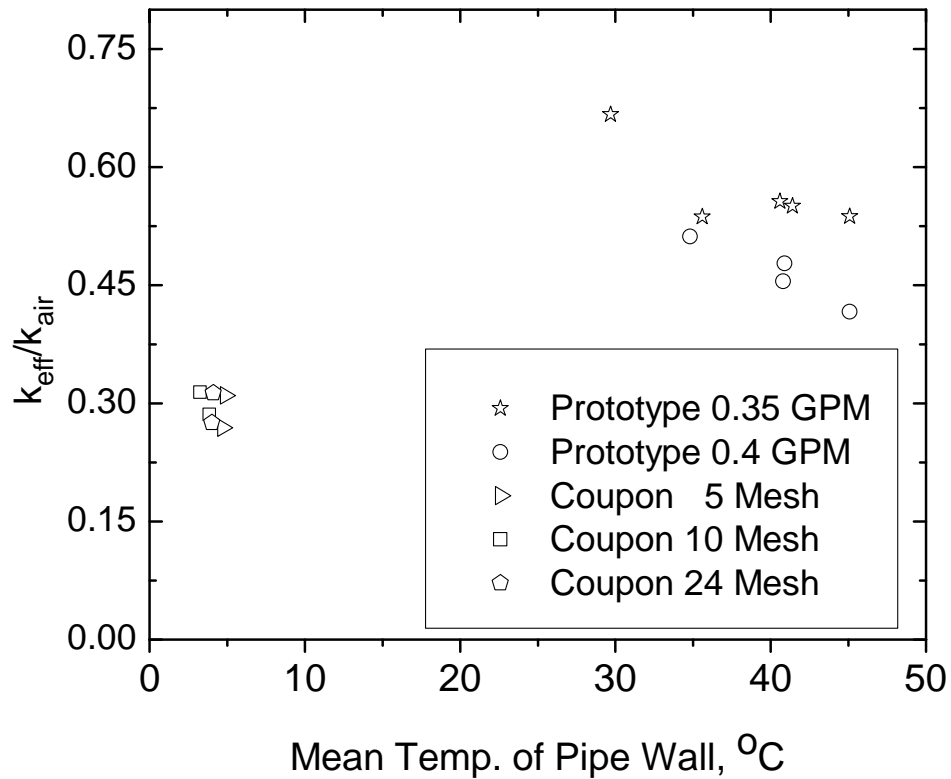
Figure 40 Ratios of thermal conductivity for prototype pipe and coupon tests as a function of mean temperature of pipe wall.

Table 6 Thermal conductivity of present technology to conventional materials [26, 27]

Material	IIT	Contra Therm™	C Therm™	Urethane	Air
Thermal Conductivity	0.017 ~ 0.079	0.151	0.08 ~ 0.15	0.026	0.0264
	At 27°C	Varies by water absorption	Varies by water absorption	At 27°C	At 27°C

Transient Test

For the transient tests, the thermal diffusivity was calculated from the surface temperature measurements as a function of mean temperature for the pipe wall. The thermal diffusivity, α, is compared to five different starting temperatures during the cool down period as shown in Fig. 41. At the higher mean temperatures, the thermal diffusivity difference between 50°C and 80°C was relatively large, however, as the mean temperature decreased, the difference decreased. For instance, at 27°C mean temperature the difference between 50°C and 80°C was $1.8\times10^{-6}\,m^2/s$ but at 4°C mean temperature, the difference decreased to $6.1\times10^{-9}\,m^2/s$, this difference is very small. For comparison purposes, the thermal diffusivity for this technology is shown with other conventional materials. Table 7 shows the comparison for these values.

The elapsed cooling times are shown in Fig. 42 for two (inner hot water temperatures of 50 and 80°C) cases. The cool down times were 16.6 and 18.1 hours, respectively, with similar cooling trends. For instance, when the starting temperature (the inner surface average temperature) was initially 72°C, the complete cool down period was 18.1 hours while at 47°C as the starting temperature it was 16.1 hours. However, the elapsed time difference was much smaller for the transient cool down period which started at 74°C and ended at 47°C, the measured time cycle was 1.4 hours. When the temperature trend for 47°C is shifted to approximately 74°C, the trends showed consistency.
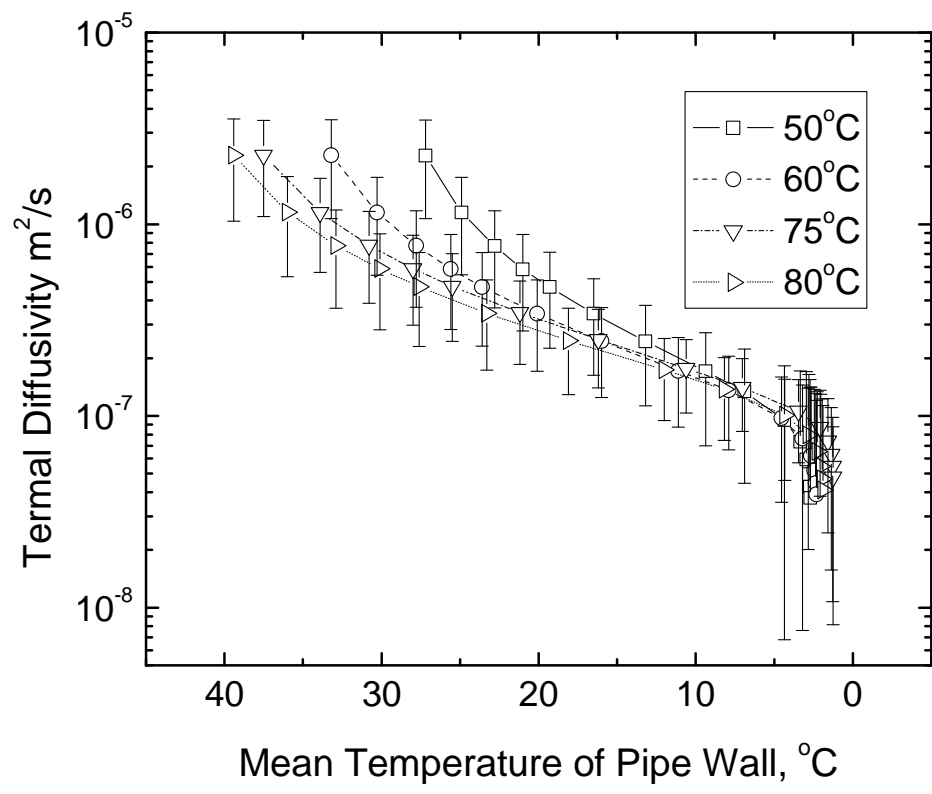
Figure 41 Thermal diffusivity variations at each starting hot water temperature as a function of mean pipe wall temperature.

Table 7 Thermal diffusivity of present technology to conventional materials [23, 25].

Material	IIT	Carbon Steel 1010	Stainless Steel 304	Glass Fiber	Air
Thermal Diffusivity At 27°C	4.721E-07 ~ 2.278E-06	1.88E-05	3.95E-06	1.42E-06	2.25E-05
Difference, %		825~3980	173~837	62.4~301	988~4765
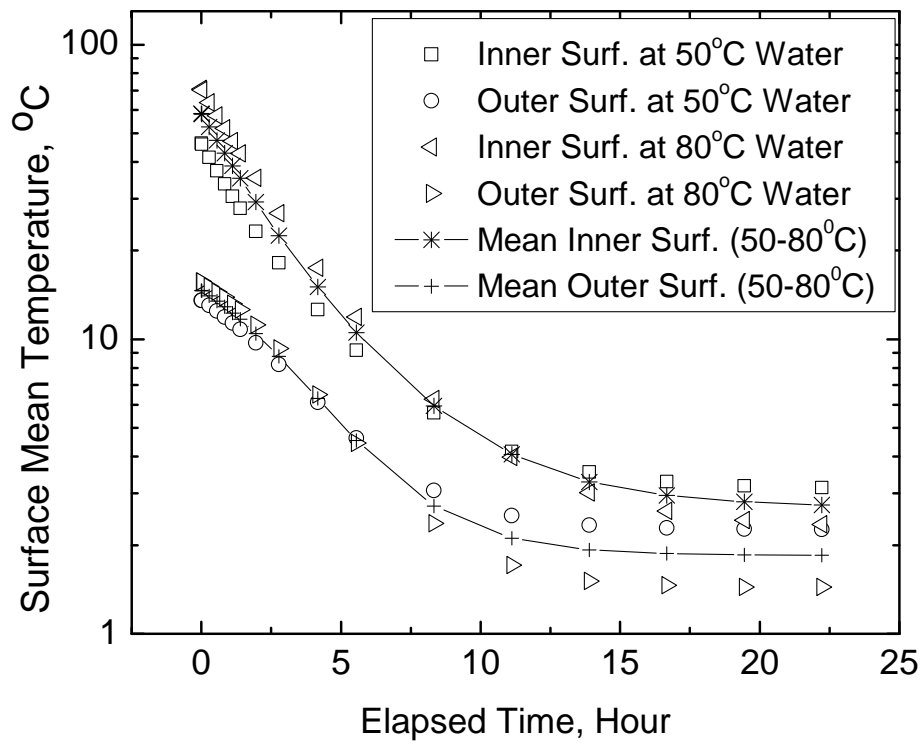
Figure 42 Mean temperature of inner and outer surface temperature of each contained water temperatures as a function of elapsed cooling time.

Figure 43 shows the ratio of the thermal diffusivities, α / α_{air}, for the IIT with respect to air as a function of mean temperature of pipe wall at each water temperature case. At low temperature (2.5°C), the IIT had a very low thermal diffusivity compare to air with a ratio values equal to 0.002, i.e. 0.2% of thermal diffusivity of air at same temperature. As the temperature was increased, the ratio for the thermal diffusivities increased up to 0.095 which represents 9.5% of the value for air. And as the temperature is increased further, the differences among the four different cases were observable but small enough to be within uncertainty range.

In summary, results from steady state and transient tests show the feasibility of the IIT. Visual investigation of the manufactured test pipe showed that the wire screen did not full come into contact with the pipe walls in every location. This may have affected the results for the effective thermal conductivity and the thermal diffusivity. However, as a prototype the pipe section was still very useful. For more realistic operating conditions, a full length pipe with more layers under more controlled manufacturing processes should be fabricated and evaluated for both thermal and mechanical performance.
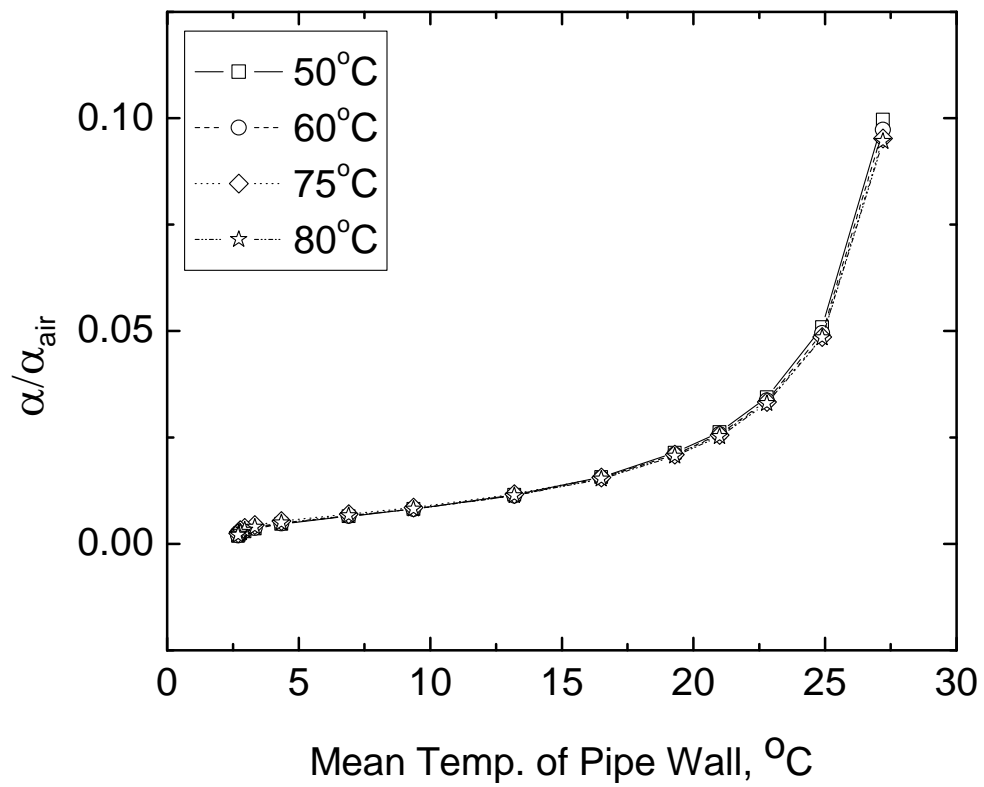
Figure 43 Thermal diffusivity ratios at each starting hot water temperature as a function of the mean pipe wall temperature.

CHAPTER V

FINDINGS

Analytical Model

1. The contact resistance decreases as applied interface pressure increases while the air resistance decreases only slightly. The model indicates that the thermal contact resistance is the dominant resistance in a node.

2. The contact resistances within a node can be divided into several contact resistances. The thermal contact resistance at the inner wall-to-wire interface, the wire-to-wire interface, and the wire-to-outer wall interface thermal resistance. The inner wall-to-wire or wire-to-outer wall contacts creates higher resistance than the wire-to-wire contact resistance. Therefore these contacts controlled the overall thermal resistance for the range of applied pressures investigated.

3. The dominant resistance component at the inner wall-to-wire interface was clearly the microcontact resistance, which is highly dependent on the applied interface pressure.

4. Even at the wire-to-wire interface, the microcontact resistance seemed to be the dominant resistance parameter; similar to the inner wall-to-wire interface.

5. As a comparison to model predictions, experimental data were shown with model predictions. The inclusion of a plastic model for micro contacts was

better at predicting the experimental data than the assumption of elastic micro contacts.

6. The average RMS errors were calculated for the various model predictions as compared to the experimentally measured values. Incorporating only the macrocontact model, an upper limit of 72% for the RMS error was calculated; while the inclusion of the plastic deformation model for microcontacts had an upper limit of 16%. The assumption of elastic microcontact deformation at the contacting interfaces had an upper limit of 26%.

7. The reason for the higher conductance/lower resistance at lighter pressures (light applied load) as compared to the model predictions can be accounted for from visual inspection of the wire screen prior to any testing. In the untested state, pre-deformation was observable at each wire-to-wire interface for each node. This can be attributed to stresses from the fabrication process. The applied load due to fabrication formed an initial contact area which results in lower resistance and higher conductance when compared to the model predictions.

8. To investigate the contribution of each resistance to the overall resistance in a single node, a radiative resistance further added to the model. As a result, higher thermal conductance (lower thermal resistance) was observed at lower pressure range. Under prediction at light pressure was decreased while at the high pressure its change was negligible, which is a positive result in the prediction of the thermal performance.

9. Thermal conductance for other wire mesh materials with different mesh numbers was predicted well by the analytical model for the given pressure range tested; however, under prediction was observed at low pressure. The RMS errors ranged from 10.5~21.9% .

10. A multilayer model which ranged from a single layer to fifty (50) layers was developed. As the number of layers increased, the thermal conductance of the structure decreased. Thermal conductance of a multilayer structure showed a significant decreased; however, the amount of decrease by adding each additional layer decreased as the number of layers increased.

11. For the multilayer structure, the thermal resistance, increased linearly as a function of applied interface pressure. The thermal resistance seemed more sensitive to applied pressure due to greater deformation of the structure; this resulted in greater contact area.

12. The effective thermal conductivity of the multilayer structure increased as the number of layer increased; however, its rate of increase decreased as the layers increased.

13. A sensitive study was conducted that included geometrical property and mechanical property such as surface roughness and Young's modulus. Moreover, thermophysical properties such as thermal conductivity and emissivity were included. When each parameter was varied by 10, 20 and 30% from nominal values (Table 5), thermal conductivity was observed to be the most dominant parameter.

Prototype Experiment

1. Under various experimental and steady state conditions, the effective thermal conductivity, k_{eff} , for various in-flow hot water temperatures and different volumetric flow rates (0.1 to 0.4 GPM) was computed. The results showed a very low value of 0.011 W/mK at 80°C; however, for the entire range of combinations, the value varied from 0.011 to 0.079 W/mK .

2. When the effect of heat rate on the effective thermal conductivity was analyzed, the lowest values observed ranged from 0.011 to 0.02 W/mK for a heat rate of 10W. These values occurred at inlet hot water temperatures between 50 to 80°C. It was observed that the effective thermal conductivity increased as the temperature and volumetric flow rate were decreased.

3. With four (4) different inlet hot water temperatures (50, 60, 70 and 80°C), transient tests were conducted so that the thermal diffusivity, α , and cooling times could be computed. At 27°C, the thermal diffusivity of IIT determined to be ranged $4.721 \times 10^{-7} \sim 2.278 \times 10^{-6} m^2/s$.

4. As the wall mean temperature was decreased, the thermal diffusivity decreased and among the various temperature cases the thermal diffusivity variance also decreased.

5. For comparison purposes, the thermal diffusivity values were compared with conventional insulation materials. The analysis showed a bare Carbon steel

ANSI 1010 had 825 ~ 3980% and a glass fiber insulation had 61 ~ 301% diffusivity values than IIT.

6. At an inlet hot water temperature of 80°C, the cooling time was 18.1 hours, and this value decreased to 16.6 hours as the initial hot water temperature was decreased to 50°C.

CHAPTER VI

CONCLUSIONS

In this study, an analytical and experimental study was conducted for an interstitial insulation technology (IIT). It included analytical modeling for performance predictions and the testing of a prototype pipe for measurement of actual thermal performance characteristics. By developing an analytical model for a multilayer screen wire structure its thermal conductance (resistance) was predicted for any given contact pressure for a one (1) inch diameter coupon.

Macro and micro contact resistance models were used to predict the thermal performance of an interstitial insulation technology which contained wire screen. The model developed showed very good agreement with the experimentally measured conductance, h, values over an applicable pressure range. We believe that this model can be used for an entire array of wire screen mesh sizes. This concept dramatically increased the thermal resistance when compared with a metallic slab (acting as a wall for pipe). As a result, the rate of heat loss from the inner hot wall to the outer cold wall was dramatically decreased by more than two orders of magnitude. These orders of magnitude will be higher when compared to higher thermal conductivity metals acting as the wall thickness of a pipe. The thermal conductance was further reduced by adding more layers of wire screen insulation.

In addition, the study modeled the influences of several contact resistance parameters which encompassed both macrocontacts and microcontacts at the interface

of contacting surfaces. Calculated average RMS errors were showed for the various model predictions as compared to the experimentally measured values. Incorporating only the macrocontact model gave higher RMS error, while the inclusion of the microcontact models gave lower errors. The assumption of plastic microcontact deformation at the interfaces gave the lowest error value; therefore, we conclude that plastic deformation is occurring at the contacting asperities.

Clearly, among the three deformation models, the inclusion of the plastic microcontacts with elastic macrocontact deformation showed very good results throughout the entire contact pressure range with especially excellent agreement at higher pressures. From the analytical model investigation, microcontact resistance was found to be the dominant resistance parameter.

A radiative resistance was added to the model as a parallel thermal resistance with the contact and air resistance. With the modified model, the contribution of the radiative resistance was investigated. As a result, the under prediction of thermal conductance (over prediction in thermal resistance) at light pressure range was reduced while at the high pressure its change was negligible, which is a positive result in the prediction of the thermal performance.

Thermal conductance predictions for different wire mesh materials and mesh number were compared against experimental data. The model predicted very well at the pressure range tested with results similar to Stainless Steel with respect to agreement.

A multilayer structure increases the number of layers from a single layer to the required number of layers, its performance characteristic was predicted with new multilayer model. Predictions indicate that as the number of layers increased, the thermal conductance of the structure decreased. However, the rate of reduction in conductance by adding each additional layer decreased as the number of layers increased. A linear increase in overall thermal resistance was observed with addition of layers. Thermal resistance seemed to be more sensitive to applied pressure. The effective thermal conductivity of the multilayer structure increased as the number of layer increased; however, its rate of increase decreased as the layers increased.

By conducting a parametric study with surface roughness, σ, as a geometrical property, Young's modulus, E, as a mechanical property and thermal conductivity, k, and emissivity, ε, as the thermophysical properties, it was observed that thermal conductivity was the dominant variable and each parameter's contribution to the thermal performance improvement (reduce thermal conductance) was identified as a function of applied interface pressure. Therefore, by modifying the geometrical, mechanical and thermophysical parameters of the wire screen an optimum design can be achieved.

Experimental tests using a prototype pipe with two layers of stainless wire mesh which were separated by a thin aluminum layer permitted preliminary measurement of the wire screen's thermal performance under simulated conditions. Under various combinations and steady state conditions, the effective thermal conductivity for in-flow

hot water temperatures at different volume flow rates (0.1 to 0.4 GPM) was calculated and its values were from 0.011 to 0.079 W/mK.

With seven different inlet hot water temperatures, transient tests were also conducted so that the thermal diffusivity and cooling times could be determined. The thermal diffusivity, α, was computed at different water temperatures. As the wall mean temperature was decreased, the thermal diffusivity decreased and among the various temperature cases the thermal diffusivity variance also decreased. For comparison purposes, the thermal diffusivity values were compared with conventional insulation materials. The analysis showed a 228% reduction as compared to bare Carbon steel ANSI 1010, and 80% reduction when compared to glass fiber insulation.

Using mean temperatures for the inner and outer walls, instead of inlet temperature, the results were similar. Therefore, it could be possible to predict cooling times for inlet hot water temperatures in the range between 50 to 80°C.

The results from both the modeling and experimental investigations seem to indicate superior insulating characteristics for the IIT when compared to current technologies, Thus, the present technology has shown promise for sub-sea piping and oil/gas applications and the viability of using a wire mesh as an insulating material has been proven in this investigation. However, to ensure the best performance optimization of the IIT is required and further study is needed to account for the over-prediction at lighter pressures as indicated by the analytical contact model. Pre-deformation of the contact area within the wire-to-wire interface was clearly observed. This could be attributed to wire tension forces from the fabrication process.

In summary, IIT (Interstitial Insulation Technology) is a strong candidate for reducing heat losses in many applications. Its advantages are higher structural strength, ease of installation, relatively low product cost and environmentally design due to non-chemical based material usage. Investigated results indicate superior insulating characteristics for the IIT when compared to current technologies. Thus, the present technology shows promise for most industrial applications besides insulating subsea piping.

REFERENCES

[1] Lou Watkins and Elmer Hershey, Cuming Corp. **May 2004** "Sub-sea Insulation." *World Pipelines*, pp. 49-54.

[2] Choqueuse, Dominique, Angele Chomard and Christian Bucherie. **2002** "Insulation Materials for Ultra Deep Sea Flow Assurance: Evaluation of the Material Properties." *OTC14115***,** pp. 1-8.

[3] Hallot, Raymond, Angele Chomard and Stephane Couprie. **2002** "Ils – A Passive Insulation Solution to Answer Cool Down Time Challenges on Deep Water Flowlines." *OTC 14117*, pp. 1-10.

[4] Azzola, J. H., Pattillo, P. D., Richey, J. F. and Segreto, S.J., **2004** "The Heat Transfer Characteristics of Vacuum Insulated Tubing." *SPE 90151*, pp. 1-8.

[5] Marotta, E. E. and Fletcher, L. S., **2005** "Interstitially Insulated Coaxial Pipe." *MMS/OTRC MEEN CHTL-05-509-35663*, pp. 2-3, 24-25.

[6] Yovanovich, M. M. and Marotta, E. E., 2003 *Thermal Spreading and Contact Resistances*, Heat Transfer Handbook, Wiley, New York, Chap.4.

[7] Cividino, S., Yovanovich, M. M. and Fletcher, L. S., **1974** "A Model for Predicting the Joint Conductance of a Woven Wire Screen Contacting Two Solids." *AIAA/ASME Thermophysics and Heat Transfer Conference, 74-695*, pp.1-17.

[8] Johnson, K. L., **1985** *Contact Mechanics*, Cambridge University Press, Cambridge.

[9] Lambert, M. A. and Fletcher, L. S., **1997** "Review of Models for Thermal Contact Conductance of Metals." *AIAA Journal of Thermophysics and Heat Transfer*, **11**, (2), pp. 129-140.

[10] Sridhar, M. R. and Yovanovich, M. M., **1994** "Review of Elastic and Plastic Contact Conductance Models Comparison with Experiment." *Journal of Thermophysics and Heat Transfer*, **8**, (4), pp. 633-640.

[11] Savija, I., Culham, J. R., Yovanovich, M. M. and Marotta, E. E., **2003** "Review of Thermal Conductance Models for Joints Incorporating Enhancement Materials." *Journal of Thermophysics and Heat transfer*, **17**, (1), pp. 43-52.

[12] Mills, A.F., **1999** *Heat Transfer*, 2nd ed., Prentice Hall, Upper Saddle River, New Jersey.

[13] Yovanovich, M. M., **1970** "Thermal Constriction Resistance Between Contacting Metallic Paraboloids: Application to Instrument Bearings." *AIAA Thermophysics Conference, 70-857*, pp.337-358.

[14] Cividino, S., **Dec. 1972** 'Thermal Constriction Resistance of Woven Screen Between Parallel Plates in a Vacuum." ME 751, Advanced Heat Conduction Project, Dept. of Mechanical Engineering, University of Waterloo, Waterloo, Ont.

[15] Rizzoni, G., **1993** *Principles and Applications of Electrical Engineering*, Irwin, Scarborough.

[16] Francis, H. A., **1975** "Application of Spherical Indentation Mechanics to Reversible and Irreversible Contact Between Rough Surfaces." *Wear*, **45,** pp. 221-269.

[17] Cooper, M. G., Mikic, B. B., and Yovanovich, M. M., **1969** "Thermal Contact Conductance." *Int. J. Heat Mass Transfer*, **12**, 279-300.

[18] Yovanovich, M. M., **1982** "Thermal Contact Correlations, in Progress in Astronautics and Aeronautics: Spacecraft Radiative Transfer and Temperature Control." *AIAA*, **83**, T. E. Horton, ed., AIAA, New York, pp. 83-95.

[19] Song, S., Yovanovich, M. M. and Nho, K., **1992** "Thermal Gap Conductance: Effects of Gas Pressure and Mechanical Load." *AIAA Journal of Thermophysics*, **6**, (1), pp.62-68.

[20] Mikic, B. B., **1974** "Thermal Contact Conductance: Theoretical Considerations." *Int. J. Heat Mass Transfer*, **17**, 205-214.

[21] Negus, K. J., and Yovanovich, M. M. **1988** "Correlation of Gap Conductance Integral for Conforming Rough Surfaces." *Journal of Thermophysics, Heat Transfer*, **12**, 279-281.

[22] Yovanovich, M. M., Culham, J. R. and Teertstra, P. **1997** "Calculating Interface Resistance." *Electronic Cooling*, **3**, pp. 1-7.

[23] Incropera, DeWitt, Bergman and Lavine, **2005** *Fundamentals of Heat and Mass Transfer*, Sixth Edition, Wiley, Hoboken, New Jersey.

[24] Raithby, G. D. and Hollands, K. G. T. **1975** "A General Method of Obtaining Approximate Solutions to Laminar and Turbulent Free Convection Problems." *Advanced in Heat Transfer* , **11**, Academic Press, New York, pp. 265-315.

[25] Schneider, P. J. **1955** *Conduction Heat Transfer*, Addison-Wesley, Reading, Massachusetts.

[26] Alderley, **2006** "ContraTherm®Subsea." www.alderleygroup.com/upload /Materials%20Subsea%202006.pdf.

[27] Cuming Corporation, **2004** "TB 601C-THERM Syntactic Foam Thermal Insulation." www.cumingcorp.com/insultn.php/pdf/tb_601.pdf.

APPENDIX A

EXPERIMENTAL DATA

Steady State Test

Effective Thermal Conductivity at Inflow hot water temperature and volume flux rate

	$50\,^{o}C$	$60\,^{o}C$	$70\,^{o}C$	$75\,^{o}C$	$80\,^{o}C$
0.1GPM	0.08406	0.065969	0.059016	0.046464	0.036143
0.15GPM	0.066428	0.059459	0.053689	0.039723	0.035211
0.245GPM	0.038436	0.03146	0.029328	0.024278	0.023846
0.35GPM	0.01776	0.014544	0.015296	0.015161	0.01495
0.4GPM		0.013841	0.012507	0.013142	0.011588

Effective Thermal Conductivity at Inflow hot water temperature and Heat rate

Heat Rate(W)	4.78E+01	2.46E+01	1.19E+01
$50\,^{o}C$	0.087371	0.041577	0.019901
Heat Rate(W)	4.82E+01	2.30E+01	1.11E+01
$60\,^{o}C$	0.065969	0.031461	0.014544
Heat Rate(W)	4.69E+01	2.65E+01	1.10E+01
$70\,^{o}C$	0.053689	0.030153	0.012475
Heat Rate(W)	4.30E+01	2.27E+01	1.10E+01
$75\,^{o}C$	0.046464	0.024278	0.011086
Heat Rate(W)	4.64E+01	2.42E+01	1.15 E+01
$80\,^{o}C$	0.050157	0.023846	0.011588

Transient Test

Thermal Diffusivity at given elapsed cooling time and mean surface temperature for initially contained Hot water

60^oC	α	65^oC	α	73^oC	α
33.17	2.288E-06	32.94	2.269E-06	37.46	2.286E-06
30.34	1.151E-06	29.94	1.143E-06	33.92	1.153E-06
27.83	7.729E-07	27.26	7.688E-07	30.79	7.756E-07
25.58	5.84E-07	24.86	5.819E-07	27.99	5.873E-07
23.57	4.708E-07	22.70	4.701E-07	25.48	4.745E-07
20.09	3.42E-07	18.97	3.429E-07	21.21	3.460E-07
15.95	2.46E-07	14.55	2.487E-07	16.23	2.505E-07
11.07	1.722E-07	9.45	1.770E-07	10.56	1.773E-07
7.89	1.356E-07	6.27	1.420E-07	7.03	1.414E-07
4.54	9.768E-08	3.16	1.065E-07	3.46	1.059E-07
3.20	7.629E-08	2.03	8.572E-08	2.09	8.714E-08
2.66	6.198E-08	1.61	7.054E-08	1.57	7.379E-08
2.44	5.191E-08	1.46	5.929E-08	1.36	6.313E-08
2.35	4.457E-08	1.40	5.093E-08	1.29	5.464E-08
2.32	3.901E-08	1.38	4.459E-08	1.25	4.797E-08

75^oC	α	78^oC	α	80^oC	α
37.74	2.285E-06	39.85	2.299E-06	39.41	2.293E-06
34.17	1.153E-06	36.23	1.158E-06	36.00	1.154E-06
30.98	7.756E-07	33.01	7.782E-07	32.93	7.749E-07
28.14	5.874E-07	30.14	5.886E-07	30.15	5.855E-07
25.58	4.748E-07	27.56	4.750E-07	27.63	4.721E-07
21.21	3.466E-07	23.14	3.457E-07	23.26	3.431E-07
16.10	2.515E-07	17.95	2.494E-07	18.06	2.472E-07
10.30	1.79E-07	11.96	1.755E-07	12.00	1.739E-07
6.74	1.437E-07	8.18	1.389E-07	8.18	1.379E-07
3.24	1.088E-07	4.33	1.012E-07	4.32	1.009E-07
1.95	8.992E-08	2.85	7.992E-08	2.84	7.974E-08
1.46	7.591E-08	2.28	6.530E-08	2.26	6.510E-08
1.28	6.462E-08	2.06	5.481E-08	2.03	5.459E-08
1.21	5.576E-08	1.98	4.708E-08	1.94	4.688E-08
1.18	4.889E-08	1.94	4.123E-08	1.89	4.104E-08

Inner and outer Surface Temperature at given elapsed cooling time for three different

contained hot water temperatures.

Cooling Time (Sec.)	$50\,^{o}C$		$80\,^{o}C$	
	Inner(^{o}C)	Outer(^{o}C)	Inner(^{o}C)	Outer(^{o}C)
0.0001	46.29	13.57	70.69	15.71
60	45.98	13.54	70.25	15.67
1000	41.44	13.03	63.70	15.12
2000	37.27	12.47	57.49	14.51
3000	33.67	11.92	51.98	13.88
4000	30.55	11.36	47.06	13.23
5000	27.81	10.81	42.68	12.57
7000	23.27	9.72	35.27	11.25
10000	18.19	8.21	26.81	9.30
15000	12.61	6.11	17.51	6.49
20000	9.18	4.62	11.90	4.45
30000	5.63	3.06	6.26	2.37
40000	4.15	2.52	3.98	1.71
50000	3.54	2.34	3.02	1.51
60000	3.28	2.28	2.61	1.46
70000	3.18	2.27	2.43	1.44
80000	3.13	2.26	2.35	1.44

APPENDIX B

UNCERTAINTY ANALYSIS

Steady State Test

Uncertainty in inner surface Area

$$A_{is} = \pi D_i L$$

$$\Delta D_i = 0.00005\text{m}, \ \Delta L = 0.0005\text{m}$$

$$\frac{dA_{is}}{dD_i} \cdot \Delta D_i = \pi L \cdot \Delta D_i$$

(A. 1)

$$\frac{dA_{is}}{dL} \cdot \Delta L = \pi D_i \cdot \Delta L$$

(A. 2)

$$\omega_A = \sqrt{\left(\frac{dA_{is}}{dD_i} \cdot \Delta D_i\right)^2 + \left(\frac{dA_{is}}{dL} \cdot \Delta L\right)^2}$$

(A. 3)

Uncertainty in the heat transfer coefficient

$$h_i = \frac{4.36 k_w}{D_i}$$

$$\Delta k_w = 0.001 \ \text{W/m-K}$$

$$\frac{dh_i}{dk_w} \cdot \Delta k_w = \frac{4.36}{D_i} \cdot \Delta k_w$$

(A. 4)

$$\frac{dh_i}{dD_i} \cdot \Delta D_i = -\frac{4.36 k_w}{D_i^{\ 2}} \cdot \Delta D_i$$

(A. 5)

$$\omega_{h_i} = \sqrt{\left(\frac{dh_i}{dk_w} \cdot \Delta k_w\right)^2 + \left(\frac{dh_i}{dD_i} \cdot \Delta D_i\right)^2}$$

(A. 6)

Uncertainty in heat rate

$$\dot{Q} = h_i A_{is} (T_i - T_o)$$

$$\Delta T = 0.0018\,^o C$$

$$\frac{d\dot{Q}}{dh_i} \cdot \Delta h = A_{is} (T_i - T_o) \cdot \Delta h_i$$

(A. 7)

$$\frac{d\dot{Q}}{dA_{is}} \cdot \Delta A_{is} = h_i (T_i - T_o) \cdot \Delta A_{is}$$

(A. 8)

$$\frac{d\dot{Q}}{dT_i} \cdot \Delta T_i = h_i A_{is} \cdot \Delta T_i$$

(A. 9)

$$\frac{d\dot{Q}}{dT_o} \cdot \Delta T_o = -h_i A_{is} \cdot \Delta T_o$$

(A. 10)

$$\omega_{\dot{Q}} = \sqrt{\left(\frac{d\dot{Q}}{dh_i} \cdot \Delta h\right)^2 + \left(\frac{d\dot{Q}}{dA_{is}} \cdot \Delta A_{is}\right)^2 + \left(\frac{d\dot{Q}}{dT_i} \cdot \Delta T_i\right)^2 + \left(\frac{d\dot{Q}}{dT_o} \cdot \Delta T_o\right)^2}$$

(A. 11)

Uncertainty in the effective thermal conductivity

$$k_{eff} = \frac{\dot{Q}t}{A_{is}(T_i - T_o)}$$

$$\Delta t = 0.0001\mathrm{m}, \ t = 0.0127\mathrm{m}$$

$$\frac{dk_{eff}}{d\dot{Q}} \cdot \Delta\dot{Q} = \frac{t}{A_{is}(T_i - T_o)} \cdot \Delta\dot{Q}$$

(A. 12)

$$\frac{dk_{eff}}{dt} \cdot \Delta t = \frac{\dot{Q}}{A_{is}(T_i - T_o)} \cdot \Delta t$$

(A. 13)

$$\frac{dk_{eff}}{dA_{is}} \cdot \Delta A_{is} = -\frac{\dot{Q}t}{A_{is}^2(T_i - T_o)} \cdot \Delta A_{is}$$

(A. 14)

$$\frac{dk_{eff}}{dT_i} \cdot \Delta T_i = -\frac{\dot{Q}t}{A_{is}(T_i - T_o)^2} \cdot \Delta T_i$$

(A. 15)

$$\frac{dk_{eff}}{dT_o} \cdot \Delta T_o = \frac{\dot{Q}t}{A_{is}(T_i - T_o)^2} \cdot \Delta T_o$$

(A. 16)

$$\omega_{k_{eff}} = \sqrt{\left(\frac{dk_{eff}}{d\dot{Q}} \cdot \Delta\dot{Q}\right)^2 + \left(\frac{dk_{eff}}{dt} \cdot \Delta t\right)^2 + \left(\frac{dk_{eff}}{dA_{is}} \cdot \Delta A_{is}\right)^2 + \left(\frac{dk_{eff}}{dT_i} \cdot \Delta T_i\right)^2 + \left(\frac{dk_{eff}}{dT_o} \cdot \Delta T_o\right)^2}$$

(A. 17)

Inflow $50\,^{o}C$ hot water

	A.1	A.2			A.3
	1.46E-04	1.20E-04			1.89E-04
	A.4	A.5			A.6
	5.72E-02	-2.44E-02			6.22E-02
Inflow rate (GPM)	A.7	A.8	A.9	A.10	A.11
1.00E-01	8.05E-02	4.08E-02	1.44E-02	-1.44E-02	9.25E-02
1.50E-01	6.61E-02	3.35E-02	1.44E-02	-1.44E-02	7.69E-02
2.45E-01	5.10E-02	1.45E-02	1.44E-02	-1.44E-02	6.47E-02
3.50E-01	1.82E-02	9.25E-03	1.44E-02	-1.44E-02	2.89E-02
Heat Rate (W)	A.7	A.8	A.9	A.10	A.11
4.78E+01	8.12E-02	5.38E-02	1.44E-02	-1.44E-02	9.95E-02
2.46E+01	4.18E-02	2.12E-02	1.44E-02	-1.44E-02	5.11E-02
1.19E+01	2.02E-02	1.02E-02	1.44E-02	-1.44E-02	3.05E-02

Inflow rate (GPM)	A.12	A.13	A.14	A.15	A.16	A.17($\omega_{k_{eff}}$)	$k_{eff}(W/m^2K)$	% Difference
1.00E-01	9.08E-04	3.66E-03	-4.01E-04	-1.42E-04	1.42E-04	3.80E-03	7.93E-02	4.79E+00
1.50E-01	9.19E-04	3.66E-03	-4.01E-04	-1.73E-04	1.73E-04	3.80E-03	6.64E-02	5.73E+00
2.45E-01	9.25E-04	3.66E-03	-4.01E-04	-3.32E-04	3.32E-04	3.88E-03	3.84E-02	1.01E+01
3.50E-01	1.25E-03	3.66E-03	-4.01E-04	-6.25E-04	6.25E-04	3.99E-03	1.78E-02	2.25E+01
Heat Rate (W)	A.12	A.13	A.14	A.15	A.16	A.17($\omega_{k_{eff}}$)	$k_{eff}(W/m^2K)$	% Difference
4.78E+01	9.68E-04	3.66E-03	-4.01E-04	-1.40E-04	1.40E-04	3.81E-03	8.74E-02	4.37E+00
2.46E+01	9.66E-04	3.66E-03	-4.01E-04	-2.73E-04	2.73E-04	3.83E-03	4.16E-02	9.21E+00
1.19E+01	1.19E-03	3.66E-03	-4.01E-04	-5.65E-04	5.65E-04	3.95E-03	1.99E-02	1.99E+01

Inflow $80\,^{o}C$ hot water

	A.1	A.2		A.3
	1.46E-04	1.20E-04		1.89E-04
	A.4	A.5		A.6
	5.72E-02	-2.55E-02		6.26E-02
Inflow rate (GPM)	A.7	A.8	A.9	A.10	A.11
1.00E-01	5.68E-02	2.99E-02	1.51E-02	-1.51E-02	6.76E-02
1.50E-01	5.48E-02	2.88E-02	1.51E-02	-1.51E-02	6.55E-02
2.45E-01	3.97E-02	2.09E-02	1.51E-02	-1.51E-02	4.96E-02
3.50E-01	2.44E-02	1.28E-02	1.51E-02	-1.51E-02	3.48E-02
4.00E-01	1.89E-02	9.96E-03	1.51E-02	-1.51E-02	3.02E-02
Heat rate (W)	A.7	A.8	A.9	A.10	A.11
4.30E+01	7.62E-02	4.01E-02	1.51E-02	-1.51E-02	8.87E-02
2.27E+01	3.97E-02	2.09E-02	1.51E-02	-1.51E-02	4.96E-02
1.10E+01	1.89E-02	9.96E-03	1.51E-02	-1.51E-02	3.02E-02

Inflow rate (GPM)	A.12	A.13	A.14	A.15	A.16	A.17($\omega_{k_{eff}}$)	$k_{eff}(W/m^2K)$	% Difference
1.00E-01	9.47E-04	3.82E-03	-4.19E-04	-2.11E-04	2.11E-04	3.97E-03	3.61E-02	1.10E+01
1.50E-01	9.50E-04	3.82E-03	-4.19E-04	-2.19E-04	2.19E-04	3.97E-03	3.52E-02	1.13E+01
2.45E-01	9.95E-04	3.82E-03	-4.19E-04	-3.02E-04	3.02E-04	3.99E-03	2.38E-02	1.68E+01
3.50E-01	1.14E-03	3.82E-03	-4.19E-04	-4.91E-04	4.91E-04	4.07E-03	1.50E-02	2.72E+01
4.00E-01	1.27E-03	3.82E-03	-4.19E-04	-8.16E-04	8.16E-04	4.21E-03	1.16E-02	3.63E+01
Heat rate (W)	A.12	A.13	A.14	A.15	A.16	A.17($\omega_{k_{eff}}$)	$k_{eff}(W/m^2K)$	% Difference
4.30E+01	9.26E-04	3.82E-03	-4.19E-04	-1.57E-04	1.57E-04	3.96E-03	4.98E-02	7.95E+00
2.27E+01	9.95E-04	3.82E-03	-4.19E-04	-3.02E-04	3.02E-04	3.99E-03	2.38E-02	1.68E+01
1.10E+01	1.27E-03	3.82E-03	-4.19E-04	-6.33E-04	6.33E-04	4.15E-03	1.16E-02	3.58E+01

Transient Test

Uncertainty in Rayleigh Number

$$Ra_L = \frac{g\,\beta(T_{os} - T_{ss})t^3}{\nu\alpha_c}$$

$\Delta g = 0.001\,m/s^2$, $\Delta\beta = 0.00001\,K^{-1}$, $\Delta T_{os} = 0.5^{\,o}C$, $\Delta T_{ss} = 0.05^{\,o}C$

$\Delta t = 0.002\text{m}$, $\Delta\nu = 0.1\,m^2/s$, $\Delta\alpha_c = 10^{-10}\,m^2/s$

$$\frac{dRa_L}{dg}\cdot\Delta g = \frac{\beta(T_{os} - T_{ss})t^3}{\nu\alpha_c}\cdot\Delta g$$

(A. 18)

$$\frac{dRa_L}{d\beta}\cdot\Delta\beta = \frac{g(T_{os} - T_{ss})t^3}{\nu\alpha_c}\cdot\Delta\beta$$

(A. 19)

$$\frac{dRa_L}{d\beta}\cdot\Delta T_{os} = \frac{g\,\beta t^3}{\nu\alpha_c}\cdot\Delta T_{os}$$

(A. 20)

$$\frac{dRa_L}{d\beta}\cdot\Delta T_{ss} = -\frac{g\,\beta t^3}{\nu\alpha_c}\cdot\Delta T_{ss}$$

(A. 21)

$$\frac{dRa_L}{d\beta}\cdot\Delta t = \frac{3g(T_{os} - T_{ss})t^2}{\nu\alpha_c}\cdot\Delta t$$

(A. 22)

$$\frac{dRa_L}{d\nu} \cdot \Delta\nu = -\frac{g\beta(T_{os} - T_{ss})t^3}{\nu^2\alpha_c} \cdot \Delta\nu$$

(A. 23)

$$\frac{dRa_L}{d\alpha_c} \cdot \Delta\alpha_c = -\frac{g\beta(T_{os} - T_{ss})t^3}{\nu\alpha_c^2} \cdot \Delta\alpha_c$$

(A. 24)

$$\omega_{Ra_L} = \sqrt{\left(\frac{dRa_L}{dg}\cdot\Delta g\right)^2 + \left(\frac{dRa_L}{d\beta}\cdot\Delta\beta\right)^2 + \left(\frac{dRa_L}{d\beta}\cdot\Delta T_{os}\right)^2 + \left(\frac{dRa_L}{d\beta}\cdot\Delta T_{ss}\right)^2 + \left(\frac{dRa_L}{d\beta}\cdot\Delta t\right)^2 + \left(\frac{dRa_L}{d\nu}\cdot\Delta\nu\right)^2 + \left(\frac{dRa_L}{d\alpha_c}\cdot\Delta\alpha_c\right)^2}$$

(A. 25)

Uncertainty in Concentric Cylinder Rayleigh Number

$$Ra_c^* = \frac{\left[\ln\left(D_s/D_o\right)\right]^4 Ra_L}{t^3\left(D_s^{-3/5} + D_o^{-3/5}\right)^5}$$

$$\Delta D_s = 0.0000508\text{m}$$

$$\Delta D_o = 0.0004\text{m}$$

$$\frac{dRa_c^*}{dD_s} \cdot \Delta D_s = \left\{\frac{3D_o^{18/5}D_s^2\left[\ln\left(D_s/D_o\right)\right]^4 Ra_L}{\left(D_s^{3/5} + D_o^{3/5}\right)^6 t^3} + \frac{4D_o^3 D_s^2\left[\ln\left(D_s/D_o\right)\right]^3 Ra_L}{\left(D_s^{3/5} + D_o^{3/5}\right)^5 t^3}\right\} \cdot \Delta D_s$$

(A. 26)

$$\frac{dRa_c^*}{dD_o} \cdot \Delta D_o = \frac{-\left[\ln\left(D_s/D_o\right)\right]^3 \cdot D_o^2 \cdot \left\{4\cdot D_o^{3/5} - \left[3\cdot\ln\left(D_s/D_o\right) - 4\right]\cdot D_s^{3/5}\right\}\cdot D_s^3 \cdot Ra_L}{\left(D_s^{3/5} + D_o^{3/5}\right)^6 t^3} \cdot \Delta D_o$$

(A. 27)

$$\frac{dRa_c^*}{dRa_L} \cdot \Delta Ra_L = \frac{\left[\ln\left(D_s / D_o\right)\right]^4}{t^3 \left(D_s^{-3/5} + D_o^{-3/5}\right)^5} \cdot \Delta Ra_L$$

(A. 28)

$$\frac{dRa_c^*}{dRa_L} \cdot \Delta t = -\frac{3\left[\ln\left(D_s / D_o\right)\right]^4 Ra_L}{t^4 \left(D_s^{-3/5} + D_o^{-3/5}\right)^5} \cdot \Delta t$$

(A. 29)

$$\omega_{Ra_c^*} = \sqrt{\left(\frac{dRa_c^*}{dD_s} \cdot \Delta D_s\right)^2 + \left(\frac{dRa_c^*}{dD_o} \cdot \Delta D_o\right)^2 + \left(\frac{dRa_c^*}{dRa_L} \cdot \Delta Ra_L\right)^2 + \left(\frac{dRa_c^*}{dRa_L} \cdot \Delta t\right)^2}$$

(A. 30)

Uncertainty in Effective thermal conductivity in Concentric Rayleigh Number

$$k_{ef} = 0.386 k_c \left(\frac{\Pr}{0.861 + \Pr}\right)^{1/4} \left(Ra_c^*\right)^{1/4}$$

$$\Delta k_c = 0.1 \, W/m^2 K$$

$$\Delta \Pr = 0.1$$

$$\frac{dk_{ef}}{dk_c} \cdot \Delta k_c = 0.386 \left(\frac{\Pr}{0.861 + \Pr}\right)^{1/4} \left(Ra_c^*\right)^{1/4} \cdot \Delta k_c$$

(A. 31)

$$\frac{dk_{ef}}{d\Pr} \cdot \Delta \Pr = \frac{0.083087 k_c \left(Ra_c^*\right)^{1/4}}{\left(\Pr + 0.861\right)^2 \cdot \left(\frac{\Pr}{0.861 + \Pr}\right)^{3/4}} \cdot \Delta \Pr$$

(A. 32)

$$\frac{dk_{ef}}{dRa_c^*} \cdot \Delta Ra_c^* = 0.386 k_c \left(\frac{Pr}{0.861 + Pr}\right)^{1/4} \cdot \frac{\left(Ra_c^*\right)^{-3/4}}{4} \cdot \Delta Ra_c^*$$

(A. 33)

$$\omega_{k_{ef}} = \sqrt{\left(\frac{dk_{ef}}{dk_c} \cdot \Delta k_c\right)^2 + \left(\frac{dk_{ef}}{d Pr} \cdot \Delta Pr\right)^2 + \left(\frac{dk_{ef}}{dRa_c^*} \cdot \Delta Ra_c^*\right)^2}$$

(A. 34)

Uncertainty in Heat rate

$$\dot{Q} = \frac{2\pi k_{ef} L}{\ln(D_s / D_o)} (T_{os} - T_{ss})$$

$$\Delta L = 0.001 \text{m}$$

$$\frac{d\dot{Q}}{dk_{ef}} \cdot \Delta k_{ef} = \frac{2\pi L}{\ln(D_s / D_o)} (T_{os} - T_{ss}) \cdot \Delta k_{ef}$$

(A. 35)

$$\frac{d\dot{Q}}{dL} \cdot \Delta L = \frac{2\pi k_{ef}}{\ln(D_s / D_o)} (T_{os} - T_{ss}) \cdot \Delta L$$

(A. 36)

$$\frac{d\dot{Q}}{dT_{os}} \cdot \Delta T_{os} = \frac{2\pi k_{ef} L}{\ln(D_s / D_o)} \cdot \Delta T_{os}$$

(A. 37)

$$\frac{d\dot{Q}}{dT_{ss}} \cdot \Delta T_{ss} = \frac{-2\pi k_{ef} L}{\ln(D_s / D_o)} \cdot \Delta T_{ss}$$

(A. 38)

$$\frac{d\dot{Q}}{dD_s} \cdot \Delta D_s = \frac{-2\pi k_{ef} L}{\left[\ln(D_s / D_o)\right]^2 D_s} (T_{os} - T_{ss}) \cdot \Delta D_s$$

(A. 39)

$$\frac{d\dot{Q}}{dD_o} \cdot \Delta D_o = \frac{2\pi k_{ef} L}{\left[\ln(D_s / D_o)\right]^2 D_o} (T_{os} - T_{ss}) \cdot \Delta D_o$$

(A. 40)

$$\omega_{\dot{Q}} = \sqrt{\left(\frac{d\dot{Q}}{dk_{ef}} \cdot \Delta k_{ef}\right)^2 + \left(\frac{d\dot{Q}}{dL} \cdot \Delta L\right)^2 + \left(\frac{d\dot{Q}}{dT_{os}} \cdot \Delta T_{os}\right)^2 + \left(\frac{d\dot{Q}}{dT_{ss}} \cdot \Delta T_{ss}\right)^2 + \left(\frac{d\dot{Q}}{dD_s} \cdot \Delta D_s\right)^2 + \left(\frac{d\dot{Q}}{dD_o} \cdot \Delta D_o\right)^2}$$

(A. 41)

Uncertainty in Free Convection heat transfer coefficient

$$h_o = \frac{\dot{Q}}{A_{os}(T_{os} - T_{ss})}$$

$$\Delta A_{os} = 0.00049163 \, m^2$$

$$\frac{dh_o}{d\dot{Q}} \cdot \Delta \dot{Q} = \frac{1}{A_{os}(T_{os} - T_{ss})} \cdot \Delta \dot{Q}$$

(A. 42)

$$\frac{dh_o}{dA_{os}} \cdot \Delta A_{os} = -\frac{\dot{Q}}{A_{os}^{\;2}(T_{os} - T_{ss})} \cdot \Delta A_{os}$$

(A. 43)

$$\frac{dh_o}{dT_{os}} \cdot \Delta T_{os} = -\frac{\dot{Q}}{A_{os}(T_{os} - T_{ss})^2} \cdot \Delta T_{os}$$

(A. 44)

$$\frac{dh_o}{dT_{ss}} \cdot \Delta T_{ss} = \frac{\dot{Q}}{A_{os}\left(T_{os} - T_{ss}\right)^2} \cdot \Delta T_{ss}$$

(A. 45)

$$\omega_{h_o} = \sqrt{\left(\frac{dh_o}{d\dot{Q}} \cdot \Delta \dot{Q}\right)^2 + \left(\frac{dh_o}{dA_{os}} \cdot \Delta A_{os}\right)^2 + \left(\frac{dh_o}{dT_{os}} \cdot \Delta T_{os}\right)^2 + \left(\frac{dh_o}{dT_{ss}} \cdot \Delta T_{ss}\right)^2}$$

(A. 46)

Uncertainty in Biot Number

$$Bi = \frac{h_o t}{k}$$

$$\Delta k = 0.5 \, W/m^2 K$$

$$\frac{dBi}{dh_o} \cdot \Delta h_o = \frac{t}{k} \cdot \Delta h_o$$

(A. 47)

$$\frac{dBi}{dt} \cdot \Delta t = \frac{h_o}{k} \cdot \Delta t$$

(A. 48)

$$\frac{dBi}{dk} \cdot \Delta k = -\frac{h_o t}{k^2} \cdot \Delta k$$

(A. 49)

$$\omega_{h_o} = \sqrt{\left(\frac{dBi}{dh_o}\cdot\Delta h_o\right)^2 + \left(\frac{dBi}{dt}\cdot\Delta t\right)^2 + \left(\frac{dBi}{dk}\cdot\Delta k\right)^2}$$

(A. 50)

Uncertainty in Dimensionless Radius

$$r^* = r/r_o$$

$$\Delta r = 0.00005\text{m}$$

$$\Delta r_o = 0.00005\text{m}$$

$$\frac{dr^*}{dr}\cdot\Delta r = \frac{1}{r_o}\cdot\Delta r$$

(A. 51)

$$\frac{dr^*}{dr_o}\cdot\Delta r_o = -\frac{r}{r_o^2}\cdot\Delta r_o$$

(A. 52)

$$\omega_{r^*} = \sqrt{\left(\frac{dr^*}{dr}\cdot\Delta r\right)^2 + \left(\frac{dr^*}{dr_o}\cdot\Delta r_o\right)^2}$$

(A. 53)

Uncertainty in Coefficient

$$C_1 = \frac{2}{\zeta_1}\frac{J_1(\zeta_1)}{J_0^{\,2}(\zeta_1)+J_1^{\,2}(\zeta_1)}$$

$$\frac{dC_1}{d\zeta_1}\cdot\Delta\zeta_1 = \left\{-\frac{2}{\zeta_1^2}\frac{J_1(\zeta_1)}{J_0^{\,2}(\zeta_1)+J_1^{\,2}(\zeta_1)} + \frac{2}{\zeta_1}\left\{\frac{-J_2(\zeta_1)}{J_0^{\,2}(\zeta_1)+J_1^{\,2}(\zeta_1)} - \frac{J_1(\zeta_1)\cdot[2J_0(\zeta_1)+2J_1(\zeta_1)]}{\left[J_0^{\,2}(\zeta_1)+J_1^{\,2}(\zeta_1)\right]^2}\right\}\right\}\cdot\Delta\zeta_1$$

(A. 54)

$$\omega_{C_1} = \sqrt{\left(\frac{dC_1}{d\zeta_1} \cdot \Delta\zeta_1\right)^2}$$

(A. 55)

Uncertainty in Dimensionless Temperature

$$\theta^* = \frac{T_{os} - T_{ss}}{T_{osi} - T_{ss}}$$

$$\Delta T_{osi} = 0.05\,^o C$$

$$\frac{d\theta^*}{dT_{os}} \cdot \Delta T_{os} = \frac{1}{T_{osi} - T_{ss}} \cdot \Delta T_{os}$$

(A. 56)

$$\frac{d\theta^*}{dT_{ss}} \cdot \Delta T_{ss} = \left[\frac{-1}{T_{osi} - T_{ss}} + \frac{T_{os} - T_{ss}}{\left(T_{osi} - T_{ss}\right)^2}\right] \cdot \Delta T_{ss}$$

(A. 57)

$$\frac{d\theta^*}{dT_{osi}} \cdot \Delta T_{osi} = \frac{-\left(T_{os} - T_{ss}\right)}{\left(T_{osi} - T_{ss}\right)^2} \cdot \Delta T_{osi}$$

(A. 58)

$$\omega_{\theta^*} = \sqrt{\left(\frac{d\theta^*}{dT_{os}} \cdot \Delta T_{os}\right)^2 + \left(\frac{d\theta^*}{dT_{ss}} \cdot \Delta T_{ss}\right)^2 + \left(\frac{d\theta^*}{dT_{osi}} \cdot \Delta T_{osi}\right)^2}$$

(A. 59)

Uncertainty in Fourier Number

$$Fo = \frac{\ln\left(\dfrac{\theta^*}{C_1 J_0(\zeta_1 r^*)}\right)}{-\zeta_1^2}$$

$$\frac{dFo}{d\theta^*} \cdot \Delta\theta^* = \frac{\dfrac{1}{\theta^*}}{-\zeta_1^2} \cdot \Delta\theta^*$$

(A. 60)

$$\frac{dFo}{dC_1} \cdot \Delta C_1 = \frac{-\dfrac{1}{C_1}}{-\zeta_1^2} \cdot \Delta C_1$$

(A. 61)

$$\frac{dFo}{d\zeta_1} \cdot \Delta\zeta_1 = \left[\frac{2\ln\left(\dfrac{\theta^*}{C_1 J_0(\zeta_1 r^*)}\right)}{\zeta_1^3} + \frac{\left(-\dfrac{1}{r^* J_1(\zeta_1)}\right)}{-\zeta_1^2}\right] \cdot \Delta\zeta_1$$

(A. 62)

$$\frac{dFo}{dr^*} \cdot \Delta r^* = \frac{-\dfrac{1}{\zeta_1 J_1(r^*)}}{-\zeta_1^2} \cdot \Delta r^*$$

(A. 63)

$$\omega_{Fo} = \sqrt{\left(\frac{dFo}{d\theta^*} \cdot \Delta\theta^*\right)^2 + \left(\frac{dFo}{dC_1} \cdot \Delta C_1\right)^2 + \left(\frac{dFo}{d\zeta_1} \cdot \Delta\zeta_1\right)^2 + \left(\frac{dFo}{dr^*} \cdot \Delta r^*\right)^2}$$

(A. 64)

Uncertainty in Thermal Diffusivity

$$\alpha = \frac{Fot^2}{t_{ct}}$$

$$\frac{d\alpha}{dFo} \cdot \Delta Fo = \frac{t^2}{t_{ct}} \cdot \Delta Fo$$

(A. 65)

$$\frac{d\alpha}{dt} \cdot \Delta t = \frac{2Fot}{t_{ct}} \cdot \Delta t$$

(A. 66)

$$\frac{d\alpha}{dt_{ct}} \cdot \Delta t_{ct} = -\frac{Fot}{t_{ct}^2} \cdot \Delta t_{tc}$$

(A. 67)

$$\omega_\alpha = \sqrt{\left(\frac{d\alpha}{dFo} \cdot \Delta Fo\right)^2 + \left(\frac{d\alpha}{dt} \cdot \Delta t\right)^2 + \left(\frac{d\alpha}{dt_{ct}} \cdot \Delta t_{ct}\right)^2}$$

(A. 68)

Cooling from $50^{o}C$

Time (Hour)	A.18	A.19	A.20	A.21	A.22	A.23	A.24	A.25
1.67E-02	8.12E-06	1.23E-03	1.23E-03	-1.23E-04	3.76E-02	-1.40E-04	-7.97E-12	3.77E-02
2.78E-01	7.11E-06	1.07E-03	1.23E-03	-1.23E-04	3.30E-02	-1.22E-04	-6.98E-12	3.30E-02
5.56E-01	6.21E-06	9.37E-04	1.23E-03	-1.23E-04	2.88E-02	-1.07E-04	-6.09E-12	2.88E-02
8.33E-01	5.45E-06	8.22E-04	1.23E-03	-1.23E-04	2.52E-02	-9.37E-05	-5.34E-12	2.53E-02
1.11E+00	4.80E-06	7.25E-04	1.23E-03	-1.23E-04	2.23E-02	-8.27E-05	-4.71E-12	2.23E-02
1.39E+00	4.26E-06	6.42E-04	1.23E-03	-1.23E-04	1.97E-02	-7.33E-05	-4.18E-12	1.98E-02
1.94E+00	3.39E-06	5.12E-04	1.23E-03	-1.23E-04	1.57E-02	-5.84E-05	-3.33E-12	1.58E-02
2.78E+00	2.50E-06	3.77E-04	1.23E-03	-1.23E-04	1.16E-02	-4.30E-05	-2.45E-12	1.17E-02
4.17E+00	1.63E-06	2.46E-04	1.23E-03	-1.23E-04	7.54E-03	-2.80E-05	-1.60E-12	7.64E-03
5.56E+00	1.14E-06	1.72E-04	1.23E-03	-1.23E-04	5.29E-03	-1.96E-05	-1.12E-12	5.44E-03
8.33E+00	6.41E-07	9.68E-05	1.23E-03	-1.23E-04	2.97E-03	-1.10E-05	-6.29E-13	3.22E-03
1.11E+01	4.10E-07	6.19E-05	1.23E-03	-1.23E-04	1.90E-03	-7.05E-06	-4.02E-13	2.27E-03
1.39E+01	3.01E-07	4.54E-05	1.23E-03	-1.23E-04	1.39E-03	-5.17E-06	-2.95E-13	1.86E-03
1.67E+01	2.51E-07	3.78E-05	1.23E-03	-1.23E-04	1.16E-03	-4.31E-06	-2.46E-13	1.69E-03
1.94E+01	2.28E-07	3.44E-05	1.23E-03	-1.23E-04	1.06E-03	-3.93E-06	-2.24E-13	1.63E-03
2.22E+01	2.18E-07	3.29E-05	1.23E-03	-1.23E-04	1.01E-03	-3.76E-06	-2.14E-13	1.60E-03

Time (Hour)	A.26	A.27	A.28	A.29	A.30
1.67E-02	6.99E-06	-1.81E-05	1.03E-03	-4.12E-04	1.11E-03
2.78E-01	6.71E-06	-1.73E-05	8.99E-04	-3.96E-04	9.83E-04
5.56E-01	6.42E-06	-1.66E-05	7.85E-04	-3.78E-04	8.72E-04
0.00E+00	6.12E-06	-1.58E-05	6.89E-04	-3.61E-04	7.78E-04
1.11E+00	5.82E-06	-1.50E-05	6.08E-04	-3.43E-04	6.98E-04
1.39E+00	5.52E-06	-1.43E-05	5.39E-04	-3.26E-04	6.30E-04
1.94E+00	4.94E-06	-1.28E-05	4.30E-04	-2.92E-04	5.19E-04
2.78E+00	4.13E-06	-1.07E-05	3.17E-04	-2.44E-04	4.00E-04
4.17E+00	3.01E-06	-7.77E-06	2.08E-04	-1.77E-04	2.74E-04
5.56E+00	2.21E-06	-5.71E-06	1.48E-04	-1.30E-04	1.97E-04
8.33E+00	1.37E-06	-3.55E-06	8.77E-05	-8.10E-05	1.19E-04
1.11E+01	1.08E-06	-2.79E-06	6.17E-05	-6.38E-05	8.88E-05
1.39E+01	9.86E-07	-2.55E-06	5.07E-05	-5.82E-05	7.72E-05
1.67E+01	9.56E-07	-2.47E-06	4.62E-05	-5.64E-05	7.29E-05
1.94E+01	9.47E-07	-2.45E-06	4.43E-05	-5.58E-05	7.13E-05
2.22E+01	9.44E-07	-2.44E-06	4.35E-05	-5.57E-05	7.07E-05

Time (Hour)	A.31	A.32	A.33	A.34
1.67E-02	1.53E-02	2.13E-06	4.17E-01	4.17E-01
2.78E-01	1.51E-02	2.11E-06	3.82E-01	3.82E-01
5.56E-01	1.49E-02	2.09E-06	3.50E-01	3.50E-01
0.00E+00	1.48E-02	2.06E-06	3.24E-01	3.24E-01
1.11E+00	1.46E-02	2.04E-06	3.02E-01	3.02E-01
1.39E+00	1.44E-02	2.01E-06	2.83E-01	2.83E-01
1.94E+00	1.40E-02	1.96E-06	2.54E-01	2.54E-01
2.78E+00	1.34E-02	1.87E-06	2.24E-01	2.24E-01
4.17E+00	1.24E-02	1.73E-06	1.94E-01	1.94E-01
5.56E+00	1.14E-02	1.60E-06	1.76E-01	1.77E-01
8.33E+00	1.02E-02	1.42E-06	1.52E-01	1.53E-01
1.11E+01	9.58E-03	1.34E-06	1.36E-01	1.36E-01
1.39E+01	9.36E-03	1.31E-06	1.26E-01	1.27E-01
1.67E+01	9.29E-03	1.30E-06	1.22E-01	1.22E-01
1.94E+01	9.26E-03	1.30E-06	1.20E-01	1.21E-01
2.22E+01	9.26E-03	1.29E-06	1.20E-01	1.20E-01

Time (Hour)	A.35	A.36	A.37	A.38	A.39	A.40	A.41
1.67E-02	4.41E+02	4.28E+01	6.03E+02	-6.03E+01	-7.40E+01	2.19E+02	7.85E+02
2.78E-01	3.54E+02	3.75E+01	5.97E+02	-5.97E+01	-6.42E+01	1.90E+02	7.26E+02
5.56E-01	2.83E+02	3.27E+01	5.90E+02	-5.90E+01	-5.54E+01	1.64E+02	6.80E+02
0.00E+00	2.30E+02	2.87E+01	5.83E+02	-5.83E+01	-4.80E+01	1.42E+02	6.48E+02
1.11E+00	1.89E+02	2.53E+01	5.76E+02	-5.76E+01	-4.18E+01	1.24E+02	6.23E+02
1.39E+00	1.57E+02	2.24E+01	5.68E+02	-5.68E+01	-3.66E+01	1.08E+02	6.04E+02
1.94E+00	1.12E+02	1.79E+01	5.53E+02	-5.53E+01	-2.84E+01	8.37E+01	5.74E+02
2.78E+00	7.30E+01	1.32E+01	5.29E+02	-5.29E+01	-2.00E+01	5.90E+01	5.40E+02
4.17E+00	4.12E+01	8.57E+00	4.88E+02	-4.88E+01	-1.20E+01	3.55E+01	4.94E+02
5.56E+00	2.63E+01	6.01E+00	4.52E+02	-4.52E+01	-7.80E+00	2.30E+01	4.56E+02
8.33E+00	1.28E+01	3.38E+00	4.01E+02	-4.01E+01	-3.89E+00	1.15E+01	4.04E+02
1.11E+01	7.26E+00	2.16E+00	3.78E+02	-3.78E+01	-2.34E+00	6.92E+00	3.80E+02
1.39E+01	4.96E+00	1.58E+00	3.69E+02	-3.69E+01	-1.68E+00	4.96E+00	3.71E+02
1.67E+01	4.00E+00	1.32E+00	3.67E+02	-3.67E+01	-1.39E+00	4.10E+00	3.69E+02
1.94E+01	3.59E+00	1.20E+00	3.66E+02	-3.66E+01	-1.26E+00	3.72E+00	3.68E+02
2.22E+01	3.41E+00	1.15E+00	3.65E+02	-3.65E+01	-1.21E+00	3.56E+00	3.67E+02

Time (Hour)	A.42	A.43	A.44	A.45	A.46
1.67E-02	8.30E+01	-1.21E+00	-1.11E+01	1.11E+00	8.37E+01
2.78E-01	8.75E+01	-1.32E+00	-1.38E+01	1.38E+00	8.86E+01
5.56E-01	9.40E+01	-1.43E+00	-1.71E+01	1.71E+00	9.56E+01
0.00E+00	1.02E+02	-1.53E+00	-2.09E+01	2.09E+00	1.04E+02
1.11E+00	1.11E+02	-1.63E+00	-2.53E+01	2.53E+00	1.14E+02
1.39E+00	1.22E+02	-1.73E+00	-3.02E+01	3.02E+00	1.25E+02
1.94E+00	1.45E+02	-1.89E+00	-4.13E+01	4.13E+00	1.51E+02
2.78E+00	1.85E+02	-2.05E+00	-6.09E+01	6.09E+00	1.95E+02
4.17E+00	2.60E+02	-2.11E+00	-9.65E+01	9.65E+00	2.78E+02
5.56E+00	3.42E+02	-2.05E+00	-1.33E+02	1.33E+01	3.68E+02
8.33E+00	5.40E+02	-2.02E+00	-2.34E+02	2.34E+01	5.89E+02
1.11E+01	7.96E+02	-2.34E+00	-4.24E+02	4.24E+01	9.02E+02
1.39E+01	1.06E+03	-2.84E+00	-7.02E+02	7.02E+01	1.27E+03
1.67E+01	1.26E+03	-3.28E+00	-9.72E+02	9.72E+01	1.60E+03
1.94E+01	1.38E+03	-3.56E+00	-1.16E+03	1.16E+02	1.81E+03
2.22E+01	1.44E+03	-3.70E+00	-1.26E+03	1.26E+02	1.92E+03
Time (Hour)	A.47	A.48	A.49		A.50
1.67E-02	5.32E+00	1.79E+01	-5.70E-01		1.87E+01
2.78E-01	5.63E+00	1.78E+01	-5.64E-01		1.86E+01
5.56E-01	6.07E+00	1.76E+01	-5.58E-01		1.86E+01
0.00E+00	6.61E+00	1.74E+01	-5.51E-01		1.86E+01
1.11E+00	7.25E+00	1.71E+01	-5.44E-01		1.86E+01
1.39E+00	7.96E+00	1.69E+01	-5.37E-01		1.87E+01
1.94E+00	9.59E+00	1.65E+01	-5.22E-01		1.90E+01
2.78E+00	1.24E+01	1.57E+01	-4.99E-01		2.00E+01
4.17E+00	1.76E+01	1.45E+01	-4.61E-01		2.29E+01
5.56E+00	2.33E+01	1.35E+01	-4.27E-01		2.69E+01
8.33E+00	3.74E+01	1.19E+01	-3.79E-01		3.93E+01
1.11E+01	5.73E+01	1.13E+01	-3.57E-01		5.84E+01
1.39E+01	8.08E+01	1.10E+01	-3.49E-01		8.16E+01
1.67E+01	1.01E+02	1.09E+01	-3.46E-01		1.02E+02
1.94E+01	1.15E+02	1.09E+01	-3.46E-01		1.15E+02
2.22E+01	1.22E+02	1.09E+01	-3.45E-01		1.22E+02
	A.51	A.52			A.53
	1.64E-04	-4.37E-04			4.67E-04

Time (Hour)	A.54			A.55
1.67E-02	-6.92E+01			6.92E+01
2.78E-01	-6.89E+01			6.89E+01
5.56E-01	-6.87E+01			6.87E+01
0.00E+00	-6.87E+01			6.87E+01
1.11E+00	-6.88E+01			6.88E+01
1.39E+00	-6.91E+01			6.91E+01
1.94E+00	-7.04E+01			7.04E+01
2.78E+00	-7.41E+01			7.41E+01
4.17E+00	-8.46E+01			8.46E+01
5.56E+00	-9.98E+01			9.98E+01
8.33E+00	-1.46E+02			1.46E+02
1.11E+01	-2.17E+02			2.17E+02
1.39E+01	-3.03E+02			3.03E+02
1.67E+01	-3.79E+02			3.79E+02
1.94E+01	-4.28E+02			4.28E+02
2.22E+01	-4.55E+02			4.55E+02
Time (Hour)	A.56	A.57	A.58	A.59
1.67E-02	3.83E-02	-9.47E-06	-3.82E-03	3.84E-02
2.78E-01	3.83E-02	-1.59E-04	-3.67E-03	3.84E-02
5.56E-01	3.83E-02	-3.21E-04	-3.50E-03	3.84E-02
0.00E+00	3.83E-02	-4.84E-04	-3.34E-03	3.84E-02
1.11E+00	3.83E-02	-6.47E-04	-3.18E-03	3.84E-02
1.39E+00	3.83E-02	-8.09E-04	-3.02E-03	3.84E-02
1.94E+00	3.83E-02	-1.13E-03	-2.70E-03	3.84E-02
2.78E+00	3.83E-02	-1.57E-03	-2.26E-03	3.84E-02
4.17E+00	3.83E-02	-2.18E-03	-1.64E-03	3.84E-02
5.56E+00	3.83E-02	-2.62E-03	-1.21E-03	3.84E-02
8.33E+00	3.83E-02	-3.08E-03	-7.51E-04	3.84E-02
1.11E+01	3.83E-02	-3.24E-03	-5.91E-04	3.84E-02
1.39E+01	3.83E-02	-3.29E-03	-5.39E-04	3.84E-02
1.67E+01	3.83E-02	-3.30E-03	-5.22E-04	3.84E-02
1.94E+01	3.83E-02	-3.31E-03	-5.17E-04	3.84E-02
2.22E+01	3.83E-02	-3.31E-03	-5.16E-04	3.84E-02

Time (Hour)	A.60	A.61	A.62	A.63	A.64
1.67E-02	-6.78E-03	7.60E+00	3.05E-01	7.84E-05	7.60E+00
2.78E-01	-7.06E-03	7.57E+00	2.67E-01	7.84E-05	7.57E+00
5.56E-01	-7.38E-03	7.55E+00	2.25E-01	7.84E-05	7.55E+00
0.00E+00	-7.74E-03	7.55E+00	1.81E-01	7.84E-05	7.55E+00
1.11E+00	-8.14E-03	7.57E+00	1.35E-01	7.85E-05	7.57E+00
1.39E+00	-8.57E-03	7.60E+00	8.66E-02	7.85E-05	7.61E+00
1.94E+00	-9.58E-03	7.75E+00	-1.72E-02	7.86E-05	7.75E+00
2.78E+00	-1.15E-02	8.16E+00	-1.97E-01	7.87E-05	8.16E+00
4.17E+00	-1.58E-02	9.34E+00	-5.88E-01	7.89E-05	9.36E+00
5.56E+00	-2.15E-02	1.10E+01	-1.11E+00	7.91E-05	1.11E+01
8.33E+00	-3.47E-02	1.62E+01	-2.58E+00	7.94E-05	1.64E+01
1.11E+01	-4.42E-02	2.41E+01	-4.57E+00	7.96E-05	2.45E+01
1.39E+01	-4.85E-02	3.37E+01	-6.79E+00	7.97E-05	3.43E+01
1.67E+01	-5.01E-02	4.21E+01	-8.65E+00	7.97E-05	4.30E+01
1.94E+01	-5.06E-02	4.76E+01	-9.85E+00	7.97E-05	4.86E+01
2.22E+01	-5.07E-02	5.06E+01	-1.04E+01	7.97E-05	5.16E+01

Time (Hour)	A.65	A.66	A.67	A.68(ω_α)	α	% Difference
1.67E-02	2.04E-05	7.43E-07	-1.97E-08	2.05E-05	3.77E-05	5.42E+01
2.78E-01	1.22E-06	4.49E-08	-7.12E-11	1.22E-06	2.28E-06	5.36E+01
5.56E-01	6.09E-07	2.26E-08	-1.79E-11	6.10E-07	1.15E-06	5.31E+01
0.00E+00	4.06E-07	1.52E-08	-8.03E-12	4.06E-07	7.70E-07	5.27E+01
1.11E+00	3.05E-07	1.15E-08	-4.55E-12	3.05E-07	5.82E-07	5.24E+01
1.39E+00	2.45E-07	9.24E-09	-2.93E-12	2.45E-07	4.70E-07	5.23E+01
1.94E+00	1.79E-07	6.71E-09	-1.52E-12	1.79E-07	3.41E-07	5.24E+01
2.78E+00	1.32E-07	4.82E-09	-7.66E-13	1.32E-07	2.45E-07	5.38E+01
4.17E+00	1.01E-07	3.36E-09	-3.56E-13	1.01E-07	1.71E-07	5.89E+01
5.56E+00	8.95E-08	2.63E-09	-2.09E-13	8.95E-08	1.34E-07	6.70E+01
8.33E+00	8.80E-08	1.87E-09	-9.87E-14	8.80E-08	9.48E-08	9.28E+01
1.11E+01	9.88E-08	1.44E-09	-5.73E-14	9.88E-08	7.33E-08	1.35E+02
1.39E+01	1.11E-07	1.17E-09	-3.71E-14	1.11E-07	5.93E-08	1.87E+02
1.67E+01	1.15E-07	9.77E-10	-2.59E-14	1.15E-07	4.97E-08	2.33E+02
1.94E+01	1.12E-07	8.39E-10	-1.90E-14	1.12E-07	4.26E-08	2.63E+02
2.22E+01	1.04E-07	7.33E-10	-1.46E-14	1.04E-07	3.73E-08	2.79E+02

Cooling from 80$^o C$

Time (Hour)	A.18	A.19	A.20	A.21	A.22	A.23	A.24	A.25
1.67E-02	1.37E-05	2.06E-03	1.23E-03	-1.23E-04	6.33E-02	-2.35E-04	-1.34E-11	6.34E-02
2.78E-01	1.22E-05	1.84E-03	1.23E-03	-1.23E-04	5.64E-02	-2.09E-04	-1.19E-11	5.64E-02
5.56E-01	1.08E-05	1.62E-03	1.23E-03	-1.23E-04	4.99E-02	-1.85E-04	-1.06E-11	4.99E-02
8.33E-01	9.54E-06	1.44E-03	1.23E-03	-1.23E-04	4.42E-02	-1.64E-04	-9.36E-12	4.42E-02
1.11E+00	8.47E-06	1.28E-03	1.23E-03	-1.23E-04	3.93E-02	-1.46E-04	-8.31E-12	3.93E-02
1.39E+00	7.54E-06	1.14E-03	1.23E-03	-1.23E-04	3.49E-02	-1.30E-04	-7.39E-12	3.50E-02
1.94E+00	6.02E-06	9.08E-04	1.23E-03	-1.23E-04	2.79E-02	-1.04E-04	-5.90E-12	2.79E-02
2.78E+00	4.38E-06	6.62E-04	1.23E-03	-1.23E-04	2.03E-02	-7.54E-05	-4.30E-12	2.04E-02
4.17E+00	2.76E-06	4.16E-04	1.23E-03	-1.23E-04	1.28E-02	-4.75E-05	-2.71E-12	1.29E-02
5.56E+00	1.87E-06	2.82E-04	1.23E-03	-1.23E-04	8.65E-03	-3.21E-05	-1.83E-12	8.74E-03
8.33E+00	9.74E-07	1.47E-04	1.23E-03	-1.23E-04	4.51E-03	-1.68E-05	-9.55E-13	4.68E-03
1.11E+01	5.69E-07	8.58E-05	1.23E-03	-1.23E-04	2.64E-03	-9.79E-06	-5.58E-13	2.91E-03
1.39E+01	3.77E-07	5.69E-05	1.23E-03	-1.23E-04	1.75E-03	-6.49E-06	-3.70E-13	2.14E-03
1.67E+01	2.88E-07	4.34E-05	1.23E-03	-1.23E-04	1.33E-03	-4.95E-06	-2.82E-13	1.82E-03
1.94E+01	2.47E-07	3.73E-05	1.23E-03	-1.23E-04	1.14E-03	-4.25E-06	-2.42E-13	1.68E-03
2.22E+01	2.29E-07	3.45E-05	1.23E-03	-1.23E-04	1.06E-03	-3.94E-06	-2.24E-13	1.63E-03

Time (Hour)	A.26	A.27	A.28	A.29	A.30
1.67E-02	8.13E-06	-2.10E-05	1.73E-03	-4.80E-04	1.79E-03
2.78E-01	7.84E-06	-2.02E-05	1.54E-03	-4.62E-04	1.60E-03
5.56E-01	7.51E-06	-1.94E-05	1.36E-03	-4.43E-04	1.43E-03
0.00E+00	7.17E-06	-1.85E-05	1.21E-03	-4.23E-04	1.28E-03
1.11E+00	6.82E-06	-1.76E-05	1.07E-03	-4.02E-04	1.14E-03
1.39E+00	6.47E-06	-1.67E-05	9.53E-04	-3.82E-04	1.03E-03
1.94E+00	5.76E-06	-1.49E-05	7.61E-04	-3.40E-04	8.33E-04
2.78E+00	4.72E-06	-1.22E-05	5.55E-04	-2.78E-04	6.21E-04
4.17E+00	3.21E-06	-8.30E-06	3.50E-04	-1.89E-04	3.98E-04
5.56E+00	2.12E-06	-5.47E-06	2.38E-04	-1.25E-04	2.69E-04
8.33E+00	1.00E-06	-2.59E-06	1.27E-04	-5.92E-05	1.41E-04
1.11E+01	6.46E-07	-1.67E-06	7.93E-05	-3.81E-05	8.80E-05
1.39E+01	5.42E-07	-1.40E-06	5.83E-05	-3.20E-05	6.65E-05
1.67E+01	5.13E-07	-1.33E-06	4.95E-05	-3.03E-05	5.80E-05
1.94E+01	5.05E-07	-1.30E-06	4.59E-05	-2.98E-05	5.47E-05
2.22E+01	5.03E-07	-1.30E-06	4.43E-05	-2.96E-05	5.33E-05

Time (Hour)	A.31	A.32	A.33				A.34
1.67E-02	1.59E-02	2.22E-06	6.02E-01				6.03E-01
2.78E-01	1.57E-02	2.20E-06	5.55E-01				5.55E-01
5.56E-01	1.55E-02	2.17E-06	5.11E-01				5.11E-01
0.00E+00	1.54E-02	2.15E-06	4.72E-01				4.72E-01
1.11E+00	1.52E-02	2.12E-06	4.39E-01				4.39E-01
1.39E+00	1.50E-02	2.09E-06	4.10E-01				4.10E-01
1.94E+00	1.45E-02	2.03E-06	3.63E-01				3.63E-01
2.78E+00	1.38E-02	1.93E-06	3.14E-01				3.14E-01
4.17E+00	1.26E-02	1.76E-06	2.69E-01				2.69E-01
5.56E+00	1.13E-02	1.58E-06	2.48E-01				2.48E-01
8.33E+00	9.40E-03	1.31E-06	2.27E-01				2.27E-01
1.11E+01	8.42E-03	1.18E-06	1.98E-01				1.98E-01
1.39E+01	8.06E-03	1.13E-06	1.70E-01				1.71E-01
1.67E+01	7.95E-03	1.11E-06	1.55E-01				1.55E-01
1.94E+01	7.92E-03	1.11E-06	1.48E-01				1.48E-01
2.22E+01	7.91E-03	1.11E-06	1.45E-01				1.45E-01

Time (Hour)	A.35	A.36	A.37	A.38	A.39	A.40	A.41
1.67E-02	1.07E+03	7.47E+01	6.26E+02	-6.26E+01	-1.29E+02	3.82E+02	1.31E+03
2.78E-01	8.80E+02	6.65E+01	6.20E+02	-6.20E+01	-1.14E+02	3.37E+02	1.14E+03
5.56E-01	7.16E+02	5.89E+01	6.14E+02	-6.14E+01	-9.99E+01	2.95E+02	9.97E+02
0.00E+00	5.87E+02	5.22E+01	6.07E+02	-6.07E+01	-8.75E+01	2.58E+02	8.91E+02
1.11E+00	4.85E+02	4.63E+01	5.99E+02	-5.99E+01	-7.68E+01	2.27E+02	8.10E+02
1.39E+00	4.03E+02	4.12E+01	5.91E+02	-5.91E+01	-6.74E+01	1.99E+02	7.49E+02
1.94E+00	2.85E+02	3.29E+01	5.74E+02	-5.74E+01	-5.22E+01	1.54E+02	6.65E+02
2.78E+00	1.80E+02	2.40E+01	5.46E+02	-5.46E+01	-3.62E+01	1.07E+02	5.89E+02
4.17E+00	9.68E+01	1.51E+01	4.96E+02	-4.96E+01	-2.07E+01	6.11E+01	5.12E+02
5.56E+00	6.04E+01	1.02E+01	4.47E+02	-4.47E+01	-1.26E+01	3.73E+01	4.55E+02
8.33E+00	2.88E+01	5.33E+00	3.71E+02	-3.71E+01	-5.46E+00	1.61E+01	3.75E+02
1.11E+01	1.47E+01	3.11E+00	3.32E+02	-3.32E+01	-2.86E+00	8.44E+00	3.35E+02
1.39E+01	8.38E+00	2.06E+00	3.18E+02	-3.18E+01	-1.81E+00	5.35E+00	3.20E+02
1.67E+01	5.82E+00	1.57E+00	3.14E+02	-3.14E+01	-1.36E+00	4.03E+00	3.15E+02
1.94E+01	4.77E+00	1.35E+00	3.13E+02	-3.13E+01	-1.17E+00	3.45E+00	3.14E+02
2.22E+01	4.32E+00	1.25E+00	3.12E+02	-3.12E+01	-1.08E+00	3.19E+00	3.14E+02

Time (Hour)	A.42	A.43	A.44	A.45	A.46
1.67E-02	8.22E+01	-8.73E-01	-4.75E+00	4.75E-01	8.24E+01
2.78E-01	8.02E+01	-9.36E-01	-5.72E+00	5.72E-01	8.04E+01
5.56E-01	7.95E+01	-1.00E+00	-6.92E+00	6.92E-01	7.98E+01
0.00E+00	8.01E+01	-1.07E+00	-8.32E+00	8.32E-01	8.06E+01
1.11E+00	8.21E+01	-1.13E+00	-9.92E+00	9.92E-01	8.27E+01
1.39E+00	8.52E+01	-1.19E+00	-1.17E+01	1.17E+00	8.61E+01
1.94E+00	9.48E+01	-1.29E+00	-1.59E+01	1.59E+00	9.61E+01
2.78E+00	1.15E+02	-1.38E+00	-2.33E+01	2.33E+00	1.18E+02
4.17E+00	1.59E+02	-1.35E+00	-3.64E+01	3.64E+00	1.63E+02
5.56E+00	2.09E+02	-1.19E+00	-4.73E+01	4.73E+00	2.15E+02
8.33E+00	3.30E+02	-8.96E-01	-6.84E+01	6.84E+00	3.37E+02
1.11E+01	5.05E+02	-8.85E-01	-1.16E+02	1.16E+01	5.18E+02
1.39E+01	7.28E+02	-1.07E+00	-2.11E+02	2.11E+01	7.59E+02
1.67E+01	9.41E+02	-1.31E+00	-3.39E+02	3.39E+01	1.00E+03
1.94E+01	1.09E+03	-1.50E+00	-4.50E+02	4.50E+01	1.18E+03
2.22E+01	1.18E+03	-1.61E+00	-5.22E+02	5.22E+01	1.29E+03

Time (Hour)	A.47	A.48	A.49	A.50
1.67E-02	5.23E+00	1.86E+01	-5.92E-01	1.94E+01
2.78E-01	5.11E+00	1.85E+01	-5.86E-01	1.92E+01
5.56E-01	5.07E+00	1.83E+01	-5.80E-01	1.90E+01
0.00E+00	5.12E+00	1.81E+01	-5.73E-01	1.88E+01
1.11E+00	5.25E+00	1.78E+01	-5.66E-01	1.86E+01
1.39E+00	5.47E+00	1.76E+01	-5.59E-01	1.84E+01
1.94E+00	6.10E+00	1.71E+01	-5.43E-01	1.82E+01
2.78E+00	7.47E+00	1.63E+01	-5.16E-01	1.79E+01
4.17E+00	1.04E+01	1.48E+01	-4.69E-01	1.81E+01
5.56E+00	1.36E+01	1.33E+01	-4.23E-01	1.91E+01
8.33E+00	2.14E+01	1.10E+01	-3.51E-01	2.41E+01
1.11E+01	3.29E+01	9.89E+00	-3.14E-01	3.43E+01
1.39E+01	4.82E+01	9.47E+00	-3.01E-01	4.91E+01
1.67E+01	6.35E+01	9.34E+00	-2.96E-01	6.42E+01
1.94E+01	7.50E+01	9.30E+00	-2.95E-01	7.56E+01
2.22E+01	8.18E+01	9.29E+00	-2.95E-01	8.23E+01

A.51	A.52	A.53
1.64E-04	-4.37E-04	4.67E-04

Time (Hour)	A.54			A.55
1.67E-02	-7.15E+01			7.15E+01
2.78E-01	-7.08E+01			7.08E+01
5.56E-01	-7.00E+01			7.00E+01
0.00E+00	-6.94E+01			6.94E+01
1.11E+00	-6.87E+01			6.87E+01
1.39E+00	-6.81E+01			6.81E+01
1.94E+00	-6.71E+01			6.71E+01
2.78E+00	-6.62E+01			6.62E+01
4.17E+00	-6.68E+01			6.68E+01
5.56E+00	-7.06E+01			7.06E+01
8.33E+00	-8.95E+01			8.95E+01
1.11E+01	-1.28E+02			1.28E+02
1.39E+01	-1.83E+02			1.83E+02
1.67E+01	-2.39E+02			2.39E+02
1.94E+01	-2.81E+02			2.81E+02
2.22E+01	-3.07E+02			3.07E+02
Time (Hour)	A.56	A.57	A.58	A.59
1.67E-02	3.29E-02	-7.45E-06	-3.28E-03	3.30E-02
2.78E-01	3.29E-02	-1.27E-04	-3.16E-03	3.30E-02
5.56E-01	3.29E-02	-2.59E-04	-3.03E-03	3.30E-02
0.00E+00	3.29E-02	-3.95E-04	-2.89E-03	3.30E-02
1.11E+00	3.29E-02	-5.35E-04	-2.75E-03	3.30E-02
1.39E+00	3.29E-02	-6.77E-04	-2.61E-03	3.30E-02
1.94E+00	3.29E-02	-9.65E-04	-2.32E-03	3.30E-02
2.78E+00	3.29E-02	-1.38E-03	-1.90E-03	3.30E-02
4.17E+00	3.29E-02	-1.99E-03	-1.30E-03	3.30E-02
5.56E+00	3.29E-02	-2.43E-03	-8.54E-04	3.30E-02
8.33E+00	3.29E-02	-2.88E-03	-4.05E-04	3.30E-02
1.11E+01	3.29E-02	-3.03E-03	-2.61E-04	3.30E-02
1.39E+01	3.29E-02	-3.07E-03	-2.19E-04	3.30E-02
1.67E+01	3.29E-02	-3.08E-03	-2.07E-04	3.30E-02
1.94E+01	3.29E-02	-3.08E-03	-2.04E-04	3.30E-02
2.22E+01	3.29E-02	-3.09E-03	-2.03E-04	3.30E-02

Time (Hour)	A.60	A.61	A.62	A.63	A.64
1.67E-02	-5.82E-03	7.85E+00	2.73E-01	7.83E-05	7.86E+00
2.78E-01	-6.04E-03	7.77E+00	2.35E-01	7.83E-05	7.78E+00
5.56E-01	-6.31E-03	7.69E+00	1.92E-01	7.83E-05	7.70E+00
0.00E+00	-6.60E-03	7.62E+00	1.48E-01	7.84E-05	7.62E+00
1.11E+00	-6.94E-03	7.55E+00	1.01E-01	7.84E-05	7.55E+00
1.39E+00	-7.31E-03	7.49E+00	5.14E-02	7.84E-05	7.49E+00
1.94E+00	-8.22E-03	7.38E+00	-5.44E-02	7.85E-05	7.38E+00
2.78E+00	-1.00E-02	7.29E+00	-2.32E-01	7.86E-05	7.29E+00
4.17E+00	-1.48E-02	7.37E+00	-5.82E-01	7.88E-05	7.39E+00
5.56E+00	-2.25E-02	7.81E+00	-1.02E+00	7.91E-05	7.87E+00
8.33E+00	-4.77E-02	9.94E+00	-2.21E+00	7.97E-05	1.02E+01
1.11E+01	-7.43E-02	1.42E+01	-3.95E+00	8.01E-05	1.48E+01
1.39E+01	-8.87E-02	2.04E+01	-6.10E+00	8.02E-05	2.13E+01
1.67E+01	-9.38E-02	2.67E+01	-8.17E+00	8.03E-05	2.79E+01
1.94E+01	-9.54E-02	3.14E+01	-9.68E+00	8.03E-05	3.29E+01
2.22E+01	-9.58E-02	3.43E+01	-1.06E+01	8.03E-05	3.59E+01

Time (Hour)	A.65	A.66	A.67	A.68(ω_α)	α	% Difference
1.67E-02	2.11E-05	7.48E-07	-1.98E-08	2.11E-05	3.80E-05	5.56E+01
2.78E-01	1.25E-06	4.51E-08	-7.17E-11	1.26E-06	2.29E-06	5.47E+01
5.56E-01	6.21E-07	2.27E-08	-1.80E-11	6.21E-07	1.15E-06	5.38E+01
0.00E+00	4.10E-07	1.53E-08	-8.07E-12	4.10E-07	7.75E-07	5.29E+01
1.11E+00	3.04E-07	1.15E-08	-4.57E-12	3.05E-07	5.85E-07	5.20E+01
1.39E+00	2.42E-07	9.29E-09	-2.95E-12	2.42E-07	4.72E-07	5.12E+01
1.94E+00	1.70E-07	6.75E-09	-1.53E-12	1.70E-07	3.43E-07	4.96E+01
2.78E+00	1.18E-07	4.87E-09	-7.72E-13	1.18E-07	2.47E-07	4.76E+01
4.17E+00	7.95E-08	3.42E-09	-3.62E-13	7.96E-08	1.74E-07	4.58E+01
5.56E+00	6.35E-08	2.71E-09	-2.15E-13	6.35E-08	1.38E-07	4.61E+01
8.33E+00	5.48E-08	1.99E-09	-1.05E-13	5.48E-08	1.01E-07	5.43E+01
1.11E+01	5.96E-08	1.57E-09	-6.23E-14	5.96E-08	7.97E-08	7.48E+01
1.39E+01	6.87E-08	1.28E-09	-4.07E-14	6.87E-08	6.51E-08	1.06E+02
1.67E+01	7.51E-08	1.07E-09	-2.84E-14	7.51E-08	5.46E-08	1.38E+02
1.94E+01	7.58E-08	9.23E-10	-2.09E-14	7.58E-08	4.69E-08	1.62E+02
2.22E+01	7.23E-08	8.08E-10	-1.60E-14	7.23E-08	4.10E-08	1.76E+02

VITA

Dong Keun Kim was born in Seoul city (Republic of Korea) in 1975. He graduated with his Bachelor of Science degree in aeronautical and mechanical engineering from Hankuk Aviation University in 1998, and was subsequently awarded his Master of Science degree by the same university in 2003 for his study of the Miniature Heat Pipes for Electronics cooling. In 2003, he moved to the United States to pursue his doctorate at Texas A&M University in College Station, Texas. Dong Keun's research has focused on the developing analytical model for conduction heat transfer and interstitial insulation technology. He received his Doctor of Philosophy in 2008 in mechanical engineering from Texas A&M University

Dong Keun Kim can be contacted through Texas A&M University's Department of Mechanical Engineering at the following address:

dkkim@tamu.edu

Thermal Conduction Laboratory

Department of Mechanical Engineering

Texas A&M University

3123 TAMU

College Station, TX 77843-3123